Journal of Molecular Catalysis A: Chemical 355 (2012) 1–38

Contents lists available at SciVerse ScienceDirect

Journal of Molecular Catalysis A: Chemical

journal homepage: www.elsevier.com/locate/molcata

Review

A review of the kinetics and mechanisms of formation of supported-nanoparticle heterogeneous catalysts

Joseph E. Mondloch, Ercan Bayram, Richard G. Finke*

Department of Chemistry, Colorado State University, Fort Collins, CO 80523, United States

ARTICLE INFO

Article history:
Received 4 July 2011
Received in revised form 6 November 2011
Accepted 7 November 2011
Available online 17 November 2011

Keywords:
Heterogeneous catalysis
Nanoparticle
Kinetics
Mechanism
Review

ABSTRACT

Nanoparticles supported on high surface area materials are commonly used in many industrially relevant catalytic reactions. This review examines the existing literature of the mechanisms of formation of practical, non-ultra high vacuum, supported-nanoparticle heterogeneous catalysts. Specifically, this review includes: (i) a brief overview of the synthesis of supported-nanoparticles, (ii) an overview of the physical methods for following the kinetics of formation of supported-nanoparticles, and then (iii) a summary of the kinetic and mechanistic studies of the formation of supported nanoparticle catalysts, performed under the traditional synthetic conditions of the gas–solid interface. This review then also discusses (iv) the synthesis, (v) physical methods, and (vi) the extant kinetic and mechanistic studies under the less traditional, less examined conditions of a liquid–solid system. A summary of the main insights from each section of the review is also given. Overall, surprisingly little is known about the mechanism(s) of formation of the desired size, shape and compositionally controlled supported-nanoparticle catalysts.

Contents

* Corresponding author. Tel.: +1 970 491 2541; fax: +1 970 491 1801.
E-mail address: rfinke@lamar.colostate.edu (R.G. Finke).

1381-1169/$ – see front matter © 2011 Elsevier B.V. All rights reserved.
doi:10.1016/j.molcata.2011.11.011

1. Introduction

1.1. The importance of mechanistic studies of heterogeneous catalyst formation

Heterogeneous catalysts are used in many important and industrially relevant catalytic reactions such as hydrogenations, catalytic cracking, or naptha reforming; heterogeneous catalysts are also employed in the water–gas shift reaction, the synthesis of ammonia and for ethylene oxidation, to name a few additional reactions [1–4]. Often these heterogeneous catalysts take the form of nanoparticles supported on high-surface-area materials [3,5]. Key properties inherent to these supported-nanoparticle catalysts are known to affect greatly the resultant catalytic performance [6,7]. For example, the size [8–10], structure [11–13] and the lesser investigated, but crucial, surface composition [14–17] of the supported-nanoparticles can influence the catalytic selectivity [6,13,18,19], activity [8,20] and lifetime [21]. Hence, in order to exploit these key catalytic properties for catalysis, uniform catalysts of the appropriate size, structure and composition are needed [22,23].

Unfortunately, as Schlögl has recently noted [7], "catalysts are currently prepared rather than synthesized" so that rationally guided syntheses of the desired size, structure and compositionally controlled supported-nanoparticle catalysts are generally lacking. One main reason for this gap is the relatively poor understanding of the mechanism(s) that govern the formation of these supported-nanoparticle heterogeneous catalysts. In particular, kinetic studies are often lacking, kinetics being one of the general tools crucial in elucidating reliable reaction mechanisms [24–28].[1]

1.2. Organization and scope of this review

Herein we focus on reactions that assemble supported-nanoparticles starting from molecular precursors. What follows is organized into two main sections: studies of supported-nanoparticle formation at the gas–solid interface (Section 2), and then studies of supported-nanoparticle formation in liquid–solid systems (Section 3). Sections 2 and 3 each contain: (i) a fundamental background information section which details the synthesis of supported-nanoparticles as well as the physical methods that have been utilized to measure their kinetics of formation; (ii) case studies regarding the kinetics and mechanisms of supported-nanoparticle formation; and (iii) a conclusions section that summarizes the key results in each section. A summary section (Section 4) is also provided listing the broader, key insights obtained from this first-of-its kind review.

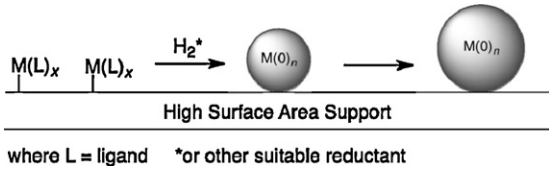

Scheme 1. A pictorial representation of supported-nanoparticle heterogeneous catalyst formation at the gas–solid interface.

To start, in Section 2 we focus on systems involving the gas–solid interface as depicted in Scheme 1. We were able to find only 39 papers [29–67] (which are given in Table S1, a condensed version of which is shown in Table 2) that address the kinetics and mechanism(s) of practical, non-ultra-high vacuum, supported-nanoparticle heterogeneous catalyst formation under traditional preparation conditions [22] at the gas–solid interface. Then, in Section 3 we review the less-commonly studied, but potentially quite valuable, liquid–solid systems. We found an additional eight kinetic and mechanistic studies [68–75], listed in Table 3, performed in contact with solution. The presence of a solvent means that the supported-nanoparticle formation steps can occur in solution, on the support, or possibly in both phases as depicted in Scheme 2.

Note that the gas–solid and liquid–solid synthetic conditions stand in stark contrast to the cleaner, better studied (and thoroughly reviewed [76–79]), but model catalysts made under ultra high vacuum (UHV) conditions. The difference between those high-vacuum, ultra-clean, often single-crystal/single facet vapor-deposited metal(0) atom model studies vs. the studies emphasized herein (on "practical, dirty" catalysts) are the so-called "pressure", "temperature" and "materials" gaps [80–84]. The uncertainty at

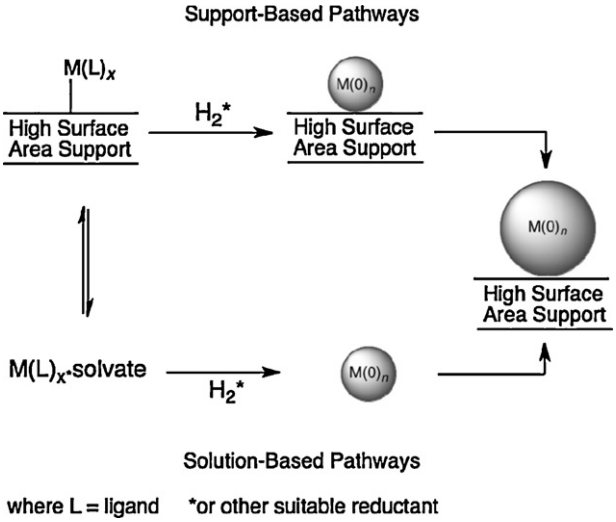

Scheme 2. A pictorial representation of the a priori plausible pathways for supported-nanoparticle formation in liquid–solid systems. The supported-nanoparticle formation can in principle occur on the support (top), in solution (bottom) or via some combination of these pathways. Section 3.2.2.4, vide infra, will examine the possible pathways in more detail.

[1] Complete mechanistic studies require more than just kinetic studies; for example, mechanistic studies of homogeneous organic [24], organometallic [25,26], or inorganic [27,28] reactions typically employ the following types of measurements: (i) first and foremost, determination of the balanced, complete reaction stoichiometry including identification of all trace products; (ii) thermochemical data; (iii) early and direct detection of intermediates—so that multistep reactions can be broken into elementary steps; (iv) kinetic studies, which typically elucidate the composition of the transition-state of the rate-determining step; (v) stereochemistry; (vi) indirect detection or other evidence for (e.g., trapping of) intermediates; (vii) independent syntheses and study of those key intermediates; and (viii) other specialized measurements such as crossover experiments, isotopic labeling or isotope effect studies, to name a few.

present of how to bridge these gaps means that we will not cover, but will supply lead references when necessary to, the: (i) kinetics and mechanisms of model UHV studies [79,80]; (ii) reactions that are occurring non-deliberately during catalyst preparation such as "autoreduction"[2]; and also references to (iii) so-called "dynamic adsorbate induced phase changes" [85] of supported metal nanoparticles (such as are present in the reduction of CuO/ZnO to Cu(0)/ZnO [86,113] or the reduction of Rh_2O_3/Al_2O_3 to $Rh(0)/Al_2O_3$ [87], or their single crystalline counterparts [11,88]). In addition, due to space limitations and the desire to focus this review as much as possible we will not cover (iv) the reduction of bulk metal oxides to their metallic counterparts, for example the reduction of $(CuO)_n$ to $Cu(0)_n$ [89]. There are some reports of supported-nanoparticle formation in liquid–solid systems that occur under photo-deposition [90] or γ-irradiation [91] conditions, but those, too, have been deemed beyond the scope of this review.

2. Studies of supported-nanoparticles at the gas–solid interface

To begin, it is important to describe the synthetic methods available at present for preparing supported-nanoparticles at the gas–solid interface. After that, a summary of the physical methods capable of following the kinetics of supported-nanoparticle formation at the gas–solid interface will be given.

2.1. Fundamental background information regarding supported-nanoparticle heterogeneous catalyst formation at the gas–solid interface

2.1.1. Synthesis methods for supported-nanoparticle heterogeneous catalysts at the gas–solid interface

Many synthetic methods exist for preparing supported-nanoparticle heterogeneous catalysts; hence, several books [3,92–94] and reviews [8,95] thoroughly describe such preparations. Therefore, for the purpose of this review it will suffice to briefly outline the most common heterogeneous catalyst preparation techniques. The interested reader is referred to that literature [3,8,92–95] for more detailed discussions of these well-established heterogeneous catalyst preparation methods.

In a simplified view, supported-nanoparticle heterogeneous catalyst preparation consists of three steps: (i) contact of a metal precursor with the support material; (ii) oxidation/calcination of the resultant precatalyst precursor/support material, and then (iii) formation of the active catalyst species via reduction (e.g., often under H_2)—it is this reduction step during which the supported-nanoparticles are typically formed [8].

Introduction of metal precursors onto a suitable support can be accomplished by several, established methods. Common methods include: (i) impregnation [96], which involves deposition of a metal precursor onto a support, typically from an aqueous solution (e.g. the well-studied system of H_2PtCl_6 impregnation onto γ-Al_2O_3, vide infra); (ii) coprecipitation [97], in which the support and metal precursor are simultaneously precipitated from solution, (iii) deposition–precipitation [8], where the support is already present in solution and a metal precursor is precipitated onto that support (often in the form of a metal oxide) from solution, and (iv) ion-exchange, as commonly used for the preparation of zeolite supported catalysts, for example, where metal salts such as $Pt(NH_3)_4^{2+}$ in aqueous solution are exchanged with $2K^+$ cations from a zeolite support [98]. One can also (v) employ preformed metal clusters, such as metal carbonyls, $M(CO)_x$ or $M_y(CO)_z$ [99–101], or (vi) deposit preformed colloids [8] (and, more recently, preformed/ligated nanoparticles [102–105],[3] vide infra). Each method has advantages and disadvantages as discussed in detail elsewhere [8,106], some of which will be brought out in what follows.

An important point that is often ignored (vide infra) is the speciation of the metal precatalyst [72,74]—that is, the specific composition and number of chemical species present post the precatalyst/support contact step. Often multiple species are present, in turn leading to complex formation reactions and kinetics for the resultant supported-nanoparticles. Hence, it is of the utmost importance to synthesize speciation-controlled supported-metal precatalysts in order to achieve the best supported-nanoparticle formation reactions as well to simplify the kinetic and mechanistic studies of those (improved) synthetic reactions.

The next step in catalyst preparation is often calcination. Che and co-workers have correctly noted that "calcination may have a pronounced effect on the reducibility, dispersion, and distribution of the metal in the final catalyst" [8]. Calcination is typically carried out in air in order to oxidatively remove unwanted ligands that came with the metal precursor complex and to attempt to remove, completely, any carbonaceous overlayers that may be present. As Schwarz et al. [106] have noted, "*calcination can change the metal precatalyst complex, typically forming metal-oxide species that are often ill-defined*"—and, we would add, that are, therefore, typically not speciation controlled. Clearly, strongly ligated precatalysts that yield poorly defined, speciation uncontrolled, secondary precatalysts are non-ideal both synthetically and from a kinetic and mechanistic standpoint. The need to begin with a single molecular

[2] The phenomenon of "autoreduction" can be described as the formation of supported $M(0)_n$ clusters or nanoparticles under conditions where a typical reductant, such as H_2, is not deliberately introduced into the system. Hence, a reduction reaction can occur under what would otherwise be oxidative (e.g., under O_2 calcination conditions) or inert (e.g., He) conditions. Generally speaking, the primary possible sources of the required reducing equivalents appear at present to be either a ligand or the support [98,151,175]. For example, when starting with $M(NH_3)_4^{2+}$/zeolite (M = Pt, Pd) supported precatalysts, Sachtler has noted that "the formation of metal clusters and zeolite protons in the reducing atmosphere of (decomposing) amine ligands" occurs [98]. An excellent account of "autoreduction" due to ligand-induced metal reduction, when starting with those $M(NH_3)_4^{2+}$ complexes, is given in the introduction of a paper by van Santen and co-workers [151]. Alternatively, an example where the support appears to supply the reducing equivalent is given by Jacobs et al. [175]; they propose that a zeolite support can generate reducing equivalents during thermal dehydration via the following reaction: $2(Ag^+ZO^-) \rightarrow \frac{1}{2}O_2 + Ag_2{}^0 + ZO^- + Z^+$ (where Z indicates the zeolite lattice). Note that high temperature, a relatively weak $Ag^+-{}^-OZ$ bond energy, and a basic/somewhat reducing, anionic site appear to be factors in the driving force of this particular "autoreduction" reaction.

[3] Modern transition-metal nanoparticles can be distinguished from classical colloids via [102]: (i) their typically smaller size and narrower size distributions; (ii) their isolability; (iii) their better compositional definition, and (iv) their reproducible preparation and subsequent reproducible catalysis [102]. Another relevant distinction here, as discussed previously [104], is that between nanoparticles, nanoclusters and clusters. Schmid et al. noted in 2010 [105] that there "is still no clear discrimination between the terms "cluster" and "nanoparticle". Historically, clusters have not been specified in size, but have been considered to be discrete, atomically precise species containing metal–metal bonds "exactly defined in (their) chemical composition and structure" [105]. Many types of "clusters" are known in the literature, metal carbonyl clusters, $M_y(CO)_z$, being among the best studied [102,105]. In contrast, the terms nanoparticles and nanoclusters imply a size between 1 and 100 nm, terms which are used interchangeably within the extant literature. Nanoparticles "usually means particles of less precise characterization" [105], often particles with a range of sizes and chemical compositions. Unfortunately, the terms nanoparticles, nanoclusters or clusters are used almost interchangeably in the current literature. A more precise vocabulary would, we suggest, use the following terms: (i) *nanoparticle*, when the precise structure of the particle is not known and a range of particle sizes between 1 and 100 nm are present; (ii) *nanocluster*, when the precise structure of the particle is known and is ≥1 nm in size, and (iii) *cluster*, when the precise composition and structure of the compound are known and the cluster is <1 nm in size.

Table 1
Physical methods used in the literature for measuring the kinetics of supported-nanoparticle heterogeneous catalyst formation at the gas–solid interface.

Method	Times utilized in Table 2	Direct/indirect[a]	In situ or ex situ (as used to date)
Extended X-ray absorbance fine structure spectroscopy	18	Direct	In situ
X-ray absorbance near edge structure spectroscopy	15	Indirect to direct [b]	In situ
H_2 uptake kinetics	8	Indirect	In situ
Infrared spectroscopy	5	Indirect	In situ
Electron spin resonance	2	Direct	Ex situ
H_2 chemisorption	1	Indirect	Ex situ
Total high energy X-ray scattering plus pair-distribution-function analysis	2	Direct	In situ
UV–vis spectroscopy	1	Indirect to direct [c]	In situ
X-ray diffraction	1	Direct	In situ

[a] Direct (vs. indirect) is defined as the ability (or not) of the cited physical method to directly monitor M–M or net $M(0)_n$ nanoparticle formation. In addition, a direct physical method as defined herein should be able to measure those M–M bonds or $M(0)_n$ over the concentration range of interest.
[b] XANES could in principle be used to follow $M(0)_n$ formation if one has the independent XANES spectrum for both the reactants and products. For the studies identified within this review, the XANES edge has typically been used to follow the loss of the starting material qualitatively.
[c] UV–vis spectroscopy can be direct if the metal of interest contains a plasmon resonance band in the visible region (e.g., Au, Ag and Cu).

precursor, of precisely defined composition and structure, en route to superior supported nanoparticle catalysts will be an important, fundamental and recurring point throughout this review, vide infra.

The final step in supported-nanoparticle heterogeneous catalyst preparation is the transformation of the precatalyst—or, really and typically, the range of precatalyst species present post the contact and calcination steps, vide infra—to the $M(0)_n$ supported-nanoparticle catalyst(s), typically by reduction under H_2. Again the experimental conditions, such as the temperature or H_2 pressure, can change the observed catalyst product so that the reduction step needs to be optimized for each individual supported-metal precatalyst [3]. Importantly, the reduction of non-speciation controlled supported-metal precatalysts often leads to a wide distribution of supported-nanoparticle products (vide supra and vide infra), so that precise, careful control of the precatalyst speciation is essential for preparing the next generation of size-, shape- and composition-controlled supported-nanoparticle catalysts. Overall and ultimately, it will become apparent throughout this review that each of the catalyst preparation steps (i.e., precursor/support contact, calcination and reduction) can dramatically affect the mechanism(s) by which supported-nanoparticles are formed (vide infra).

2.1.2. Physical methods for following the kinetics of supported-nanoparticle heterogeneous catalyst formation at the gas–solid interface

Nuzzo and co-workers correctly noted [45] that "methods available to characterize the phase dynamics of nanoscale systems are limited". This sentiment was echoed by Chupas et al. who remarked in 2007 that "the kinetics and mechanisms of nanoparticle formation... have been largely overlooked, due to a lack of adequate experimental methodology" [56].

Table 1 highlights the nine physical methods that have been identified by this review for following the kinetics of supported-nanoparticle heterogeneous catalyst formation in real time and at the gas–solid interface. In addition, Table 1 identifies how many times each physical method has been utilized (see Table S1 of the Supporting Information for a full list of papers identified by this review, from which Table 1 was constructed). Table 1 also lists whether each physical method is directly able to monitor M–M bond formation or net $M(0)_n$ nanoparticle formation—if so, that physical method is designated as a "direct method", or if not, an "indirect method". Table 1 also indicates whether each physical method has typically been used in situ or ex situ. Notably, only five direct methods have been utilized to date to follow supported-nanoparticle heterogeneous catalyst formation.

Ideally, the use of multiple, complimentary, direct and in situ—or better yet *in operando*[4] [107–111]—physical methods should be used to monitor all of the catalyst preparation steps and, then, the supported-nanoparticle catalyst formation kinetics.[4] Below, key physical methods for following the kinetics of supported-nanoparticle heterogeneous catalyst formation are discussed (i.e., and based on the literature in Table 1); key advantages and disadvantages of each physical method are also highlighted. In addition, recent advances in transmission electron microscopy (TEM) instrumentation and imaging, ideally *in operando* but if not at least in situ [112–115], promise to prove useful in understanding the mechanisms of supported-nanoparticle heterogeneous catalyst formation.

2.1.2.1. X-ray absorbance fine structure spectroscopy (XAFS): X-ray absorbance near edge spectroscopy (XANES) and extended X-ray absorbance fine-structure spectroscopy (EXAFS). XAFS spectroscopy is a local, average, but generally powerful method for following the kinetics of supported-nanoparticle heterogeneous catalyst formation, one that yields (average) structural information for metal–metal and metal–ligand interactions (Table 1). Of the 39 mechanistic studies regarding supported-nanoparticle heterogeneous catalyst formation listed in Table S1 of the Supporting Information, 18 utilize XAFS to obtain their kinetic data. XAFS is particularly attractive as it can in principle be used in both gas–solid and liquid–solid systems, as well as for all metals and supports of interest. However, one important pitfall to be aware of is that the high energy X-rays can cause beam damage to the sample so that controls should be performed, for example controls varying the beam-exposure time [52].

Another important experimental consideration is the required data acquisition time—is it slow or relatively fast? Early XAFS data were collected by slow monochromator scanning of the entire X-ray range point-by-point in energy space over the course of minutes, making impossible time-resolved experiments on sub-minute time scales [116]. Recently however, quick XAFS (QXAFS, which employs faster scanning) yields data acquisition time scales on the

[4] In principle, all supported-nanoparticle heterogeneous catalyst formation kinetics would be monitored *in operando* (i.e., under working conditions) [107]. The Latin term "*in operando*" implies the "simultaneous evaluation of both catalyst active site structure and catalytic activity/selectivity" [111]. While "catalyst preparation" does not typically occur *in operando*, *ideally it should*, so that at least in some cases the M^{x+} to $M(0)_n$ catalyst formation steps would occur, and be monitored, under the actual catalytic reaction conditions of interest. Such studies would, therefore, also monitor so-called dynamic adsorbate induced restructuring [85]. Hence, and at least in principle, *synthesis* and *monitoring* of all catalyst preparation steps *in operando* should become the norm en route to the next generation of size-, shape- and composition-controlled supported-nanoparticle heterogeneous catalysts.

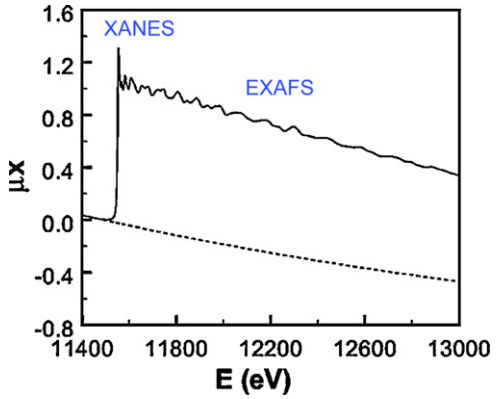

Fig. 1. XAFS spectrum for a Pt foil [118]: μX (measured absorption coefficient) vs. E (eV, energy of the incident X-ray) with the XANES and EXAFS regions identified as shown.
Adapted with permission from [118]. Copyright (2000) Springer.

order of seconds. Moreover, energy-dispersive XAFS (DXAFS, which utilizes a bent monochromator to produce the range of required X-rays, so that scanning is not necessary) yields millisecond data-acquisition time scales [116]. Herein, we will refer to all forms of the experiment, including QXAFS and DXAFS, simply as XAFS, but with it being understood that both QXAFS and DXAFS should be employed as required.

Further details regarding the experimental and theoretical details of the XAFS experiment have been extensively covered in a book edited by Koningsberger and Prins [117]. Hence, in what follows we will focus on the data that can be obtained via XAFS spectroscopy along with the specific strengths and weaknesses of both the XANES and EXAFS components of XAFS for following the kinetics and mechanism(s) of formation of supported-nanoparticle heterogeneous catalysts.

An example XAFS spectrum, shown in Fig. 1, is composed of two distinct regimes, the XANES and EXAFS regimes. XANES is both metal and ligand dependent, and starts with the lowest energy photoinonization process leading to the XANES edge (i.e., the so-called "jump" [117]) and continues up to ~40 eV beyond the initial edge [119] (Fig. 1). XANES provides information on the electronic and geometric properties of the metal of interest, including the relative oxidation state and, in favorable cases, the symmetry environment of the adsorbing atom site [117]. Hence, XANES is poised to probe changes in the formal metal oxidation state, the ligand environment and covalency [119,120], as well as any changes that occur during the supported-nanoparticle heterogeneous catalyst formation reaction. Shown in Fig. 2 is an example, from Gates and co-workers [61], which utilizes XANES to monitor the change over time in the Rh K-edge of $Rh(C_2H_4)_2$ supported on dealuminated zeolite-Y (zeolite-DAY) under H_2 and at 298 K. Unfortunately, XANES is often qualitative, so that precise identification of the formal oxidation state and ligand environment is only obtained in reference to known, structurally well-characterized, model complexes [130]. Advances in XANES fitting theory (e.g., improvements in algorithms and calculation speed) are progressing and should help in ab initio XANES modeling; however, at present XANES is often considered semi-quantitative [121].

The remaining portion of the XAFS spectrum is the EXAFS region (Fig. 1) which arises from the backscattering of excited low kinetic energy (10–40 eV) photoelectrons by neighboring atom(s) at distances up to 4–5 Å, with an accuracy up to ±0.2 Å [117,122]. Overall, EXAFS yields average, local structural information concerning the relative positions of neighboring atom(s), as well as their relative distances and coordination numbers to the adsorbing atom of interest [123]. Hence, EXAFS can follow directly M–M bond

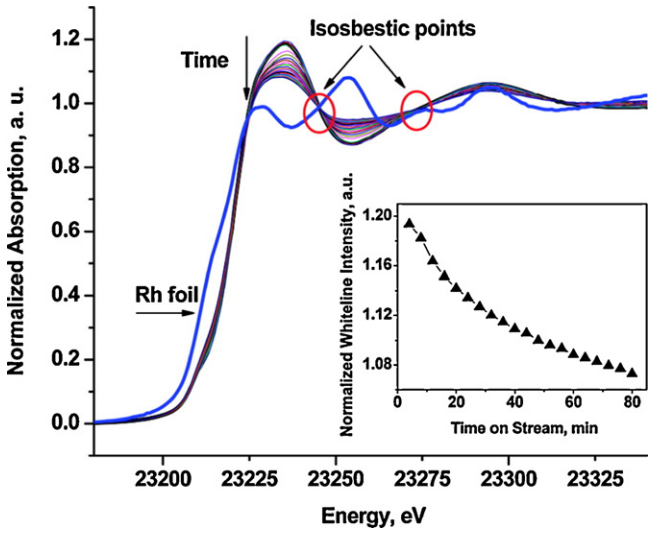

Fig. 2. An excellent example of the changes in a series of raw XANES spectra and the white line intensity (insert) during the reduction of $Rh(C_2H_4)_2$/zeolite-DAY under H_2 (at 298 K) [61].
Reprinted with permission from [61]. Copyright (2008) American Chemical Society.

formation (when appropriate models are used) and, therefore, can follow directly the formation of $M(0)_n$ supported-nanoparticle heterogeneous catalysts. Shown in Fig. 3 is an example of the changes in the Rh–C, $Rh–O_{Support}$ and Rh–Rh coordination numbers over time (under H_2 and at 298 K), extracted from the EXAFS portion of the spectra for the aforementioned $Rh(C_2H_4)_2$ complex supported on dealuminated zeolite-Y system studied by Gates and co-workers. Noteworthy is that each Rh first nearest neighbor (i.e., each of Rh–C, $Rh–O_{Support}$ and Rh–Rh) can be followed in real time, yielding information regarding both the loss of the precursor (i.e., $-d[Rh(C_2H_4)_2]/dt$) and formation of the Rh_n clusters (i.e., $+d[Rh_n]/dt$).

EXAFS is able to follow directly dilute molecular species (e.g., 0.4-wt% Pd on zeolite H-USY has been analyzed [50]). In addition, EXAFS is now commonly used to analyze supported-nanoparticles [123], making it a valuable method for following the kinetics of those supported-nanoparticle formation reactions. Unfortunately, however, EXAFS yields only relative scattering distances and not absolute bond distances; the latter require the use of known model structures and their measured EXAFS or other simulations

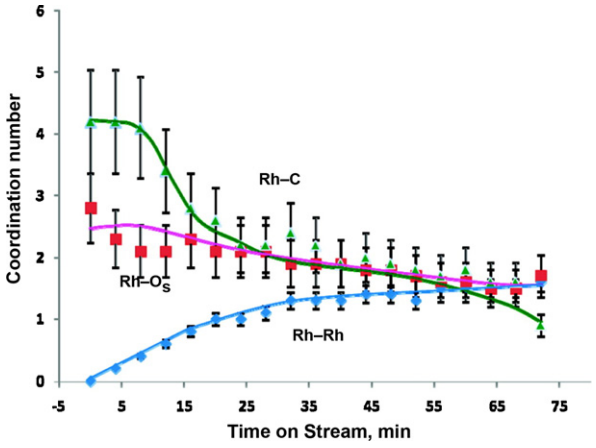

Fig. 3. An example of the changes in Rh–C, $Rh–O_{Support}$ and Rh–Rh coordination numbers obtained from EXAFS spectra of $Rh(C_2H_4)_2$ supported on dealuminated zeolite-Y at 298 K under H_2 and vs. time [61].
Reprinted with permission from [61]. Copyright (2008) American Chemical Society.

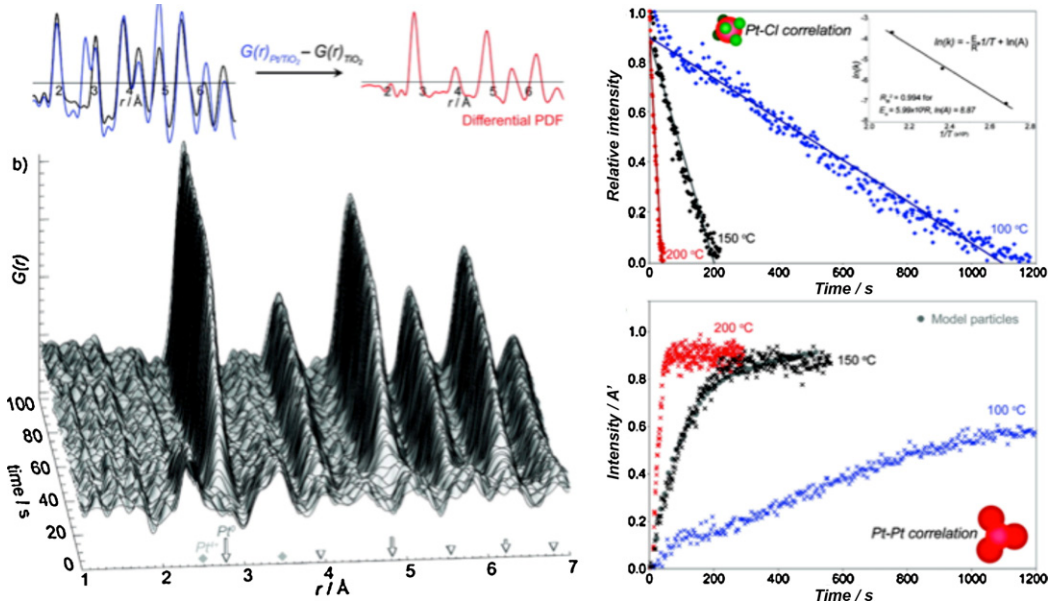

Fig. 4. Kinetic data obtained by the high energy X-ray scattering plus PDF method, from the work of Chupas et al. [56]. Shown to the left is the raw differential (support-subtracted) PDF for the formation of $Pt(0)_n/TiO_2$ under H_2 over time. Shown to the right are the extracted Pt–Cl (top right) and Pt–Pt contributions (bottom right) over time for the formation of $Pt(0)_n/TiO_2$.

Reprinted with permission from [56]. Copyright (2007) American Chemical Society.

typically from known structural data (e.g., from single crystal X-ray structures). Hence, quantitative EXAFS-based structural data are often obtained only when a good fit is observed between a known model structure and the experimental data. However, even in the most favorable cases the fitting procedure (containing up to five fitting parameters per scattering path [117]) can often "lead to more than one statistically valid and physically possible structural model", as Gates and co workers have emphasized [124]. Therefore, EXAFS is often best used only in a complimentary role with several other physical methods. In addition, EXAFS requires the use of synchrotron sources to provide the intense (10^{10} flux vs. 10^3 flux with an X-ray tube) continuum (3–30 keV) of required X-ray radiation [117,125], so it is not yet what one would term a "routine method" available to each and every laboratory at any time.

2.1.2.2. Total high energy X-ray scattering and pair-distribution-function (PDF) analysis. A relatively new[5] and potentially powerful technique for following the kinetics of supported-nanoparticle heterogeneous catalyst formation is total high-energy X-ray scattering coupled with PDF analysis. To date, only two studies (Table 1) have utilized total high-energy X-ray scattering coupled with PDF analysis to follow the formation of supported-nanoparticles [56,66]. Billinge has discussed extensively the experimental and theoretical details of total high-energy X-ray scattering plus PDF analysis [126,127]; hence, only a very brief overview is given below, one largely focused on PDF analysis. The focus herein is, instead, on the data that can be obtained along with our perception of the strengths and weaknesses at present of the total high-energy X-ray scattering plus PDF analysis technique.

Total high-energy X-ray scattering utilizes all of the "structure-relevant" diffraction data from a powder sample, including the Bragg and diffuse scattering components (vs. just the Bragg scattering components in conventional powder X-ray diffraction analysis) [128]; high-energy X-rays are required for adequate real-space resolution from the sample [129]. The experimentally measured scattering function (i.e., background subtracted and normalized), termed the total scattering function $S(Q)$, is given by Eq. (1):

$$S(Q) = \frac{I^{coh}(Q) - \sum c_i \left|f_i(Q)\right|^2}{\left|\sum c_i f_i(Q)\right|^2} \quad (1)$$

In Eq. (1), c_i is the atomic concentration, f_i is the X-ray atomic form factor, $I^{coh}(Q)$ is the measured scattering intensity from a powder sample, and $Q = 4\pi \sin(\lambda)/\theta$ [126,127]. Billinge has noted that "it is worth remembering that $S(Q)$ is nothing other than the powder diffraction pattern that has been corrected for experimental artifacts and suitably normalized" [127].

Through a Fourier transform over a measured range Q, the $S(Q)$ is transformed into the atomic PDF ($G(r)$, Eq. (2)) [126,127]:

$$G(r) = 4\pi r[\rho(r) - \rho_0] \quad (2)$$

In Eq. (2), $\rho(r)$ is the local atomic number density, ρ_0 is the average atomic number density and r is the radial distance. Hence, $G(r)$ is a representation of the coherent scattering of the total diffracted intensity of the material and, physically, contains information regarding the distances between pairs of atoms [129]. The atomic PDF ($G(r)$) data are then modeled to obtain quantitative structural information [128].

Fig. 4 (left) shows an illustrative example, reported by Chupas et al. [56], of raw and differential (i.e., support-subtracted) atomic PDF data vs. time for the formation of $Pt(0)_n/TiO_2$ under H_2 (at 200 °C). From the differential atomic PDF data, *local* Pt–Cl (at 2.5 Å) and Pt–Pt (at 2.77 Å) atomic pair correlations can be extracted (Fig. 4 (right)). While not shown, it is also possible to obtain further, atomically resolved, structural information—such as nanoparticle size or number of atoms per particle—via the Pt–Pt atomic pair correlations without the need of infinite periodicity (see, for example, the Supporting Information of Chupas et al.'s paper [56]). Specifically, the X-ray scattering plus PDF method can yield atomic resolution information at length scales up to 10 nm (i.e., at the nanoscale) for either crystalline or noncrystalline materials [129,130]. Hence, the total high-energy X-ray scattering plus PDF method is

[5] While the PDF analysis method is not new, its recent coupling with the total high-energy X-ray scattering data has allowed that coupling to become increasingly valuable for the analysis of complex materials [130].

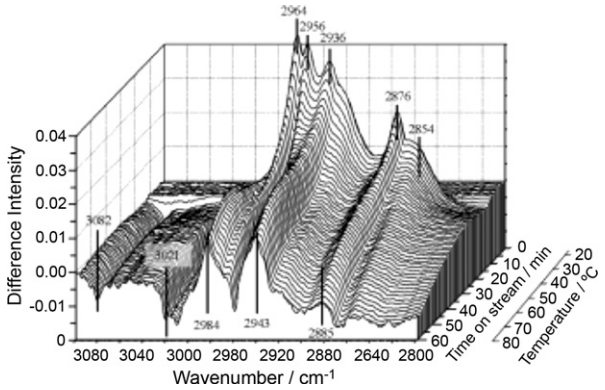

Fig. 5. An example of IR spectral data obtained for the formation and loss of ethyl ligands (shown at 2964, 2936, 2876 and 2854 cm^{-1}) from $Ir(C_2H_4)_2$/zeolite-Y under H_2 and a temperature ramp.
Reproduced with permission from [60]. Copyright (2008) Wiley-VCH.

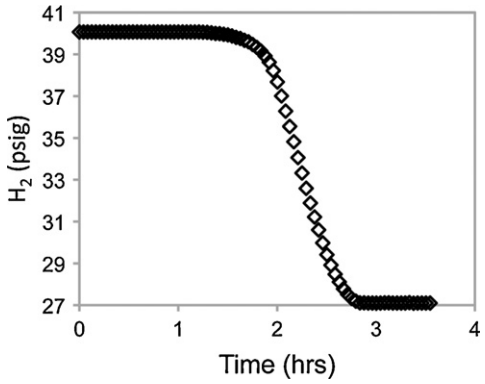

Fig. 6. An example of H_2 uptake kinetics following the formation of $Pt(0)_n/\gamma$-Al_2O_3 [72]. The sigmoidal kinetics [72] and cyclohexene reporter reaction method employed will be discussed in Section 3.2.2.3.
Adapted with permission from [72]. Copyright (2009) American Chemical Society.

complimentary to EXAFS (with its local ~0.5–1 nm scale) and X-ray diffraction (XRD, with its long range bulk analysis, >10 nm).

The total high-energy X-ray scattering plus PDF analysis method clearly has several advantages, including: (i) the ability to follow directly both the loss of a metal precursor complex and the formation of $M(0)_n$ nanoparticles; (ii) the atomically resolved, absolute bond distances, which result are not model dependent; and (iii) the fact that this method can be used in situ (and, in principle, *in operando*). Despite these advantages, as with any technique, disadvantages exist, including: (i) the need for synchrotron sources; (ii) the challenge of quantitative analysis of the data (such analysis can take a significant amount of time, presently up to even 1–2 years in the case that we are aware of, as discussed in footnote 16 of reference [72]); and (iii) "...the limitation brought by inadequate data analysis software" [128]. More specific to the heterogeneous catalysis community, (iv) there is also the limitation that loadings below 5 wt% have proven difficult to analyze, at least to date [66]. Despite this, total high-energy X-ray scattering plus PDF analysis is a powerful, evolving method that holds considerable promise for monitoring the formation of supported-nanoparticle heterogeneous catalysts. Hence, its enhanced use, especially as a complement to other direct physical methods such as XAFS and XRD and even indirect methods (such as IR spectroscopy, H_2 uptake or others, vide infra), can be anticipated.

2.1.2.3. Infrared (IR) spectroscopy. IR spectroscopy relies on the absorption of infrared light by vibrational levels within a molecule of interest. The theoretical details of IR spectroscopy can be found in many textbooks [3,131,132]. The experimental details regarding measuring IR spectra of supported-metal complexes and supported-nanoparticles have been recently and expertly discussed by Gates and co-workers [133].

Five studies in Table S1 have utilized IR spectroscopy to follow the kinetics of the loss of a supported-precatalyst [29,51,60,61,64]. An example is that of $Ir(C_2H_4)_2$ on zeolite-Y from Gates and co-workers [60] (Fig. 5). The peaks at 2964, 2936, 2876 and 2854 cm^{-1} show the formation of ethyl ligands on the Ir/zeolite-Y (from the $Ir(C_2H_4)_2$/zeolite-Y precatalyst) and subsequent loss of those ethyl ligands over 1 h under H_2 (and with a temperature ramp).

Importantly, IR spectroscopy often yields information regarding the ligand shell of a supported-metal precatalyst (and, therefore, is highly complementary to the methods that are capable of following M–M bond or net $M(0)_n$ nanoparticle formation directly). IR spectroscopy has not been used to follow the formation of M–M bonds during supported nanoparticle formation, since support vibrations often overlap with the M–M bond vibrations of interest, and is in that sense and as defined before "indirect". However, IR spectroscopy is particularly useful when supported-organometallics are present that contain CO or hydrocarbon ligands [133]. Additional advantages of IR spectroscopy include its ease of use, broad availability and value in routine, first-screenings of the kinetics of loss of the supported-organometallic or other precatalysts.

2.1.2.4. H_2 uptake kinetics: a chemical-based method. Early literature studies trying to understand supported-nanoparticle heterogeneous catalyst formation kinetics, as well as the associated M^{x+} reduction reaction, relied on H_2 uptake monitoring. More specifically, eight studies in Table S1 [30–35,37,52] utilized H_2 uptake measurements to obtain their kinetic data. The H_2 uptake experiment is in principle simple: the material of interest is placed in a closed vessel, exposed to H_2 and either a change in the pressure, or the H_2 uptake in an apparatus that maintains constant pressure, is measured quantitatively. Under the appropriate conditions, H_2 uptake kinetic data (for example when coupled to a reporter reaction, vide infra) can reveal information about supported-nanoparticle heterogeneous catalyst formation [72,74,75]. Shown in Fig. 6 is an example where H_2 uptake kinetic measurements were employed to follow $Pt(0)_n/\gamma$-Al_2O_3 supported-nanoparticle formation indirectly but in real time with hundreds to thousands of high-precision data points [72].

The largest advantage of using H_2 uptake as a kinetic monitoring method is its ease of use, ready availability, and sample compatibility (e.g., both solids and liquids are readily analyzed). Another advantage is that H_2-uptake measurements of just the precatalyst can yield information regarding the crucial stoichiometry of the supported-nanoparticle formation reaction. These advantages so noted, the two greatest disadvantages of the H_2-uptake method are its indirect nature and the thermodynamic constraints when using H_2 as a reductant. An example of the latter constraint arises when cheaper, earth-abundant first-row metal catalysts made from Co (−0.28 V vs. NHE) and Ni (−0.257 V vs. NHE) are present; these metals are not reducible thermodynamically by H_2 to the M(0) state, at least under mild, room temperature and standard (1 atm) pressure conditions.

2.1.2.5. Electron microscopy. Transmission electron microscopy (TEM) is one of the most commonly used imaging methods for analyzing supported-nanoparticle heterogeneous catalysts or, for that matter, nanoparticle catalysts made in solution and then deposited for ex situ analysis on a TEM grid [134]. In general, TEM provides largely direct and powerful, albeit historically ex situ, images of the presumed catalyst (or, more often, the O_2-exposed, possibly oxidized form of the $M(0)_n$ nanoparticle). Concerns with this method

include (i) the possibility of electron beam induced damage as "in the end you can damage virtually anything you put into the TEM" [135], (ii) the ex situ nature of a typical TEM experiment (which has made it largely ineffective for following the kinetics of the formation of supported-nanoparticles), and (iii) the "non-canonical ensemble" nature of TEM measurements (i.e., the ability to see even single nanoparticles that may be grossly unrepresentative of the bulk sample). Hence, such potential disadvantages necessitate the use of appropriate control experiments.

Recent advances[6] in the design of environmental TEM cells have allowed in situ TEM measurements under non-high-vacuum conditions [112,136]. For example, Creemer and co-workers recently studied the reduction of the well-known CuO/ZnO methanol synthesis precatalyst [3] in situ, under 1.2 bar H_2 (approximately atmospheric pressure), at temperatures up to 500 °C and at a resolution of 0.18 nm. The reduction of CuO to Cu(0) on the ZnO surface [113] could be directly imaged; the migration of 5–10 nm $Cu(0)_n$ nanoparticles on the ZnO support was also observed.

In another recent study, Alivisatos and co-workers employed an in situ, liquid-based cell to study the growth of $Pt(0)_n$ nanoparticles from Pt(acetylacetonate)$_2$. Their studies revealed both monomer addition and bimolecular aggregation [114], albeit without a support present. A limitation exposed via that study is that the TEM electron beam is involved in inducing the nanoparticle formation reaction either directly, through solvated electrons, or possibly via an oleylamine-assisted pathway, oleylamine being present as the solvent [114]. In one additional in situ TEM study worth noting, the detection of several intermediate phases from amorphous $LiFePO_4$ en route to crystalline $LiFePO_4$ [115] demonstrated the ability of TEM to directly image intermediate nanoparticle phases en route to the final product. Overall, then, environmentally controlled TEM cells [112,136][6] promise to make additional contributions to our understanding of how supported-nanoparticle heterogeneous catalysts form.

2.1.3. Conclusions

Clearly, each of the precatalyst preparation steps—that is, precursor/support contact, calcination and reduction—has the potential to influence the supported-nanoparticle heterogeneous catalyst formation speciation and resultant kinetics. Overall, speciation-controlled, supported-metal precatalysts are needed for the next generation syntheses of supported-nanoparticles as well as for reliable kinetic studies of their formation reaction(s).

A variety of advanced techniques, including EXAFS, XANES, total high-energy X-ray scattering plus PDF analysis, as well as in situ TEM are emerging as viable, often complimentary options for following the stoichiometries and the kinetics of formation of supported-nanoparticle heterogeneous catalysts. In addition, any technique capable of in situ, or better *in operando*,[4] measurements can in principle be used to follow the stoichiometries and kinetics, thereby helping deduce the mechanism(s) of supported-nanoparticle heterogeneous catalyst formation reactions.

IR spectroscopic and H_2 uptake studies are the two-quicker/easier methods that have been used to date to follow supported-nanoparticle formation reactions. However, care must be taken in such indirect studies to ensure that the desired supported-nanoparticle heterogeneous catalyst formation reaction is what is actually being monitored.

Overall however, there is still a need to develop more routine, "available-in-any-lab" methods to follow supported-nanoparticle formation stoichiometries and kinetics. A broader availability of more routine, ideally direct methods would ensure that only the most important systems are thereby indentified and developed, so that only those "best" systems can then be subjected to the more expensive and time-consuming, but more powerful and direct techniques, including XAFS, high energy total X-ray scattering plus PDF analysis and in situ TEM. Furthermore, the inherently complex nature of supported-nanoparticle heterogeneous catalyst formation problem demands the use of multiple, complimentary physical methods to follow the stoichiometries, kinetics and thereby deduce reliable mechanisms for those supported-nanoparticle formation reactions.

2.2. Kinetic and mechanistic studies of practical supported-nanoparticle heterogeneous catalyst formation at the gas–solid interface

2.2.1. Brief overview of the primary literature

Table S1 of the Supporting Information is a compilation of 39 primary literature references reporting kinetic and mechanistic studies of supported-nanoparticle formation at the gas–solid interface [29–67]. For what follows we have chosen four representative systems, organized by the supported-metal precatalyst used. The systems are covered in 25 of the 39 references in Table S1 and are four systems which provide a good overview of the best-studied systems in the literature. Those 25 papers are shown in Table 2 along with: (i) experimental details of the preparation of the supported metal precatalyst and, then, the details of the supported-nanoparticle heterogeneous catalyst formation reaction; (ii) information on whether the study contains kinetic data (and, if so, the physical method employed); and if kinetic data were obtained, then also (iii) information on whether those data were collected isothermally or non-isothermally. While classical chemical kinetics are traditionally performed isothermally, non-isothermal kinetic measurements are common in the supported-nanoparticle formation literature—the precise interpretation, and hence the resultant exact meaning and value, of which are currently being actively debated [137–141].[7] Also given in Table 2 is (iv) whether the stoichiometry of the supported-nanoparticle heterogeneous catalyst formation reaction was explicitly demonstrated (and if so, how that stoichiometry was obtained as a guide for future studies); and (v) the rate equations and proposed mechanism as given by the original authors (if available).

Before discussing each of the four case studies in detail, a brief overview of Table 2 is quite informative and reveals several insights into the state of mechanistic knowledge for supported-nanoparticle heterogeneous catalyst formation. Specifically, while 24 of the 25 studies in Table 2 contain kinetic data, 9 of those 24 studies were done under non-isothermal reduction conditions [137]. In addition, only 10 of the 25 studies rigorously

[6] Also worth mentioning here are the recent advances in electron sources, dampening and aberration correction that have improved TEM resolution [136].

[7] One sub-goal of kinetic studies is to obtain the Arrhenius parameters for the chemical reaction of interest—that is, the activation energy (E_a) and pre-exponential factor (A). This is commonly done by collecting a series of isothermal kinetic curves (i.e., the change in the reactants or products with time), from which rate constants, k, are extracted. A subsequent plot of the $\ln k$ vs. $1/T$ then yields the well-known E_a (the slope of the line equals $-E_a/R$) and A (the y-intercept equals $\ln(A)$). Another possibility is to measure the kinetic curve during a temperature ramp, that is non-isothermally. This approach is attractive as, at least in principle, the E_a, A and k can be determined from a single experiment [138]. Hence, the heterogeneous catalysis community has utilized such non-isothermal kinetic measurements to try and understand the mechanisms of supported-nanoparticle formation [137], as Table 2 makes apparent. However, the utility and treatment of non-isothermal kinetic data, particularly for understanding mechanism, is under current debate. Galwey has argued that it is simply not possible, in general, to obtain the E_a, A and k from a single non-isothermal kinetic experiment [141]. Galwey and Brown have also noted that the isothermal treatment of kinetic data "requires fewer assumptions and results appear to be more consistent and reliable" [138].

Table 2
The twenty-five primary case studies, of four main systems, investigated herein which report the kinetics and mechanisms of formation of supported-nanoparticle catalysts at the gas–solid interface. A full list of the 39 presently available studies, from which these 25 case studies were chosen, is available in Table S1 of the Supporting Information.

Entry [Reference]	Authors	System studied	Kinetic data (physical method employed)	Isothermal kinetic data	Stoichiometry (physical method employed)	Proposed mechanism(s) and rate equations as written by the original authors (if available)
$M(NH_3)_4^{2+}$ based systems						
1[29]	Dalla Betta, R.A.; Boudart, M.	5-wt% $Pt(NH_3)_4Cl_2$ was ion-exchanged onto zeolite-Y and reduced under H_2 from 25 to 350 °C. The effects of calcination and H_2O were also investigated.	Yes (IR spectroscopy)	No	Yes (H_2 uptake)	*Proposed mechanism*. Aggregation is proposed to be due to "the unstable neutral, hence mobile, hydride (i.e., Pt–H), which leads to Pt agglomeration", as shown in Scheme 3.
2[39]	Tzou, M.S.; Sachtler, W.M.H.	7.4-wt% $Pt(NH_3)_4Cl_2$ was ion-exchanged onto zeolite NaY. The resultant precatalyst was calcined between 360 and 550 °C and reduced under H_2 at 500 °C.	Yes (H_2 chemisorption)	Yes	No	*Proposed mechanism of subnanometer $Pt(0)_n$/zeolite-Y formation*. Calcination at 360 °C afforded Pt^{2+} ions in the zeolite supercages, which are easily reduced with H_2 between −15 and 150 °C. "Growth" kinetics were obtained by monitoring the change in the Pt dispersion by H_2 chemisorption. The H_2 chemisorption data "favor the mechanism of particle growth by migration and coalescence of particles rather than Ostwald ripening, that is by atomic migration". *Proposed mechanism of 10–50 nm $Pt(0)_n$/zeolite-Y formation*. Calcination at 550 °C afforded Pt^{2+} ions in the sodalite cages. The Pt^{2+} ions are reduced and driven to a location where $Pt(0)_n$ particles can form. "Two stages can be discerned: (a) nucleation, and (b) growth of particles". The Pt(0) atoms can migrate to the surface of the zeolite.
3[41]	Homeyer, S.T.; Sachtler, W.M.H.	2–7-wt% $[Pd(NH_3)_4](NO_3)_2$ was ion-exchanged onto zeolite NaY. The sample was calcined at 250 and 500 °C and then reduced under a temperature ramp from −80 to 350 °C.	No		Yes (H_2 Uptake)	*Proposed mechanism when Pd ions are in the supercages*. "Pd ions migrate to an activated nucleus where they are reduced, forming primary particles. These migrate through the supercage network until they either contact another primary or secondary particle. Once all the primary particles are used up, further growth of the secondary particles occurs via a different mechanism, possibly involving Ostwald ripening or local collapse of the zeolite matrix". *Proposed mechanism when Pd ions are in the sodalite cages*. "Pd atoms are released into the supercage network at higher temperatures, where they form secondary particles either through migration and coalescence or by trapping Pd atoms as they leave the sodalite cages".
4[47]	Oudenhuijzen, M.K.; Kooyman, P.J.; Tappel, B.; van Bokhoven, J.A.; Koningsberger, D.C.	1-wt% $[Pt^{2+}(NH_3)_4](NO_3^-)_2$ was impregnated onto SiO_2 by incipient wetness. The precatalyst was dried under N_2 for 1 h at room temperature, followed by 8 h at 80 °C. The precatalyst is then reduced with H_2 under a temperature ramp from room temperature to 400 °C.	Yes (XANES and EXAFS)	No	No	*Proposed mechanism*. The final size of the Pt particles (when reduced under H_2) is controlled by two parameters, the nucleation rate and the growth rate. "Since the formation of metal–metal bonds adds significantly to the stability of Pt atoms, the reduction of the $Pt^{2+}(NH_3)_x$ complex must involve migration and collision of the Pt^{2+} species with either an earlier formed metallic Pt nucleus or several other Pt^{2+} complexes and reduced at the same moment". The authors propose that a highly mobile Pt–H species is responsible for the nanoparticle growth, analogous to that reported by Dalla Betta and Boudart [29].

Table 2 (*Continued*)

Entry [Reference]	Authors	System studied	Kinetic data (physical method employed)	Isothermal kinetic data	Stoichiometry (physical method employed)	Proposed mechanism(s) and rate equations as written by the original authors (if available)
5[50]	Okumura, K.; Yoshimoto, R.; Uruga, T.; Tanida, H.; Kato, K.; Yokota, S.; Niwa, M.	0.4-wt% $Pd(NH_3)_4Cl_2$ was ion-exchanged onto zeolite Na–ZSM-5, H–ZSM-5 and Y–mordenite. The samples were oxidized at 773 K and then reduced in H_2 up to 750 K.	Yes (EXAFS)	No	No	No mechanism was proposed for the supported-nanoparticle heterogeneous catalyst formation reaction.
6[58]	Okumura, K.; Kato, K.; Sanada, T.; Niwa, M.	0.4 and 0.8-wt% $Pd(NH_3)_4Cl_2$ was ion-exchanged onto zeolite H–USY. The samples were calcined under O_2 at 773 K for 4 h and reduced with H_2 under a temperature ramp from room temperature to 773 K.	Yes (EXAFS)	No	Yes (XANES)	No mechanism was proposed for the supported-nanoparticle heterogeneous catalyst formation reaction.
7[62]	Okumura, K.; Honma, T.; Hirayama, S.; Sanada, T.; Niwa, M.	0.4 and 0.8-wt% $Pd(NH_3)_4Cl_2$ was ion-exchanged onto zeolite H–USY. The samples were dried at 323 K under atmospheric conditions and reduced under H_2 at 300 K.	Yes (XANES and EXAFS)	Yes	Yes (XANES)	No mechanism was proposed for the supported-nanoparticle heterogeneous catalyst formation reaction.
8[63]	Okumura, K.; Matsui, H.; Sanada, T.; Arao, M.; Honma, T.; Hirayama, S.; Niwa, M.	0.4-wt% $Pd(NH_3)_4Cl_2$ was ion-exchanged onto zeolite H–USY, dried at 323 K under atmoshpere and reduced under H_2 at 300 K. Precatalysts containing $PdCl_2$, $Pd(OAc)_2$ and $Pd(NH_3)_4(NO_3)_2$ on zeolite H–USY were also investigated.	Yes (XANES and EXAFS)	Yes	Yes (XANES)	No mechanism was proposed for the supported-nanoparticle heterogeneous catalyst formation reaction.
H_2PtCl_6 based systems						
9[38]	Dexpert, H.	H_2PtCl_6 was impregnated onto Al_2O_3. The samples were reduced under H_2 at room temperature or 200 °C.	Yes (XANES and EXAFS)	Yes	No	*Proposed mechanism*. A summary of the author's word-based mechanism for the "decomposition of the isolated $PtCl_6^{2-}$ complexes" is: (i) oxygen starts to replace the chlorine atoms; (ii) a chlorinated Pt dimer is formed; and (iii) the dimer grows as the reduction continues.
10[40]	Le Normand, F.; Bazin, D.; Dexpert, H.; Lagarde, P.; Bournonville, J.P.	H_2PtCl_6 was impregnated onto γ-Al_2O_3. The catalyst was dried at 120 °C and reduced under H_2 at 300 °C.	Yes (XANES and EXAFS)	Yes	No	No mechanism was proposed, but qualitatively the authors state that: (i) "the reduction rate tends to increase with the time of isothermal reduction", which may be due to spillover, and (ii) that "the isothermal reduction is associated with the growth of Pt clusters".
11[56]	Chupas, P.J.; Chapman, K.W.; Jennings, G.; Lee, P.L.; Grey, C.P.	5-wt% H_2PtCl_6 was deposited on TiO_2 via incipient wetness. The samples were dried overnight at 60 °C and reduced under H_2 at 100, 150 and 200 °C.	Yes (total high energy X-ray scattering + PDF analysis)	Yes	No	No mechanism was proposed for the supported-nanoparticle heterogeneous catalyst formation reaction.
12[65]	Shishido, T.; Asakura, H.; Amano, F.; Sone, T.; Yamazoe, S.; Kato, K.; Teramura, K.; Tanaka, T.	H_2PtCl_6 was impregnated on TiO_2 or γ-Al_2O_3 (5-wt%), dried at 353 K and calcined at 773 K. Subsequently the samples were pulsed with 5 mL of H_2 for 20 s at 473 K.	Yes (DXAFS)	Yes	Yes (XANES)	No mechanism was proposed for the supported-nanoparticle heterogeneous catalyst formation reaction.
13[66]	Chupas, P.J.; Chapman, K.W.; Chen, H.; Grey, C.P.	2.5–7.5-wt% H_2PtCl_6 was impregnated onto TiO_2 and dried at 60 °C overnight. Some of the samples were calcined at 200 °C for 2 h under O_2. The kinetic data were collected while the sample was being reduced in H_2 from 0 to 227 °C.	Yes (high energy total X-ray scattering + PDF analysis)	No	No	*Proposed mechanism*. "The initial Pt nanoparticles that form are ~1 nm in size, while by 200 °C are larger and more crystalline. This suggests a mechanism for particle growth where the initial particles that form are small (<1 nm) then agglomerate into ensembles of many small particles and lastly anneal to form larger well-ordered particles".

$Ag(NO)_3$ zeolite based systems						
14[32]	Beyer, H.; Jacobs, P.A.; Uytterhoeven, J.B.	$AgNO_3$ is ion-exchanged on zeolite NaY and reduced under H_2. Prior to reduction the samples were out gassed and calcined at 373, 473 and 623 K and subsequently reduced under H_2 isothermally between 298 and 623 K.	Yes (H_2 uptake)	Yes	Yes (H_2 uptake)	*Observed rate law: low temperature* (≤430 K) $\frac{dc}{dt} = k'P\frac{C_0'-C}{C}$ P is the H_2 pressure, C_0' the initial Ag^+, and C is the reduced form of Ag^+ at time t. *Proposed mechanism #1 (low temperature): H_2 activation on Ag^+* $H_2 + Ag^+ \rightleftharpoons (Ag^+H^-) + H^+$ $(Ag^+H^-) \xrightarrow{RDS} (Ag^0H)$ $Ag^+ + (Ag^0H) \rightleftharpoons H^+ + Ag_2$ *Proposed mechanism #2 (low temperature): H_2 activation at some surface site, S* $H_2 + S \rightleftharpoons (SH–H)$ $(SH–H) + Ag^+ \rightleftharpoons (SH–Ag) + H^+$ $(SH–H) + Ag^+ \xrightarrow{RDS} S + H^+ + 2Ag$ *Observed rate law: high temperature* (>430 K) $\frac{dc}{dt} = k_1(C_0 - C)$ C_0 is the initial Ag^+ and C is the reduced form of Ag^+ at time t. Proposed mechanism (high temperature). The reduction is "rate-controlled by the migration of Ag^+ ions" to activated H_2 somewhere within the zeolite.
15[36]	Hermerschmidt, D.; Haul, R.	$AgNO_3$ was ion-exchanged onto zeolites X and A. The samples were dehydrated under O_2 at 400 °C and reduced under H_2 isothermally between −50 and 400 °C.	Yes (ESR)	Yes	No	No mechanism was proposed for the supported-nanoparticle heterogeneous catalyst formation reaction.
16[37]	Beyer, H.K.; Jacobs, P.A.	$Ag(NO)_3$ was ion-exchanged onto the chabsite zeolite. The samples were isothermally reduced under H_2 at varying temperatures between 295 and 613 K.	Yes (H_2 uptake)	Yes	Yes (H_2 uptake)	*Observed rate law* $\frac{d[Ag^+]}{dt} = k[Ag^+]^2[P_{H_2}]^{1/2}$ *Proposed mechanism* $H_2 \rightleftharpoons 2H^\bullet$ $H^\bullet + Ag^+ \rightleftharpoons [Ag(0)H^+]$ $[Ag(0)H^+] + Ag^+ \overset{RDS}{\rightleftharpoons} Ag_2^+ + H^+$
17[42]	Schoonheydt, R.A.; Leeman, H.	$AgNO_3$ was ion-exchanged onto zeolite NaA. The samples were calcined at 673 K and reduced under H_2 between 253 and 298 K. All manipulations were carried out in the dark.	Yes (ESR)	Yes	No	*Proposed mechanism* $Ag + Ag \rightarrow Ag_2 \rightarrow Ag_3$, etc.
18[57]	Shimizu, K.-I.,; Sugino, K.; Kato, K.; Yokota, S.; Okumura, K.; Satsuma, A.	$AgNO_3$ was ion-exchanged onto zeolite H-MFI. The sample was dried at 383 K for 24 h, calcined at 823 K for 2 h and reduced under H_2 at 573 K.	Yes (EXAFS and UV–vis)	Yes	Yes (H_2 uptake)	No mechanism was proposed for the supported-nanoparticle heterogeneous catalyst formation reaction.
Supported-organometallic systems						
19[45]	Nasher, M.S.; Frenkel, A.I.; Somerville, D.; Hills, C.W.; Shaplye, J.R.; Nuzzo, R.G.	1–2-wt% $PtRu_5C(CO)_{16}$ was deposited on carbon black via incipient wetness from THF. The sample was allowed to dry in air for 1 h and evacuated for 1 h and reduced under H_2 from 150 to 773 K.	Yes (XANES and EXAFS)	No	No	*Proposed mechanism*. "...the initial nucleation of a compact (Pt-rich) structure (is) followed by the inversion of the intraparticle distribution of the Pt and Ru atoms upon continued high-temperature annealing. In this inversion, the core-segregated Pt atoms exchange with Ru surface atoms to form a surface Pt shell structure".
20[48]	Fiddy, S.G.; Newton, M.A.; Campbell, T.; Dent, A.J.; Harvey, I.; Salvini, G.; Turin, S.; Evans, J.	5-wt% $Pt(acac)_2$ was slurried onto SiO_2 from toluene. The solvent was then removed by rotary evaporation and reduced under H_2 from 300 to 673 K. The authors also looked at a bimetallic system of $Pt(acac)_2$ plus $GeBu_4$.	Yes (EXAFS)	No	No	*Proposed mechanism*. "...an initial decomposition of a small fraction of the supported $Pt(acac)_2$ leading to the formation of a low level of small Pt particles... (which are) active for rapid H_2 dissociation and subsequent spillover of atomic hydrogen".

Table 2 (*Continued*)

Entry [Reference]	Authors	System studied	Kinetic data (physical method employed)	Isothermal kinetic data	Stoichiometry (physical method employed)	Proposed mechanism(s) and rate equations as written by the original authors (if available)
21[51]	Li, F.; Gates, B.C.	1-wt% $Ir(CO)_2(acac)$ was deposited on zeolite NaY from a pentane solution. The solvent was removed by evacuation and put under CO at 40 °C.	Yes (IR spectroscopy)	Yes	No	No specific mechanism was proposed for the formation of $Ir_4(CO)_{12}$ on zeolite NaY.
22[60]	Uzun, A.; Gates, B.C.	1-wt% $Ir(C_2H_4)_2(acac)$ was contacted onto dealuminated zeolite-Y from a n-pentane slurry. The solvent was removed under vacuum and the sample was reduced under H_2 in a temperature ramp from 298 to 353 K.	Yes (XANES, EXAFS and IR spectroscopies)	No	No	*Proposed mechanism*. A model was proposed for the formation of $Ir_4(ligand)_x$/zeolite-Y that goes through a $Ir_2(ligand)_x$/zeolite-Y intermediate. A pictorial representation, as proposed by the original authors, is given in Scheme 10.
23[61]	Liang, A.J.; Gates, B.C.	1-wt% $Rh(C_2H_4)(acac)$ was contacted onto dealuminated zeolite-Y from a n-pentane slurry. The solvent was removed under vacuum and the sample was reduced under H_2 at 298 K.	Yes (XANES, EXAFS and IR spectroscopies)	Yes	No	No mechanism was proposed for the supported-nanoparticle heterogeneous catalyst formation reaction.
24[64]	Kulkarni, A.; Gates, B.C.	1-wt% of each $Os_3(CO)_{12}$ and $Ru_3(CO)_{12}$ (by metal) were simultaneously deposited onto MgO from pentane. The solvent was removed under vacuum and reduced under H_2 in a temperature ramp from 298 to 423 K.	Yes (XANES, EXAFS and IR spectroscopies)	No	No	*Proposed mechanism*. "First, the decarbonylation of triruthenium clusters (occurs) starting at 333 K (with the triosmium carbonyl clusters still being coordinatively saturated and intact). The coordinatively unsaturated ruthenium species were reactive, and at 333 K, had aggregated substantially so that the average ruthenium cluster was larger than trirutheim. When the temperature had been raised to about 358 K, the triosmium clusters began to undergo decarbonylation, and at approximately 398 K the triosmium clusters had lost enough CO ligands to become sufficiently coordinatively unsaturated to allow migration and reaction with Ru atoms of neighboring species", as pictorially depicted in Scheme 11.
25[67]	Nassreddine, S.; Bergeret, G.; Jouguet, B.; Geantet, C.; Piccolo, L.	1.0-wt% $Ir(acac)_3$ was contacted with amorphous silica–alumina (ASA) from toluene. The sample was dried at 120 °C overnight and reduced in flowing H_2 at 350 °C for 6 h.	Yes (in situ XRD)	Yes	Yes (mass spectrometry)	No mechanism was proposed for the supported-nanoparticle heterogeneous catalyst formation reaction.

demonstrated the supported-nanoparticle heterogeneous catalyst formation stoichiometry—the first, key step in any reliable mechanistic study, since that stoichiometry is what the proposed mechanistic steps must sum to! Perhaps most strikingly, only 3 of the 25 studies in Table 2 contain rigorous, chemical-reaction-based mechanisms (i.e., vs. their less useful word-only or picture-based mechanisms[8]). Chemical-reaction-based mechanisms are the hallmark of rigorous mechanistic chemistry in, for example, physical organic [24], organometallic [25,26] and inorganic chemistries [27,28]. From this brief overview alone of the literature in Table 2, one can conclude that the present state of knowledge, of how supported-nanoparticle catalysts form, is still in an early, somewhat rudimentary, stage.

2.2.2. Kinetic and mechanistic case studies

2.2.2.1. System I: $M(NH_3)_4^{2+}$ based systems (where M = Pt and Pd). Interest in $Pt(0)_n$ and $Pd(0)_n$ zeolite-supported-nanoparticle catalysts derives from their use as shape-selective isomerization, hydrogenation and hydrocracking catalysts [3,98,142,143]. Jacobs has insightfully noted that; "the solid-state transformations of Pt and Pd ions in zeolites are understood qualitatively... however, the detailed chemical reactions involved have not been elucidated quantitatively" [155]. He also noted that "in order to establish the dispersion of metals in zeolite cages, it is necessary to understand the reduction mechanism" [153]. We have found eight papers in the literature [29,39,41,47,50,58,62,63], detailed in Table 2 as Entries 1–8, that focus on the kinetics and mechanisms of $M(0)_n$/support supported-nanoparticle heterogeneous catalyst formation starting from the $M(NH_3)_4^{2+}$/support precatalyst (or from closely related derivatives such as $M(NH_3)_{4-x}(H_2O)_x$).

In a classic 1973 paper, shown in Entry 1 of Table 2, Dalla Betta and Boudart investigated the formation of nanometer and subnanometer $Pt(0)_n$ sized particles from $Pt(NH_3)_4^{2+}$ and all supported on zeolite-Y [29]. The $Pt(0)_n$/zeolite-Y products were analyzed via H_2 chemisorption measurements; approximately[9] 14 nm $Pt(0)_n$/zeolite-Y nanoparticles were found when the precatalyst was reduced under H_2 using a temperature ramp from 25 to 350 °C. In contrast, much smaller, approximately[9] 0.9 nm $Pt(0)_n$ nanoparticles were found when the sample was first calcined in O_2 at 350 °C and then reduced in a H_2 temperature ramp from 25 to 400 °C. The observed, varying, $Pt(0)_n$/zeolite-Y product provides one specific example of how the precatalyst preparation conditions can significantly affect the resultant supported-nanoparticle products.

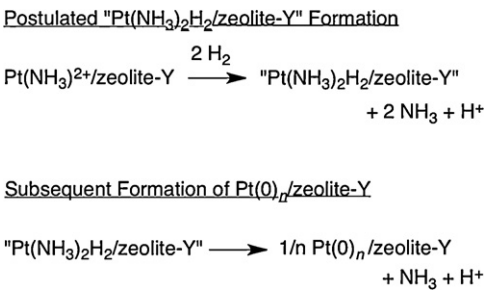

Scheme 3. Formation of Dalla Betta and Boudart's postulated "unstable neutral, hence mobile, hydride" (top) which is proposed to cause aggregation to $Pt(0)_n$/zeolite-Y supported-nanoparticles [29].

The structural evolution of the loss of NH_3 and –NH stretches from the $Pt(NH_3)_4$/zeolite-Y precatalyst, during the temperature ramp under H_2, was qualitatively followed over time via IR spectroscopy. Dalla Betta and Boudart proposed that the "unstable neutral, hence mobile, hydride", $Pt(NH_3)_2H_2$ (Scheme 3), led to the formation of large 13–14 nm $Pt(0)_n$ nanoparticles supported on zeolite-Y when the precatalyst was reduced under H_2 without the calcination treatment [29]. However, no evidence was obtained for the presence of the putative $Pt(NH_3)_2H_2$ intermediate, nor was any kinetic or other evidence given for how $Pt(NH_3)_2H_2$ evolves to form the supported-nanoparticle product, $Pt(0)_n$/zeolite-Y.

In a subsequent study, Mashchenko et al. [144] did obtain IR spectroscopy stretching frequencies consistent with a $Pt–H^+$/zeolite-Y intermediate under H_2; such a species may be related to the putative $Pt(NH_3)_2H_2$ intermediate proposed by Dalla Betta and Boudart [29]. However, kinetic competence for the $Pt–H^+$/zeolite-Y intermediate en route to $Pt(0)_n$/zeolite-Y has yet to be demonstrated (i.e., observable species are often more stable and, therefore, detectable only because they can lie off the kinetically dominant pathway). While it is conceivable that the putative $Pt(NH_3)_2H_2$ intermediate may be responsible for the formation of the lower dispersed ~14 nm $Pt(0)_n$/zeolite-Y products under H_2, one precedented, alternative hypothesis [106] is that the varying precatalyst preparation steps have led to the formation of different supported-Pt precatalyst species (i.e., the different conditions of direct reduction under H_2 vs. calcination followed by reduction under H_2). Indeed, precedence exists in the extant, $M(NH_3)_4^{2+}$/support preparation literature [106,145–151] for the formation of: (i) $(PtO_2)_n$ particles, (ii) Pt^{2+}-based ions (ligand composition unknown), or (iii) $Pt(0)_n$ particles (formed via autoreduction[2]). Each of these species would then have their own, different rates and mechanisms of supported-nanoparticle heterogeneous catalyst formation [47]. Relevant, excellent accounts of the insights into the effects of the precatalyst/support contact and calcination steps can be found in several key papers [147,151], reviews [152–154] and a book chapter [155]. Clearly, then, this is a classic example of where direct in situ (or better *in operando*[4]) characterization of each precatalyst preparation step would be enormously helpful in elucidating the precatalyst speciation and then the resultant mechanism(s) of formation of the supported-nanoparticle catalyst(s). The bottom line here is that additional kinetic and other characterization studies are needed, under Dalla Betta and Boudart's precise experimental conditions, to confirm or refute the important $Pt(NH_3)_2H_2$ intermediate hypothesis.

In 1988, Sachtler and co-workers also studied the formation of $Pt(0)_n$/zeolite-Y under H_2 from the same $Pt(NH_3)_4^{2+}$/zeolite-Y precursor (Entry 2, Table 1) [39]. Again the $Pt(0)_n$ dispersion/particle

[8] Chemical-reaction-based mechanisms have been the hallmark of rigorous mechanistic chemistry in, for example, physical organic [24], organometallic chemistry [25,26] and inorganic chemistry [27,28]. That said, we have noted elsewhere [282] that "At times, a word or picture-only mechanism may be useful to describe what would otherwise be a very complex set of equations (that may not be tested or even testable due to their associated mathematical complexity). But, they (word- or picture-only mechanisms) do not lead to precise kinetic equations and corresponding differential equations (and then, ideally, their integrated counterparts), such differential-kinetic equations being required to test the mechanism vs. the experimental kinetic data. Another serious issue arises when a word or picture-only mechanism is proposed along with (different or other) equation(s) that cannot be derived from that (word or picture) mechanism: *a disconnect then results between the mechanism proposed and the differential equation(s) given*, which in turn *leads to the use of rigorously undefined, if not simply wrong, concepts and words for the physical phenomena at hand*. In rigorous mechanistic studies, balanced chemical equations define *both the rate constant* and the *words and concepts* that one can use" [282]. The latter point is particularly significant as discussed further elsewhere [281].

[9] Dalla Betta and Boudart reported the dispersion of the $Pt(0)_n$/zeolite-Y catalyst based on H_2 chemisorption measurements [29]. Herein we estimate the supported-nanoparticle diameter empirically using a formula from the literature: diameter = 108/(% dispersion) [3]. This formula can be derived by considering that the dispersion is equal to the number of surface metal atoms divided by the total number of atoms present with the particle, assuming a particle geometry (e.g., spherical), and taking into consideration the planar area of the metal atom of interest, all as derived in [3]. For example, the dispersion of the $Pt(0)_n$/zeolite-Y catalyst reduced directly under H_2 was experimentally measured to be 8%. Therefore, 108/8 = 13.5 nm or approximately 14 nm $Pt(0)_n$ nanoparticles supported on zeolite-Y.

size was found to be dependent on the calcination temperature. More specifically, lower calcination temperatures (e.g., 360 °C) lead to subnanometer $Pt(0)_n$ nanoparticles while higher calcination (e.g., 550 °C) temperatures led to much larger, 10–50 nm $Pt(0)_n$ nanoparticles supported on zeolite-Y. Because of the widely varying supported-nanoparticle products, two different supported-nanoparticle formation mechanisms were proposed (as described in Table 2, Entry 39), namely particle growth via migration and coalescence (for the subnanometer $Pt(0)_n$ nanoparticles) and nucleation and growth (for the 10–50 nm $Pt(0)_n$ nanoparticles). Unfortunately, these word-based mechanisms were not accompanied by the chemical equations necessary to define the underlying elementary reaction steps. The authors did obtain ex situ growth kinetics for the sample calcined at 360 °C by monitoring the Pt dispersion (i.e., the Pt/H ratio) via H_2 chemisorption. Also unfortunate is that the H_2 chemisorption data were not fit to any series of specific reactions and their associated kinetic equations to support, or refute, the author's proposed mechanistic hypothesis.

In a subsequent study (Entry 3, Table 2), Sachtler and co-workers examined the closely related system, $Pd(NH_3)_4^{2+}$/zeolite-Y, which was calcined at either 250 or 500 °C and then reduced under H_2 during a temperature ramp [41]. Both "Ostwald ripening and coalescence growth" mechanisms were proposed, albeit again without supporting kinetic data. In addition, neither study addressed the kinetics of the crucial nucleation step postulated [39] in the formation of their $Pd(0)_n$/zeolite-Y products. In short, specific, chemical-based mechanisms supported by kinetic studies are not available from these early, important studies of the M = Pt, Pd $M(NH_3)_4^{2+}$ precursor to $M(0)_n$/zeolite systems [39,41].

More recently, in 2002 Koningsberger and co-workers studied the temperature-ramped H_2 reduction of $[Pt(NH_3)_4](NO_3)_2/SiO_2$ to yield 1.8 nm $Pt(0)_n$ nanoparticles supported on SiO_2 [47] (Entry 4, Table 2). Several $[Pt(NH_3)_4](NO_3)_2/SiO_2$ precatalyst decomposition pathways were elucidated via temperature-programmed mass spectrometry; however and unfortunately, the stoichiometry of the supported-nanoparticle formation reaction was not rigorously demonstrated. Insights into the $Pt(0)_n/SiO_2$ supported-nanoparticle formation reaction were obtained from non-isothermal reduction kinetics monitored via EXAFS of both the Pt–N bond loss and the Pt–Pt bond formation. The resultant kinetic data provide direct evidence for a simultaneous, rapid decrease in the Pt–N coordination number along with a concomitant increase in the Pt–Pt coordination number between 150 and 200 °C. Building off Dalla Betta and Boudart's work [29], Koningsberger and co-workers postulated that a $Pt(NH_3)_2H_2$ intermediate was responsible for the formation of $Pt(0)_n/SiO_2$. However, again direct evidence for the postulated $Pt(NH_3)_2H_2$ hydride intermediate is lacking. In addition, XANES was used to follow the decreasing Pt L_{III} edge intensity as the supported-nanoparticle catalyst was being formed. The authors proposed that the final $Pt(0)_n/SiO_2$ particle size is "governed by the ratio of the growth-rate and nucleation rate". However, no mechanism was proposed for this specific $[Pt(NH_3)_4](NO_3)_2/SiO_2$ to $Pt(0)_n/SiO_2$ supported-nanoparticle heterogeneous catalyst formation reaction.

The authors are nonetheless correct in their statement that the nanoparticle size depends on the nucleation (k_1) and (autocatalytic) growth (k_2) rate constants. Significantly, a quantitative expression for nanoparticle size as a function of the k_1 (nucleation), k_2 (growth) and initial precatalyst concentration (call it $[A]_0$) is available from studies of the formation of nanoparticles in solution [[156]; see also [157]]. The k_1 and k_2 rate constants refer to the 2-step A → B slow, continuous nucleation (rate constant k_1) and then A + B → 2B autocatalytic surface growth (rate constant k_2) mechanism established for nanoparticle formation in solution, vide infra, where, again, A is the precatalyst and B is the growing, $M(0)_n$ nanoparticle surface [156,157]. Greater use of the nanoparticle size equation, as a function of k_1, k_2 and $[A]_0$ and when the 2-step nucleation and autocatalytic growth mechanism is operative [156], is recommended.

Between 2004 and 2009 Okumura and co-workers have extensively studied the formation under H_2 of $Pd(0)_n$ nanoparticles supported on a variety of zeolites, including the Na–ZSM-5, H–ZSM-5, H–mordenite and H–USY zeolites [50,58,62,63]. In an important initial study (Entry 5, Table 2), Okumura and co-workers used XAFS to follow the calcination (heating from 523 K to 773 K in O_2) of $Pd(NH_3)_4^{2+}$ supported on the zeolites Na–ZSM-5, H–ZSM-5 and H–mordenite [50]. A key finding is that the calcination step yields $(PdO)_n$ clusters supported on Na–ZSM-5, but highly dispersed Pd^{2+}–$O_{zeolite}$ ions on the H–ZSM-5 and H–mordenite zeolites as revealed, respectively, by the presence or lack of Pd–O–Pd contributions in the EXAFS spectra. While not rigorously investigated or discussed by the authors [50], the change in the Pd–Pd coordination number over time (and with increasing temperature) was, as expected, observed to be qualitatively quite different for each zeolite and for the reduction of $(PdO)_n$ and Pd^{2+}–$O_{zeolite}$ [50]—that is, one expects that the mechanisms of formation of supported $Pd(0)_n$ will be quite different for the $(PdO)_n$ clusters vs. the more highly dispersed Pd^{2+}–$O_{zeolite}$ ions. The observed, different Pd–Pd coordination number changes are consistent with the hypothesis, presented herein, that different supported-precatalysts $(PdO)_n$ and Pd^{2+}–$O_{zeolite}$ in the present case—and plausibly $(PtO_2)_n$, Pt^{2+} and $Pt(0)_n$ supported-precatalysts in the work of Dalla Betta and Boudart discussed earlier [29])—are expected to have different intimate mechanisms for their supported-nanoparticle formation reactions. Hence, further kinetic and mechanistic studies of this "$Pd(NH_3)_4^{2+}$"/support system (and of the classic aforementioned "$Pt(NH_3)_4^{2+}$"/support system [29] as well) are needed to determine the precise mechanisms of the supported-nanoparticle formation reactions for these different, $Pd(0)_n$ (and $Pt(0)_n$) systems.

Building off their aforementioned studies [50], Okumura and co-workers studied the formation of $Pd(0)_n$/H–USY [58] (Entry 6, Table 2). Characterization of the 773 K calcined $Pd(NH_3)_4^{2+}$/H–USY precatalyst via EXAFS spectroscopy indicated the formation of highly dispersed Pd^{2+}–$O_{zeolite}$ ions supported on H–USY. When the highly dispersed Pd^{2+}–O/H–USY ions were reduced with H_2 under an initial temperature programmed reduction (300–773 K under H_2), the supported-nanoparticle catalyst was found to be $Pd(0)_{\sim 55}$/H–USY. The metal component of the reaction stoichiometry was confirmed via XANES spectroscopy in that all of the Pd^{2+} was converted to Pd(0) under H_2 by the time 500 K was reached. Interestingly, subsequent calcination/reduction treatments led to the formation of smaller, more highly dispersed, $Pd(0)_{\sim 4}$ and $Pd(0)_{\sim 13}$ clusters supported on the H–USY zeolite. In each case, EXAFS was used to follow the kinetics of the loss of Pd–O and the formation of Pd–Pd. Unfortunately and despite these very valuable direct kinetic studies from Okumura and co-workers, no detailed mechanism was proposed for the formation of the $Pd(0)_n$/H–USY supported-nanoparticle catalyst.

More recently, Okumura and co-workers revealed conditions where they could study the formation of $Pd(0)_{\sim 13}$/H–USY from $Pd(NH_3)_4^{2+}$ supported on H–USY [62,63] (Entries 7 and 8, Table 2). Two notable differences from the aforementioned studies [50,58], differences which give rise to varying supported-precatalysts, are that the $Pd(NH_3)_4^{2+}$/H–USY precatalyst sample was dried under the milder conditions of 323 K in air (vs. 773 K under O_2), and that the reduction under H_2 to $Pd(0)_{\sim 13}$/H–USY was carried out isothermally at 300 K (vs. 300–773 K under H_2). EXAFS analysis of the supported-precatalyst species suggests some form(s) of $Pd(NH_3)_{4-x}(H_2O)_x$/H–USY are present; however, it is difficult to distinguish between the Pd–N and Pd–O contributions in the EXAFS spectrum and, therefore, problematic to assign definitively the x value of the composition based on only the EXAFS. Clearly, however, the precatalyst is different from either the $(PdO)_n$

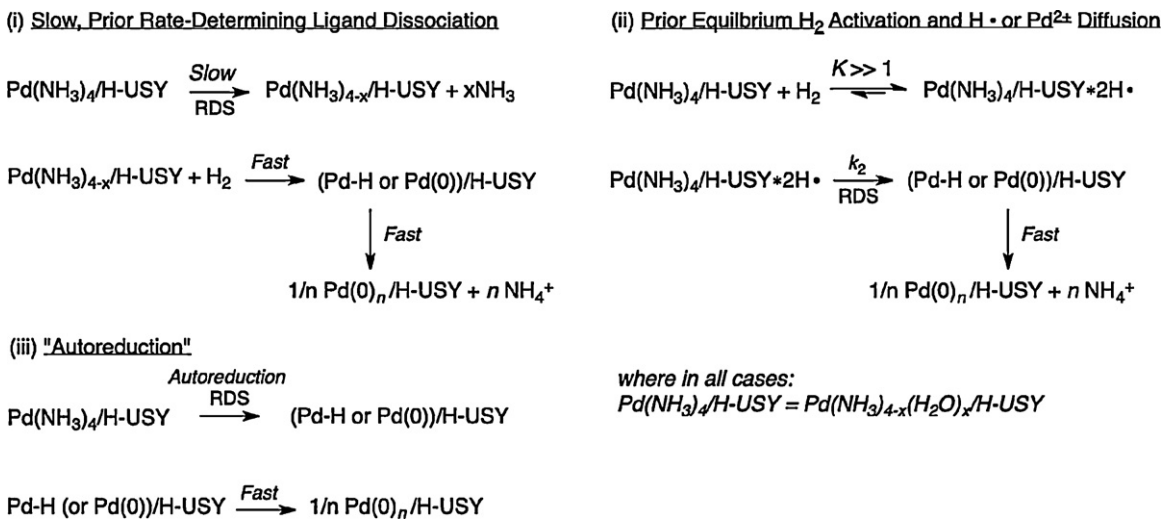

Scheme 4. Three plausible, deliberately minimal mechanisms proposed herein to account for the observed $Pd(0)_{\sim 13}$/H–USY supported-nanoparticle formation kinetics obtained by Okumura and co-workers [62,63]. The proposed mechanisms include: (i) a slow, prior rate-determining step such as ligand dissociation; (ii) a mechanism where H_2 is activated on the zeolite with $K \gg 1$ and then diffusion occurs as part of the rate-determining step; and (iii) an "autoreduction"[2] mechanism. In the autoreduction possibility (iii), the (non-obvious), ostensibly NH_3-based decomposition products are not shown.

clusters or the highly dispersed Pd^{2+}–$O_{zeolite}$ ions previously observed by EXAFS [50,58]. The metal component of the reaction stoichiometry was again confirmed by XANES spectroscopy, data which indicate complete reduction of $Pd(NH_3)_4^{2+}$ to $Pd(0)_{\sim 13}$ within 20 min. The authors studied the kinetics of the loss of Pd^{2+}/H–USY (via the XANES region) and the concomitant formation of $Pd(0)_n$/H–USY (via the EXAFS region). Plots of $\ln(C_0/C)$ (where $C_0 = Pd(0) + Pd^{2+}$ and $C = Pd^{2+}$) for both processes were linear, consistent with first-order behavior (i.e., $-d[Pd^{2+}]/dt = [Pd^{2+}]^1$ and $+d[Pd–Pd]/dt = [Pd–Pd]^1$), yielding apparent rate constants of $k = 0.28\ min^{-1}$ and $k = 0.35\ min^{-1}$, respectively.[10] Okumura and co-workers also investigated the effects of the H_2 partial pressure (from 0.6 to 50% by volume of H_2 in He), on the $Pd(0)_{\sim 13}$/H–USY supported-nanoparticle formation reaction [63]. A plot of the $\ln k$ vs. $\ln P(H_2)$ plot was almost linear, with only a slight slope of 0.08, indicating that the "partial pressure of H_2 hardly affected the reduction rate of Pd^{2+}", that is, implying a near-zero order dependence on hydrogen $[H_2]^{0.08}$. Overall, Okumura and co-workers studies contain the only quantitative kinetic data to date for the $Pd(NH_3)_4^{2+}$/support to $Pd(0)_n$/support system (and for the $Pt(NH_3)_4^{2+}$/support to $Pt(0)_n$/support system). However, they did not propose a mechanism for how the $Pd(0)_{\sim 13}$/H–USY supported-nanoparticles form, so that is done next.

Three conceivable mechanisms for the $Pd(0)_{\sim 13}$/H–USY supported-nanoparticle formation system are given in Scheme 4, possible mechanisms which we emphasize are deliberately minimal and offered solely to stimulate the required additional investigations attempting to disprove them.[11] The observation of a first-order dependence on both the loss of the precursor and formation of the $Pd(0)_{\sim 13}$/H–USY supported-nanoparticle catalyst, $-d[Pd^{2+}]/dt = [Pd^{2+}]^1$ and $+d[Pd(0)_{\sim 13}]/dt = [Pd–Pd]^1$, requires one to write mechanisms with only one Pd in the rate-determining-step. The mechanistic postulates in Scheme 4 are: (i) a slow, rate-determining step (top left, Scheme 4), such as ligand dissociation, to some "intermediate" species, followed by the fast activation of H_2 and subsequent formation of $Pd(0)_{\sim 13}$/H–USY; (ii) H_2 activation by a $K \gg 1$ prior equilibrium, on for example the zeolite surface, followed by slow diffusion of two H• to the Pd^{2+} species and or diffusion of Pd^{2+} to the activated H• as part of the rate-determining step, followed by fast agglomeration of the resultant Pd–H or Pd(0) species (top right, Scheme 4); or (iii) some autoreduction[2] process (bottom left, Scheme 4) that generates reducing equivalents, an autoreduction that the observed kinetics require would have to be slow and rate-determining (i.e., and relative to the subsequent, faster, supported-nanoparticle formation steps under H_2). The autoreduction mechanism can likely be ruled out given the lower temperature (300 K) reaction conditions since the reducing equivalents, generated from autoreduction of supported $M(NH_3)_4^{2+}$ complexes, are not typically observed until somewhat higher, 373–473 K, temperatures [149]. Overall, then, the implications are that the rate-controlling ligand dissociation or H• (or $Pd(NH_3)_4^{2+}$) migration steps are obscuring the supported-nanoparticle heterogeneous catalyst formation kinetics. To summarize, additional kinetic studies are needed in order to obtain the full rate law and distinguish between the prior equilibrium and H_2 activation mechanisms shown in Scheme 4 for this otherwise classic $Pd(NH_3)_4^{2+}$/support system [62,63].

2.2.2.2. System II: H_2PtCl_6/support based systems. $Pt(0)_n$ nanoparticles supported on γ-Al_2O_3, as well as bimetallic derivatives such as $(Pt–Re)_n$, are often used in catalytic reforming reactions [3,36,40,158–161]. One of the most common metal precursors for the preparation of $Pt(0)_n$/γ-Al_2O_3 is H_2PtCl_6. However, and again, little is known about the kinetics and mechanisms of the supported-nanoparticle heterogeneous catalyst formation step for such Pt-based systems. Five studies, which are summarized in Entries 9–13 of Table 2, start from a H_2PtCl_6-based supported metal precatalyst.

In 1986 and 1988 Dexpert and co-workers [38,40] studied the formation of ∼1 nm $Pt(0)_n$ nanoparticles supported on γ-Al_2O_3, at 200 °C under H_2, from an ill-defined $Pt(OH)_x(Cl)_y$/γ-Al_2O_3 precursor. In their first study [38], the first 10 min of the supported-nanoparticle formation were qualitatively followed via EXAFS and

[10] The reported rate constants from the EXAFS analysis (e.g., $k_{obsPd–Pd} = 0.35\ min^{-1}$) were not corrected by the required statistical factor for the reaction stoichiometry of $2Pd^{2+} \rightarrow 1Pd–Pd$; that is the XANES monitors the loss of $1Pd^{2+}$ ($-d[Pd^{2+}]/dt/1$) species while the EXAFS monitors the formation of Pd–Pd ($+d[Pd–Pd]/dt/2$). Hence, $2k_{obsPd–Pd}$ is equivalent to $1k_{obsPd2+}$ so that $k_{obsPd–Pd}/2 = 0.35/2 = 0.18\ min^{-1}$.

[11] (a) Reaction mechanisms, like science in general, progress only via conclusive disproof of multiple alternative hypotheses, as Platt has emphasized (J.R. Platt, Science 146 (1964) 347–353). Platt has further noted that "for exploring the unknown, there is no faster method". We strongly recommend Platt's classic paper to all scientists. It is one of our favorite papers in all of science!

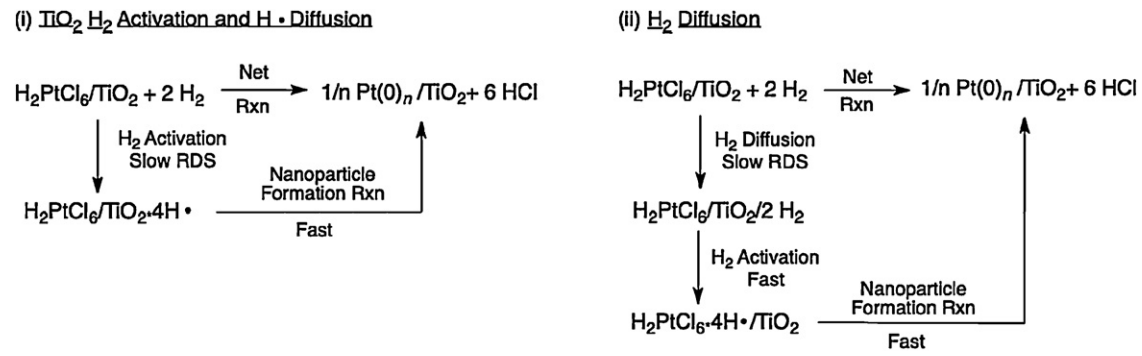

Scheme 5. Shown left is a proposed stoichiometry (top) and accompanying mechanism (bottom) [72] containing a slow rate-determining H_2 activation step to account for the observed, linear, apparently zero-order Pt–Cl and Pt–Pt kinetics observed for the formation of $Pt(0)_n/TiO_2$ [56]. Shown right is an alternative mechanism containing a slow H_2 diffusion step that could also account for the observed kinetics [56].

XANES. A word-based mechanism, summarized in Entry 9 of Table 2, was proposed for the formation of small Pt_xCl_y clusters. However, the kinetic data collected were not fit to the proposed mechanism to thereby support, or refute, that proposed mechanism. In a subsequent report [40], the loss of Pt–O and Pt–Cl bonds in the supported precursor complex, as well as the formation of Pt–Pt bonds, were followed by EXAFS at 180 °C. No additional mechanistic details were proposed for the formation of the $Pt(0)_n/\gamma\text{-}Al_2O_3$ supported-nanoparticle catalyst [40].

In 2007 Chupas et al. used the direct and powerful method of total high-energy X-ray scattering along with PDF analysis to study the kinetics of $Pt(0)_n/TiO_2$ supported-nanoparticle formation [56,66] (Entry 11, Table 2). While the stoichiometry of the supported-nanoparticle formation reaction was not rigorously demonstrated, the $Pt(0)_n/TiO_2$ products were found to be 1–5 nm depending on the reduction temperature. In their initial study, in situ X-ray scattering was used to directly follow both the loss of Pt–Cl bonds and the formation of Pt–Pt bonds at 100, 150 and 200 °C. The kinetic data of the loss of the Pt–Cl bonds were well fit to a zero-order process, which was dependent on the reduction temperature—the activation energy of the zero-order reaction was found to be 50.17 kJ/mol, apparently the activation energy of a diffusion controlled process (vide infra). Unfortunately, no mechanism was proposed for the supported-nanoparticle formation reaction; the observed zero-order kinetics (i.e. $-d[H_2PtCl_6/TiO_2] \propto [H_2PtCl_6]^0$) imply a diffusion controlled process to the observed $Pt(0)_n/TiO_2$ products as detailed next.

The intriguing linear loss of H_2PtCl_6/TiO_2 and implied zero-order dependence $[H_2PtCl_6]^0$, sparked others to postulate a mechanism that could describe such a dependence for the $Pt(0)_n/TiO_2$ system and since those other authors were also studying this same system, albeit in contact with solution [72]. Following collaborative discussions with the Chupas group, a mechanism was postulated that is consistent with the observed kinetic data, as shown in Scheme 5. The proposed mechanism consists of rate determining H_2 activation on TiO_2, followed by fast $H^\bullet$ diffusional transfer to the active site (not shown, where H_2PtCl_6 is reduced) and then supported-nanoparticle formation (i.e., which must be fast compared to the rate-determining H_2 activation/diffusion and in order to explain the observed, zero-order kinetics). It is also plausible that a second, also diffusion-limited mechanism is operating here, one where the diffusion of non-dissociated H_2 to the Pt^{4+} precatalyst is slow and the subsequent H_2 activation and supported-nanoparticle formation steps are fast. Consistent in a general way with the presence of a diffusion-limited process, a report has appeared [56] describing $Pt(0)_n/TiO_2$ supported-nanoparticle formation *in contact with solution* (i.e., involving a gas–liquid–solid system) where a H_2 gas-to-solution, diffusion-limited mechanism was also found to be operating under certain conditions (vide infra, Section 3.2.2.3).

In a follow up study, Chupas et al. [66] studied the change in the Pt–Pt contributions as the temperature was ramped from 0 to 227 °C (Table 2, Entry 11). Three distinct regimes were observed, from which the authors proposed that the "...initial particles that form are small (<1 nm) then agglomerate into ensembles of many small particles and lastly anneal to form larger well-ordered particles". These ground breaking, first-of-their-kind, total high-energy X-ray scattering/PDF analysis methods from the Chupas team promise to provide significant insights into the mechanisms of supported-nanoparticle heterogeneous catalyst formation once the best, well-defined systems are studied. It will be important in those studies to couple the X-ray scattering/PDF method to experimentally determined, balanced reaction stoichiometries and to other complimentary kinetic monitoring methods.

In 2009, Shishido et al. investigated the formation of $Pt(0)_n$ nanoparticles supported on TiO_2 and $\gamma\text{-}Al_2O_3$ from a $PtO_x/TiO_2(\gamma\text{-}Al_2O_3)$ precatalyst (Table 2, Entry 12). The observation of PtO_x by EXAFS is indicative of either highly dispersed atomic Pt^{4+} ions or the presence of supported-PtO_2 monomers. Evidence against the formation of aggregated $(PtO_2)_n$ particles, post the precatalyst calcination step, is given by a lack of long range Pt–O–Pt contributions in the EXAFS analysis (a control EXAFS measurement showed that such long range Pt–O–Pt contributions were observable in a bulk PtO_2 standard). To start, the authors monitored the change in the Pt L_{III} white line[12] XANES edge over time for the PtO_x/TiO_2 sample by admitting a pulse of 200 μL of H_2 into their gas–solid cell. At 473 K the reduction of Pt^{4+} to Pt(0) was linear and complete within 1 s (i.e., further pulses of H_2 did not change the XANES white-line intensity, meaning that no additional PtO_x was being reduced to Pt(0)) with no observable induction period. These observations are consistent with Chupas et al.'s observation of linear kinetics for the formation of $Pt(0)_n/TiO_2$ at 200 °C (which had not been calcined, i.e., the Chupas team started from the chloro complex $PtCl_6^{2-}$ supported on TiO_2) [56]. In addition, isosbestic points were observed in the XANES data at 473 K, suggesting that a direct transition from Pt^{4+} to Pt(0) occurred with no observable intermediate(s). Unfortunately, Shishido et al. did not attempt to fit their data to zero- or first-order plots. Another important point is that the temperature of the reduction drastically affected the observed changes in the

[12] (a) The white-line at the L_3-edge is an element-specific quantum mechanical transition arising from the excitation of core-level $2p_{3/2}$ electrons into unoccupied $5d_{5/2}$ and $5d_{3/2}$ states above the Fermi level.[12] Practically, the white-line intensity at the L_3-edge is a spectroscopic fingerprint that can be used, for example, to follow the loss of a supported metal precatalyst species. (b) J.J. Rehr, R.C. Albers, Rev. Mod. Phys. 72 (2000) 621–654.

white-line intensity over time; at room temperature the white line intensity effectively remained constant after two, 200 μL pulses of H_2, and did not fully decrease until the third pulse (after which no change was seen with subsequent pulses of H_2). Although not discussed by the authors, the lack of an observable change in the XANES white line intensity with exposure to H_2 implies that an induction period is present under the more mild, room temperature reduction conditions.

Next, the authors changed the support from TiO_2 to γ-Al_2O_3 and examined the reduction of PtO_x/γ-Al_2O_3 by monitoring the XANES Pt L_{III}-edge and using the same H_2-pulse procedure. Interestingly, the PtO_x/γ-Al_2O_3 precatalyst could not be reduced (i.e., the XANES white-line intensity did not change) with H_2 at room temperature over the course of 100 s, revealing that the reduction of the PtO_x/γ-Al_2O_3 is slower than that observed for the PtO_x/TiO_2 sample. The results provide prima facie evidence that the support plays a major role in the rates of supported-nanoparticle formation, at least in the PtO_x/TiO_2 and PtO_x/γ-Al_2O_3 systems. However, no mechanism was proposed for this interesting, supported-nanoparticle heterogeneous catalyst formation system. Additional kinetic and mechanistic investigations should prove informative and, therefore, are recommended.

Noteworthy here is that others observed very similar support effects for the reduction of H_2PtCl_6 on γ-Al_2O_3 and TiO_2, but now with these catalysts in contact with solution (i.e., in a gas–liquid–solid system) [72], vide infra, Section 3.2.2.3. That connection (i.e., of the H_2PtCl_6 on γ-Al_2O_3 or TiO_2 at the gas–solid interface vs. these same systems in contact with solution), and the connection between the Chupas [56] and the solution [72] studies of H_2PtCl_6/TiO_2 (specifically the diffusion limited kinetics seen for 5-wt% $Pt(0)_n/TiO_2$), are important connections/insights. Those comparisons suggest that the mechanistic insights obtained from such studies of supported heterogeneous catalyst formation in contact with solution [72,74,75] will at least sometimes connect back to, and perhaps be transferable to, the formation of supported-nanoparticle catalysts at the gas–solid interface (more here in Section 3.2.2.4, vide infra).

One final topic that merits discussion is the speciation of H_2PtCl_6 that can occur during the metal/support impregnation step. The speciation of H_2PtCl_6 in H_2O [162], and in contact with γ-Al_2O_3 [163–166], has been extensively studied, is quite complex, and varies according to the conditions employed during the impregnation step [162–166]. The literature is clear that the following species exist in aqueous solution as a starting reference point: $[PtCl_6]^{2-}$, aquo species such as $[PtCl_5(H_2O)]^-$, and aquahydroxo species such as $[PtCl_4(OH)(H_2O)]^-$; in addition, their relative concentrations are pH dependent as one might expect [162–166]. Hence, the exact interaction of the species formed from H_2PtCl_6 in aqueous solutions and in contact with γ-Al_2O_3 remains a complex, controversial subject [163,164]. Regalbuto has suggested that when fresh H_2PtCl_6 solutions are prepared, the major species present in solution is $[PtCl_3(H_2O)_3]^+$, and it is repelled from the protonated $[\gamma\text{-}Al_2O_3]^+$ surface at low pH [162]. In contrast, the major species present in aged H_2PtCl_6 solutions at a pH of 5–9 is $[PtCl_2(OH)_2(H_2O)_2]^0$ [162], a neutral species that should more readily interact with the γ-Al_2O_3 support. Solution speciation for other chloro precursors, such as $AuCl_3$ [52,59,167,168], has also been documented.

Interestingly, recent work with the discrete, soluble metal oxides known as polyoxometalates reveals that metal chlorides, such as $PtCl_4^{2-}$ [169,170] or $RuCl_3$ [171] (with their strong metal–ligand bond strengths), are often inferior to $Pt^{II}(OH)_6^{2-}$ [172,173], for example and in the platinum case, for inserting especially third- or even second-row transition metals into metal-vacancy containing, so-called "lacunary", polyoxometalates. The connection here is that insights from the syntheses involving discrete metal oxides such as polyoxometalates and late transition-metals can probably be used to guide improved syntheses of superior, solid-oxide-supported catalysts.

The bottom line, then, of this subsection on H_2PtCl_6 derived catalysts is that until and unless care is taken to minimize the speciation present, the resultant supported-metal precatalysts will both be ill-defined, likely exist as multiple species, and in turn yield multiple reactions and mechanisms to supported-nanoparticles with a broad size distribution, mixed shapes and disordered compositions! Hence, a—if not the—first topic en route to preparing the next generation of supported-nanoparticle $Pt(0)_n$ (and other) catalysts is the nature of the precise Pt speciation when H_2PtCl_6 (and other) metals are placed on supports such as γ-Al_2O_3. Once the expected extensive studies required to unravel that speciation are in hand, the next task will be to determine the kinetic contribution of each species to the supported $Pt(0)_n$ nanoparticle formation reaction.[13] Improved, rational heterogeneous catalyst syntheses will require such speciation knowledge, kinetic and mechanistic studies and, then, exploitation of the resultant insights.

2.2.2.3. System III: Ag^+/zeolite supported systems. Interest in $Ag(0)_n$ zeolite-supported (commonly zeolites A, X and Y) catalysts arises from their potential use for hydrocarbon oxidation and the dimerization of alkenes [174]. Much is known about the precatalyst preparation steps (i.e., the metal/support ion-exchange, drying and then calcination steps) when starting from $Ag(NO_3)$ and a zeolite. A key point, again, is that a broad range of speciation is present, including Ag^+, Ag_n^{x+} clusters and other established species [174–188]. However, much less is known about the supported-nanoparticle formation step. Entries 14–18 in Table 2 highlight the five papers [32,36,37,42,57] in the literature that address the kinetics and mechanisms of formation of $Ag(0)_n$/zeolite supported-nanoparticle heterogeneous catalysts.

In a classic 1976 paper, Jacobs and co-workers studied the formation of a putative, $Ag(Ag_3)^+$ subnanometer cluster on zeolite-Y from a Ag^+/zeolite-Y precatalyst over the temperature range of 298–623 K [32] (Table 2 (Entry 14)). Complete reduction of Ag^+ to Ag(0) was observed only above 556 K. The stoichiometry of the reduction reaction was proposed to occur via Eq. (3) (where the zeolite support has been omitted, although it likely plays a role in trapping the proton, vide infra); H_2 uptake measurements confirmed the Ag^+, H_2 and Ag(0) portions of that stoichiometry (Eq. (3)):

$$2Ag^+ + H_2 \rightarrow 2Ag(0) + 2H^+ \quad (3)$$

Eq. (3) is an example of what organometallic chemists have studied extensively and is known as heterolytic H_2 activation [25,26]. As such, it requires a base (B) to accept the protons (as $B\text{–}H^+$), the strength of the base typically having a large effect on the observed rate. In the present case the base is likely a zeolite–O^- site, which when protonated yields the hydroxyl species zeolite–OH (a site not experimentally verified for the $Ag(0)_n$ supported-nanoparticle formation systems in Entries 14–18 of Table 2). The $Ag(0)_n$/zeolite-Y supported-nanoparticle products were probed using powder X-ray diffraction; below 473 K the products are $Ag(0)_n$ particles <3.5 nm (as indicated by the lack of a Ag(1 1 1) reflection in the XRD spectrum). Above 423 K, the XRD data reveal that the $Ag(0)_n$ zeolite-Y supported-nanoparticles are 21 nm—a result that implies that the $Ag(0)_n$ particles are no longer within the pores of the zeolite.

The authors used H_2 uptake measurements to follow the kinetics of the Ag^+ reduction; two distinct, temperature-dependent kinetic regimes were observed. Since no mechanism was proposed for the

[13] Highly relevant here is the observation that the kinetics of $Pt(0)_n$/γ-Al_2O_3 formation, in contact with EtOH are variable and irreproducible [72], with uncontrolled speciation being the reported culprit, vide infra, Section 3.2.2.3.

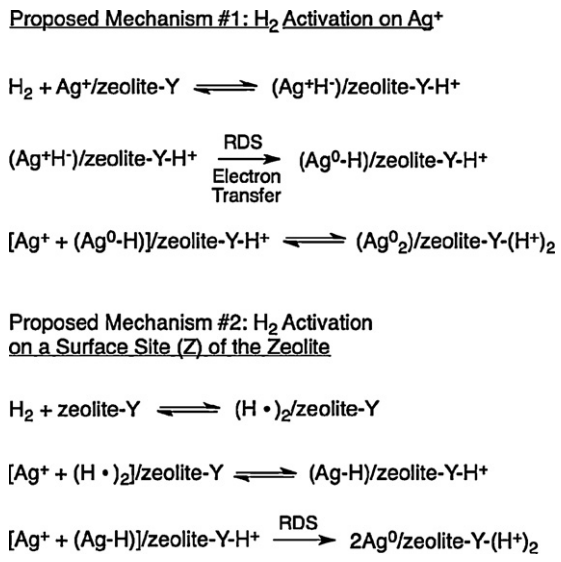

Scheme 6. The two mechanisms proposed by Jacobs and co-workers for the H_2 reduction of Ag^+/zeolite-Y to Ag^0/zeolite-Y [32] at ≤430 K. The first mechanism (top) entails H_2 activation on Ag^+ followed by a rate-determining electron transfer step, while the second mechanism involves H_2 activation on the zeolite and a rate-determining regeneration of the zeolite support site ("zeolite-Y", which has been added for clarity to the author's original mechanisms [32]). However, only the first mechanism appears to be consistent with the author's observed kinetic data as discussed in the main text.

high temperature regime (i.e., >430 K), in what follows the focus will be on the kinetic data obtained at lower temperatures (i.e., ≤430 K). The kinetics at ≤430 K were first-order with respect to Ag^+ and H_2, showed an inverse-first-order dependence with respect to the "reaction product concentration" [32] (i.e., $-d[H_2]/dt \propto [Ag^+]^1$, $[H_2]^1$ and $[H^+$ or $Ag(0)]^{-1}$, respectively).[14] An apparent activation energy of 40 kJ/mol was also obtained. The authors proposed two mechanisms (Scheme 6) both of which are claimed to be consistent with the observed kinetic data. However, only the first mechanism looks to be consistent with the observed rate law, vide infra.

In the author's first proposed mechanism (Scheme 6, top), H_2 is activated on Ag^+ followed by a slow rate-determining electron transfer step. In the second postulated mechanism (Scheme 6, bottom), H_2 is activated on some surface site of the zeolite (zeolite-Y), followed by the diffusion of Ag^+ to that activated H–zeolite-Y and finally rate-determining regeneration of that surface site. Jacobs and co-workers favor the second mechanism (bottom), and argue that electron transfer in the first mechanism (top) should not be rate determining. However, the differential equation describing their second mechanism was not provided and attempts, at least in our hands, to derive a differential equation consistent with the observed kinetic data have not been successful (i.e., for the rate law: $-d[H_2]/dt \propto [Ag^+]^1$, $[H_2]^1$ and $[H^+$ or $Ag(0)]^{-1}$). As inspection of the second mechanism predicts, such derivations yield a $[Ag^+]^2$ dependence, at least in our hands.

Derivations of the rate law corresponding to the first mechanism (Scheme 5, left) are consistent with the kinetic data, as stated by Jacobs' and co-workers [32]. Hence, the observed kinetic data favor the first mechanism, where by H_2 is heterolytically activated by Ag^+ plus a basic site on the zeolite.

[14] A key kinetic plot in Jacobs' and co-workers paper [32] is in their Fig. 5. That plot establishes both a $[H_2]^1$ and a "c^{-1}" (i.e., a $[H^+]^{-1}$ or $[Ag(0)]^{-1}$) dependence, all from just the H_2-uptake kinetics, plus the stoichiometry $C_0 - C_i' = [Ag^+]_i - [Ag^+]_t - [Ag(0)]_t - [H^+]_t$. As such, this is an illustrative example of how considerable kinetic information can be obtained from just H_2 uptake kinetic measurements plus a balanced reaction stoichiometry.

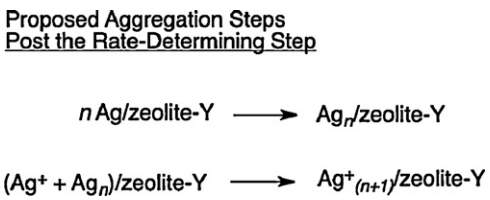

Scheme 7. The fast, post rate-determining (i.e., post the proposed steps in Schemes 5 and 6) aggregation steps proposed by Jacobs and co-workers, steps proposed to account for the observed formation of the aggregated $Ag(0)_n$/zeolite-Y products [32].

While the diffusion of Ag^+ on the zeolite surface is possible, well-known $H^\bullet$ diffusion (i.e., $H^\bullet$ spillover) could also be part of the Ag^+ plus $H^\bullet$ surface reaction [189]. In short, while the final detailed mechanism remains to be established, illustrative and worth noting here is the nearly complete rate law that Jacobs' and co-workers were able to obtain from just the reaction stoichiometry coupled with H_2-uptake kinetic data. Their results argue strongly for the increased use of H_2 uptake experiments to screen and establish the initial steps of supported-nanoparticle formation, at least when and where such H_2 uptake experiments are possible.

Finally, to account for the formation of their aggregated $Ag(0)_n$/zeolite-Y products, Jacobs and co-workers proposed the post-rate-determining, aggregation steps shown in Scheme 7 (albeit of course without any kinetic evidence for those steps since they are hidden kinetically by being after, and thus faster than, the rate-determining steps in Scheme 6) [32]. Based on two aggregation steps now precedented in solution nanoparticle chemistry [190–192], one can propose that analogous B + B → C (bimolecular) and B + C → 1.5 C (autocatalytic) aggregation steps are actually a part of the aggregation/agglomeration of $Ag(0)_n$ in the Ag^+/zeolite-Y system, where B is $Ag(0)_n$, and C is aggregates of B. The broader, more general point here is that there is a need to mesh the literature of formation of $Ag(0)_n$/solid-supports (Table 2, Entries 14–18) with the established mechanistic steps of nanoparticles in solution [190–194] where applicable. A second, important future goal is to integrate the above two areas with the extensive literature of ligand-stabilized $Ag(0)_n$–L_x nanoparticle formation in solution [195–198].

In 1980 Hermerschmidt et al. [36] studied the formation of <5 nm $Ag(0)_n$/zeolite-A supported-nanoparticles under H_2 by ESR spectroscopy (albeit from an uncharacterized, Ag supported-precatalyst) (Entry 15, Table 2). A intermediate Ag_6^+/zeolite-A supported-cluster detectable by ESR was shown to be kinetically competent for the formation of <5 nm $Ag(0)_n$ nanoparticles supported on zeolite-A. Although kinetic data were collected, Hermerschmidt et al. acknowledge that "...the rate of formation of the silver clusters can be (and were) measured from ESR signal intensities below room temperature; however, no evaluation of kinetic data was attempted since a simple kinetic model cannot be proposed for the complex mechanisms involved in the reduction, migration, and aggregation processes". This 1980 statement is notable, a general testament to the difficulty in studying the kinetics and deriving a consistent and plausible elementary-step-based mechanism for such supported-nanoparticle heterogeneous catalyst formation reactions. Nevertheless, and as pointed out by Jacobs [153], "Hermerschmidt et al. established that the loss of Ag_6^+/zeolite-A and the formation of $Ag(0)_n$/zeolite-A occur concurrently" [36].

Following up their earlier work [32], in 1982 Jacobs and co-workers studied the reduction of Ag^+ supported on the chabsite zeolite (Entry 16, Table 2) to yield a sub-nanometer $(Ag_2^+)_m$/chabsite product (where m is assumed/proposed by the authors, albeit without any experimental evidence, to be 2 to yield

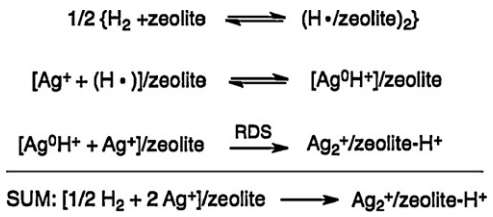

Scheme 8. The mechanism proposed by Jacobs and co-workers [37] for the formation of Ag_2^+ on the chabsite zeolite. Modifications added herein for clarity include: the addition of the zeolite support ("zeolite", above), the 1/2 { } to balance the reaction, and the final summed stoichiometry.

an overall Ag_4^{2+} cluster) [37]. Again, a significant amount of kinetic information was extracted via H_2 uptake measurements, data revealing that the reaction is second-order in Ag^+ and half-order with respect to the H_2 pressure (i.e., $-d[Ag^+]/dt = k[Ag^+]^2[H_2]^{1/2}$). An apparent activation energy of 49 kJ/mol was also reported. The authors proposed the mechanism shown in Scheme 8, where the "zeolite" has again been added clarity. The mechanism for their stated "first reduction step" now requires homolytic H_2 activation (which presumably occurs on the zeolite surface or an impurity such as Fe^{n+} on the zeolite), followed by the formation of a putative protonated Ag(0), "Ag^0H^+", species (that an organometallic chemist would write formally as a little precedented, high energy Ag^{II} species $[Ag^{II}–H]^+$). Then a rate-determining step of Ag^+ ion migration to that "Ag^0H^+" was proposed. Unfortunately, the differential equation corresponding to the mechanism shown in Scheme 8 was again not derived [37]—but derivations done as part of this review confirm that the proposed mechanism will indeed account for the $-d[Ag^+]/dt = k[Ag^+]^2[H_2]^{1/2}$ rate law. That said, still needed to support the proposed mechanism in this classic study include: (i) unequivocal demonstration of the net reaction stoichiometry, plus (ii) further kinetic and mechanistic work. Further study is also needed to (iii) understand why the mechanism and rate law have changed from that in Scheme 6 [32]; understanding the origin of that change promises to yield an at least interesting, if not important, insight into supported $(Ag_2^+)_m$/chabsite zeolite heterogeneous catalyst formation.

Moving to a 1989 study, Schoonheydt et al. also studied the kinetics of the formation of Ag_6^+/zeolite-A, from a putative Ag^+/zeolite-A precatalyst, under H_2 and over the temperature range of 258–298 K [42] (Table 2, Entry 17). ESR was used to follow the formation of Ag_6^+ on zeolite-A (via the most intense, central line of the ESR spectra). The resultant kinetic data were not fit to any mechanism, but appear first-order in most instances. At each temperature, the initial rate (i.e., $[+d[Ag_6^+/\text{zeolite-A}]/dt]_i$) was extracted, and the log of the initial rate was plotted vs. $1/T$ to obtain an apparent activation energy of 47–60 kJ/mol (which depended strongly on the amount of ion-exchanged Ag^+).

Schoonheydt et al. also investigated the role of the zeolite counter cation on the formation of Ag_6^+/zeolite-A by ESR (e.g., K^+ was exchanged for Na^+). The idea here is that if the diffusion of Ag^+ is a crucial step in the Ag_6^+/zeolite-A formation reaction, then the presence of different cations should affect the resultant kinetics. The kinetic curves are clearly different in the presence of K^+ cations (vs. Na^+), appearing sigmoidal when K^+ is present (vs. linear kinetics for the Na^+ sample). Hence, the presence of other cations besides Ag^+ matters. Finally, the authors note that Fe-based impurities (either discrete Fe^{3+} or Fe_2O_3) also affected the kinetics of Ag_6^+/zeolite-A formation. From this information the authors hypothesize that "the rate-determining step for the formation of the Na^+-exchanged Ag_6^+/zeolite-A is the diffusion of Ag^+ cations" [42]—again we see that slow, M^{x+} cation diffusion on supports and/or $H^\bullet$ diffusion is a common, albeit still not well-understood, step in the proposed mechanism of formation of supported-nanoparticle catalysts.

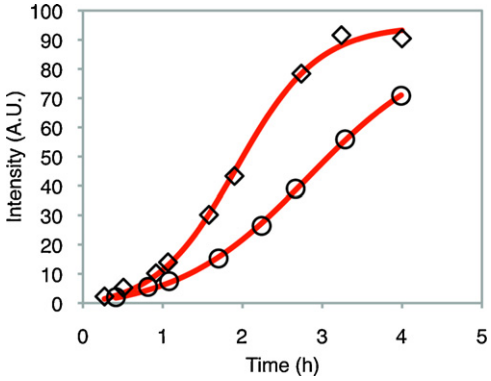

Fig. 7. The kinetics of Ag_6^+/zeolite-A(K^+) supported-(sub)nanoparticle formation measured by ESR at 273 K (circles) and 278 K (diamonds) [42]. The red lines are fits done as part of this review to the 2-step mechanism of A → B and A + B → 2B [193], where A is Ag^+, and B is the higher molecularity Ag_n or $Ag_{(n+1)}^+$ product(s). (For interpretation of the references to color in this figure legend, the reader is referred to the web version of the article.)

Adapted with permission from [42]. Copyright (1989) American Chemical Society.

The mechanism of the Ag_6^+ cluster formation consists, then, of at least two steps according to the authors: (i) "the formation of reduced centers, and (ii) the migration of Ag^+ towards these (reduced) centers" [42] (or, again we would add, $H^\bullet$ migration). The authors note that "the reduced centers cannot be the Ag(0) atoms" [42]. In addition, the authors also suggest, "that the cluster formation is a series of consecutive reactions" given by $Ag + Ag \rightarrow Ag_2 \rightarrow Ag_3$ and so on to the Ag_6^+ product. The authors argue that diffusion of Ag^+, rather than of Ag(0), is rate-limiting based on the fact that the measured activation energy (40–67 kJ/mol) is within the range of known monovalent cation diffusion E_a values in zeolite-A [42]. However, additional studies are needed to rule out a mechanism containing diffusion of Ag(0) (or possibly of Ag–H) as well as the possibility of $H^\bullet$ migration. In addition, the activation energy measured for the putative Ag^+ migration step is at best a composite of the undetermined mechanism of Ag_6^+/zeolite-A formation, making both interpretation of the 40–67 kJ/mol values, and its comparison to literature values, problematic at present [199,200].[15]

Finally, in Fig. 7 we show previously unpublished results revealing that the K^+-based Ag_6^+/zeolite-A (zeolite-A(K^+)) kinetics can be fit to a simplified, 2-step nanoparticle formation mechanism[16] that will be detailed in Section 3.[17] The 2-step mechanism has the general form of A → B (slow continuous nucleation), where A is either Ag or Ag^+ and B is the higher molecularity Ag_n and $Ag^+_{(n+1)}$ species,

[15] The authors measure the formation of Ag_6^+/zeolite-A, that is more rigorously something like $[+d[Ag_6^+/\text{zeolite-A}]/dt]_i = k_{obs}[Ag^+]_i^a[H_2]_i^b[\text{unknown species}]_i^c$. The Arrhenius equation is given by $k_{obs} = A \times \exp(-E_a/RT)$ and the typical plot of $\ln(k_{obs})$ vs. $1/T$ yields the (composite) activation energy (E_a). The problem is that the rigorous interpretation of such composite activation energies relies on knowledge of the precise mechanism of formation of Ag_6^+/zeolite-A. For a detailed example and derivation of how activation parameters propagate for composite steps, see elsewhere [199,200].

[16] The minimal, 2-step nucleation and autocatalytic growth mechanism mentioned once already was developed by Finke and Watzky while studying soluble [156,193], ligand-stabilized nanoparticle formation and their kinetics in solution [193]. The 2-step mechanism has also recently been shown to apply to the kinetics of formation of supported-nanoparticles in contact with solution [72,74,75], a topic that will be discussed in Section 3.

[17] The previously published kinetic data from Schoonheydt and co-workers [42] were digitized using Engauge Digitizer 2.12. The data were fit by the integrated analytical equation given elsewhere, corresponding to the two-step mechanism of A → B and A + B → 2B [193].

followed by A + B → 2B (autocatalytic surface growth). While the full implications of the fit shown in Fig. 7 remains to be established, that fit does provide a lead worthy of further investigation. To summarize, it is clear just from the shape of the kinetic curves that the presence of K^+ has changed the underlying nanoparticle formation mechanism from that when Na^+ is present [42].

In 2007, Shimizu et al. studied the formation of Ag_4^{2+} clusters on zeolite MFI from Ag^+/MFI under H_2 via EXAFS and UV–visible spectroscopy [57] (Entry 18, Table 2). Pseudo first-order rate constants were obtained from diffuse-reflectance UV–vis spectroscopy measurements over the temperature range of 573–913 K. Apparent activation energies were calculated from an Arrhenius plot and found to be the seemingly low value of 10 kJ/mol. Unfortunately, no specific mechanism was proposed making interpretation of the (apparent, composite[15] [199,200]) activation energy problematic. Note that this 10 kJ/mol activation energy is considerably smaller than the previous values obtained by Jacobs and co-workers [32,37] or by Schoonheydt et al. [42] (10 kJ/mol vs. 97.6, 49 and 47–60 kJ/mol, respectively). The range of activation energies suggests to us that one or more of these disparate values: (i) are suffering from so-called artifactual E_a vs. A (i.e., $\Delta H^{\ddagger}$ vs. $\Delta S^{\ddagger}$) compensation (in which, basically, the temperature range employed is insufficient to deconvolute $\Delta H^{\ddagger}$ from $\Delta S^{\ddagger}$) [201]; or (ii) are composites and need to be deconvoluted into the $\Delta H^{\ddagger}$ and $\Delta S^{\ddagger}$ values for their underlying steps to be meaningful [199,200].[15] Also possible here is (iii) that the different zeolites are playing a significant role in the supported-nanoparticle formation mechanism, or (iv) conceivably some combination of the above possibilities could be occurring. In any event, the need for further research on the Ag^+/support systems is apparent.

2.2.2.4. System IV: compositionally well-defined supported-organometallic complexes. So-called "single-site", compositionally well-defined, supported-organometallic complexes [202–204], along with various supported-organometallic clusters, are known, active catalysts for olefin polymerizations [205,206] and hydrogenations [100,207]. Furthermore, they can also be used as speciation controlled precatalysts en route to supported-nanoparticles [74,75]. In addition, such supported-organometallic precatalysts are particularly attractive for understanding the mechanisms of supported-nanoparticle heterogeneous catalyst formation as detailed in what follows. Speciation-controlled, supported-organometallics also typically contain organic ligands that can often be used as additional handles to monitor the decomposition of supported-precatalysts which, when combined with a direct technique for following M–M bond formation (or net $M(0)_n$ nanoparticle formation), can be powerful en route to the required balanced reaction stoichiometry for the nanoparticle formation reaction. Seven kinetic and mechanistic studies of the formation of supported-nanoparticles from supported-organometallic complexes are listed as Entries 19–25 in Table 2 [45,48,51,60,61,64,67]. These studies are covered next.

In 1998, Nuzzo, Frenkel, Shapley and co-workers studied the "nucleation and growth" of 1.5 nm $(Pt–Ru)_n$ nanoparticles from the well-defined $PtRu_5C(CO)_{16}$/activated-carbon precursor [45] (Table 2, Entry 19). A narrow (but non-reported) size distribution and atomically precise (1:5 Pt:Ru metal content) supported-nanoparticle product $(Pt–Ru)_n$/activated-carbon, resulted [101]. The structural evolution of the formation of $(Pt–Ru)_n$ supported on activated-carbon under H_2 (from 150 to 773 K) was followed via XANES and EXAFS. The EXAFS structural evidence is consistent with the author's proposed picture (Scheme 9) and word mechanism, in which "the initial nucleation of a compact (Pt-rich) structure (is) followed by the inversion of the intraparticle distribution of the Pt and Ru atoms upon continued high-temperature annealing". The authors further state "In this inversion, the core-segregated Pt atoms exchange with Ru surface atoms to form a surface Pt shell structure", all as depicted in Scheme 9. Nuzzo and co-workers' study (Scheme 9) is an important case history, one which sets a solid foundation for further investigation [157,208].[18] An important goal of those additional studies should be to provide a set of chemical-based equations that echo the authors' picture and word-based mechanism, so that the proposed mechanism can be tested kinetically.

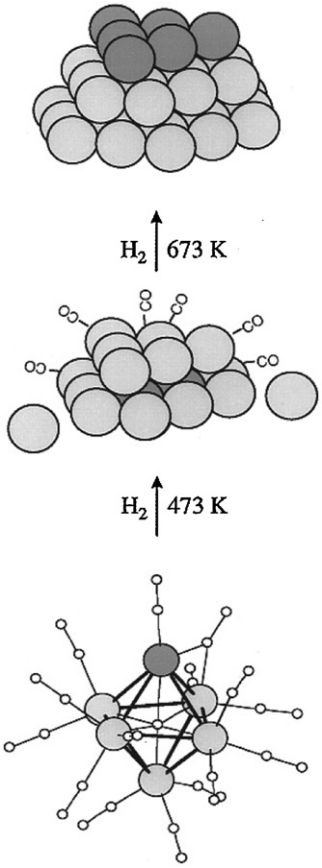

Scheme 9. Nuzzo and co-workers proposed pictorial mechanism for the conversion of $PtRu_5C(CO)_{16}$/activated-carbon into $(Pt–Ru)_n$/activated-carbon under H_2 (and a temperature ramp from 150 to 773 K) [45]. The light gray spheres represent Ru atoms, while the dark gray spheres represent Pt atoms.
Reprinted with permission from [45]. Copyright (1998) American Chemical Society.

In 2002, Newton and co-workers studied the formation of $Pt(0)_n$ nanoparticles supported on SiO_2 from a $Pt(acac)_2/SiO_2$ precursor (where acac = acetylacetonato) under H_2, and separately N_2, environments from 300 to 673 K (Table 2, Entry 20) [48]. The presence of a reducing environment clearly changes the resultant products—"larger" $Pt(0)_n/SiO_2$ nanoparticles (based on the Pt–Pt coordination number obtained from EXAFS) were observed under

[18] An important point here is the emerging role of the ligands present, in bi- or higher-multimetallic nanoparticles, in determining which metal winds up on the surface vs. in the core. Normally, one expects the "heavier" metal, with its higher M–M bond strengths and associated higher $\Delta H_{vaporization}$ [157] to reside in the core of a multimetallic nanoparticle or "nano onion", where a greater number of those stronger M–M bonds can be achieved. Good evidence of this expectation exists, see footnotes 38 and 39 elsewhere [157]. However, the ligands present, along with the stronger metal–ligand bond energies for the heavier metal, can draw that heavier metal to the surface [208]. In short, the extensive but still evolving literature of bimetallic and higher multimetallic nanoparticles is currently striving to understand these and the other competing factors that determine the structures of ligated, bimetallic and higher multimetallic nanoparticles, studies beyond the scope of this review.

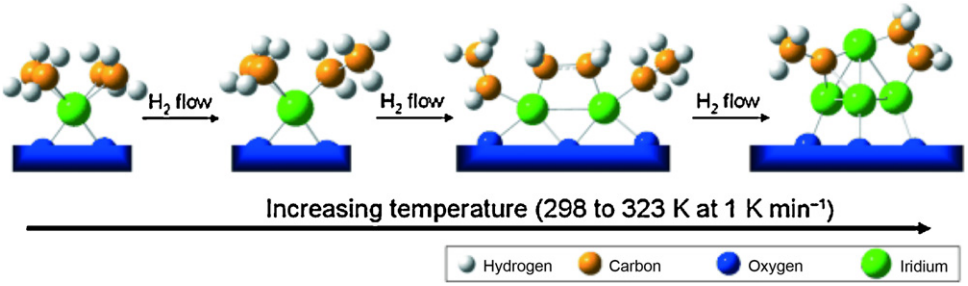

Scheme 10. Gates and co-workers proposed pictorial mechanism for the formation of $Ir_4(ligand)_x$/zeolite-Y under H_2 and a 298–323 K temperature ramp [60]. In this scheme, the white spheres are H, the orange spheres C, the blue spheres O and the green spheres Ir. (For the color version of this figure, the reader is referred to the web version of the article.)

H_2 vs. N_2. EXAFS was used to follow the kinetics of the Pt–Pt bond formation under both the H_2 and N_2 environments. As just one example, the kinetic data (for the formation of $Pt(0)_n/SiO_2$) reveals that the Pt–Pt coordination number increased from 0 to about 9 over a very short temperature range of 15 K, starting at approximately 350 K. The authors suggest that this is "indicative of some form of autocatalysis", which is corroborated by the sigmoidal shape of their kinetic data. The authors attribute this autocatalysis to "an initial decomposition of a small fraction of the supported $Pt(acac)_2$ leading to the formation of a low level of small Pt particles. . . (which are) active for rapid H_2 dissociation and subsequent spillover of atomic hydrogen". In other words the authors hypothesize that H• spillover is the cause of the formation of the larger $Pt(0)_n/SiO_2$ particles under H_2 vs. N_2. However, very similar kinetics are observed for the decomposition of $Pt(acac)_2/SiO_2$ under N_2, data which seem inconsistent with the key role hypothesized for H• spillover. One attractive alternative hypothesis here is that mobile hydride species (e.g., $[Pt–H]^0$), such as those proposed by Dalla Betta and Boudart [29] are present, a hypothesis consistent with the prior literature [29,72,74,75]. An important goal of the needed additional work here is, again, to write rigorous chemical-based mechanisms, followed by attempts to disprove those and any other, plausible alternative mechanistic hypotheses.

In 2004, Gates and co-workers studied the formation of $Ir_4(CO)_{12}$/zeolite-Y from a $Ir(CO)_2(acac)$/zeolite-Y precatalyst under CO [51] (Table 2, Entry 21). The progress of the reaction was qualitatively followed using IR spectroscopy, the important, classic spectroscopic handle for metal carbonyl complexes and clusters. A ν_{CO} stretching frequency at 1818 cm^{-1}, indicative of edge-bridging CO ligands, was assigned to a $Ir_2(CO)_8$/zeolite-Y intermediate en route to the $Ir_4(CO)_{12}$/zeolite-Y product. The assignment of the $Ir_2(CO)_8$ intermediate was corroborated by ex situ EXAFS analysis which revealed the presence of Ir–Ir scatterers. Gates and co-workers suggested that the formation of the $Ir_4(CO)_{12}$/zeolite-Y product occurs in a similar manner to known solution-based carbonyl chemistry [209] as shown in Eqs. (4) and (5). This, then, is another valuable, classic system where detailed kinetic investigations promise to prove informative.

$$IrCl_3(l) + 3CO + H_2O \rightarrow [Ir(CO)_2Cl_2]^-(l) + Cl^- + 2H^+ + CO_2 \quad (4)$$

$$4[Ir(CO)_2Cl_2]^-(l) + 6CO + 2H_2O \rightarrow Ir_4(CO)_{12}(l) + 2CO_2 + 4H^+ + 8Cl^- \quad (5)$$

Subsequently, starting from a well-defined $Ir(C_2H_4)_2$/zeolite-Y precursor, Gates and co-workers studied the formation of $Ir_4(ligand)_x$/zeolite-Y [60] (where the ligand structure was proposed to contain ethylidyne and di-σ-bonded ethylene) under H_2 from 298 to 353 K (Entry 22, Table 2) [210,211]. The $Ir(C_2H_4)_2$/zeolite-Y precursor was thoroughly characterized via IR and EXAFS spectroscopies [210] and, later, via aberration-corrected high-angle annular dark-field scanning TEM (HAADF STEM) [211]. Importantly in this well-executed study, a powerful combination of complimentary physical techniques of XANES, EXAFS and IR spectroscopies were used to follow the loss of the $Ir(C_2H_4)_2$/zeolite-Y precursor and the formation of the $Ir_4(ligand)_x$/zeolite-Y product [60]. The XANES data at the Ir L_{III} edge indicated five identifiable isosbestic points, which are consistent with the transformation of the $Ir(C_2H_4)_2$/zeolite-Y into (just) the $Ir_4(ligand)_x$/zeolite-Y. The time-resolved EXAFS data show the formation of Ir–Ir contributions and the loss of Ir–low Z contributions (i.e., Ir–ligand loss). The final Ir–Ir coordination number (N_{Ir-Ir}) was found to be approximately 3, which is consistent with the formation of Ir_4 clusters supported on zeolite-Y. The IR spectroscopy data also indicate the formation of di-σ-bonded ethylene ligands at the onset of Ir–Ir bond formation, data further consistent with the formation of the $Ir_4(ligand)_x$/zeolite-Y. One proposed mechanism for the formation of the $Ir_4(ligand)_x$/zeolite-Y supported cluster is pictorially reproduced in Scheme 10. Gates and co-workers caution that the proposed structures are "simplified" and were careful to note that there is "no direct evidence of the dinuclear intermediate species". Interestingly, the $Ir_4(ligand)_x$/zeolite-Y undergoes fragmentation back to the mononuclear $Ir(C_2H_4)_2$/zeolite-Y precatalyst under C_2H_4.

Gates and co-workers also studied the reduction of the analogous $Rh(C_2H_4)_2$/zeolite-Y precatalyst using the same methodology (Table 2, Entry 23)—the largest difference was that a $Rh_{2-3}(ligand)_x$/zeolite-Y product was formed during isothermal reduction at 298 K in H_2 [61] (i.e., and in comparison to the temperature ramp from 298 to 323 K for the $Ir(C_2H_4)_2$/zeolite-Y to $Ir_4(ligand)_x$/zeolite-Y zeolite system [60]). Significantly, the precise nuclearity of the subnanometer catalysts present, for both the Rh [212] and the Ir [213] systems, proved highly dependent on the reactive environment and specifically on the H_2/C_2H_4 ratio: higher H_2 ratios favor multinuclear clusters, while higher C_2H_4 ratios favor the mononuclear form [61,213].

To summarize, all of the data for the $Ir(C_2H_4)_2$/zeolite-Y to $Ir_4(ligand)_x$/zeolite-Y supported-cluster formation are consistent with Gates' and co-workers proposed pictorial mechanism, Scheme 10. Indeed, this example from the Gates' group is illustrative of how establishing "just" the balanced reaction is very powerful mechanistically for supported-nanoparticle formation studies—and for materials chemistry in general! This example also illustrates that getting "just" that balanced stoichiometry often takes considerable, focused effort using multiple physical tools. The system in Scheme 10 is, therefore, a prime candidate for the next level of kinetics and associated chemical-reaction-based mechanistic studies. Some collaborative efforts towards this goal are currently underway [214].

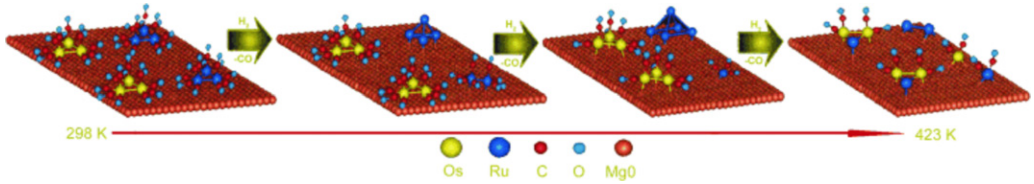

Scheme 11. Gates' and co-workers' proposed pictorial model for bimetallic $(Ru_xOs_y)_n$/MgO cluster formation from $[Ru_3(CO)_{12}]$ and $[Os_3(CO)_{11}]^{2-}$ supported on MgO under H_2 (and a temperature ramp from 298 to 423 K) [64]. In this scheme, the yellow spheres are Os, the dark blue spheres Ru, the red spheres C, the light blue spheres O and the orange spheres are the MgO support. (For the color version of this figure, the reader is referred to the web version of the article.)

In 2009, Gates and co-workers also studied the formation of the bimetallic $[H_2Os_3Ru(CO)_{13}]$/MgO cluster from $[Ru_3(CO)_{12}]$ and $[Os_3(CO)_{11}]^{2-}$ supported on MgO under H_2 and over the temperature range of 298–423 K [64] (Entry 24, Table 2). Again a powerful combination of complimentary physical techniques, XANES, EXAFS and IR spectroscopy were used to follow the loss of the precursors and formation of $(Ru_xOs_y)_n$/MgO. Because of the multiple methods used, the authors were able to show that the supported product still contains some of both of the $[Ru_3(CO)_{12}]$ and $[Os_3(CO)_{11}]^{2-}$ precatalysts. The IR spectroscopy also indicates that the bimetallic product closely resembles $[H_2Os_3Ru(CO)_{13}]$/MgO, and the EXAFS data are consistent with that interpretation. The authors suggest that the mechanism of $[H_2Os_3Ru(CO)_{13}]$/MgO occurs, as pictorially described in Scheme 11, via "first, the decarbonylation of triruthenium clusters starting at 333 K (with the triosmium carbonyl clusters still being coordinatively saturated and intact)". The authors also note that "The coordinatively unsaturated ruthenium species were reactive and, at 333 K, had aggregated substantially so that the average ruthenium cluster was larger than triruthenium. When the temperature had been raised to about 358 K, the triosmium clusters began to undergo decarbonylation, and at approximately 398 K the triosmium clusters had lost enough CO ligands to become sufficiently coordinatively unsaturated to allow migration and reaction with Ru atoms of neighboring species". Overall, this is another important system, developed by the Gates group, that merits additional kinetic and mechanistic studies en route to fully understanding bimetallic nanoparticle formation from well-defined, supported-organometallic complexes, namely metal carbonyl clusters in this latter case.

Finishing with very recent work, in 2010 Nassreddine et al. studied the formation of 1.2 nm $Ir(0)_n$ nanoparticles supported on amorphous silica alumina (ASA) from a $Ir(acac)_3$/ASA precursor under H_2 [67]. The formation of $Ir(0)_n$/ASA was followed by in situ XRD from 0 to 700 °C. The authors found that the $Ir(0)_n$/ASA particle size grows gradually from 0 to 300 °C and then slows down and remains constant at 1.2 nm above 500 °C. However, considering that the $Ir(0)_n$ particles cannot be detected until 200 °C, it is not clear if the particle size truly increases linearly below 200 °C. No mechanism was proposed for the formation of the $Ir(0)_n$/ASA product.

2.2.3. Conclusions

The eight $M(NH_3)_4^{2+}$ ($M = Pt^{2+}$, Pd^{2+}) case studies reveal that $M(0)_n$, M^{x+} or $(M_xO_y)_n$ species can form on the support during the precatalyst preparation steps and that those (different) species can have different kinetics of supported-nanoparticle formation [50,58,62,63]—results that reiterate the importance of precisely controlling the precatalyst speciation, ideally in all future syntheses of heterogeneous catalysts. While kinetic studies are in hand for the $M(NH_3)_4^{2+}$/support systems, no rigorous chemical-reaction-based mechanisms have been proposed for the formation of the resultant $M(0)_n$ supported-nanoparticle products. Dalla Betta and Boudart [29], as well as Konigsberger and co-workers [47], have suggested that a neutral "$Pt(NH_3)_2H_2$" intermediate is responsible for the formation of $Pt(0)_n$ nanoparticles supported on zeolite-Y and SiO_2, although, no compelling—and certainly no direct—evidence for that putative Pt–H intermediate exists at present. Hence, further studies attempting to detect the putative "$Pt(NH_3)_2H_2$" intermediate under the in situ nanoparticle formation conditions, for example with a combination of *in operando* XAFS plus IR spectroscopy, are hereby identified as an important, future research goal. Okumura and co-workers have demonstrated that the $Pd(0)_{\sim 13}$/H–USY supported-nanoparticle formation kinetics from Pd^{2+}/H–USY are first order in Pd^{2+} and Pd–Pd (i.e., $-d[Pd^{2+}]/dt \propto [Pd^{2+}]^1\,[Pd\text{–}Pd]^1$) [62,63]; three deliberately minimal mechanisms have been suggested herein (and were shown back in Scheme 4), mechanisms that can account for the observed kinetic data and which employ the aforementioned, putative Pd–H intermediate. The fact that the kinetics are separately first-order in both Pd^{2+} and Pd–Pd, and not bimolecular in any Pd species (e.g., $-d[Pd^{2+}]/dt = k_{obs}[Pd^{2+}]$, but not $-d[Pd^{2+}]/dt = k_{obs}[Pd^{2+}][Pd\text{–}Pd]$), demands that some of the supported-nanoparticle formation steps occur post the rate-determining step and are, therefore, kinetically hidden. Hence, conditions that unmask those later steps are and additional, important goal for future research.

Inspection of the five H_2PtCl_6 case studies reveals that the known speciation of H_2PtCl_6 in aqueous solution, as well as in the presence of metal-oxide supports [162–166], has been largely ignored in the extant kinetic and mechanistic literature of $Pt(0)_n$ supported-nanoparticle formation from the classic H_2PtCl_6 precursor. Chupas et al. demonstrated zero-order kinetics (i.e., $[H_2PtCl_6]^0$) for the H_2PtCl_6/TiO_2 to $Pt(0)_n/TiO_2$ system [56]. Two mechanisms, which can account for the observed zero-order H_2PtCl_6/TiO_2 kinetics, as well as the $Pt(0)_n/TiO_2$ supported-nanoparticle products, were shown back in Scheme 5. The observation that the kinetic data are zero-order in H_2PtCl_6/TiO_2, and not bimolecular in any supported Pt species, but still yield a Pt–Pt bonded, $Pt(0)_n/TiO_2$ product suggests that the desired nanoparticle formation steps are kinetically hidden. Hence, hereby identified as important steps in advancing our understanding of the formation of supported-nanoparticle catalysts, from the classic H_2PtCl_6 precatalyst (and once the speciation issues with this precatalyst are resolved first), are: (i) continuing to write out specific balanced reactions corresponding to the proposed mechanistic steps; (ii) being sure those reaction steps add up to the observed, experimentally demonstrated reaction stoichiometry, and then (iii) executing the needed kinetic studies that unmask the desired supported-nanoparticle formation steps from any diffusion-limited processes present.

The five $Ag(NO_3)$ case studies contain, by far, the most-detailed chemical-reaction-based mechanisms to date for supported-nanoparticle formation at the gas–solid interface. Importantly, Jacobs and co-workers were able to establish the supported-nanoparticle formation stoichiometry by using H_2 uptake measurements [32,33,37]. In addition, the classic studies of Jacobs and co-workers focus on the reduction step for those Ag^+/zeolite based systems. The accompanying kinetic studies reveal that the desired supported-nanoparticle formation steps are again masked by diffusion of $H^\bullet$ and Ag^+ towards each other. Three different chemical-reaction-based mechanisms, Schemes 6 and 8, were

proposed for the formation of Ag(0) or Ag_n^{x+} species [32,33,37]. Hence, future studies that unmask the kinetics of those important supported-nanoparticle formation steps are highly desirable.

An important insight is that diffusion-limited processes are common in the mechanisms of supported-nanoparticle formation reactions at the gas–solid interface. It means that consideration of diffusion-limitations need to be undertaken in the design of future kinetic and mechanistic studies of supported-nanoparticle formation reactions at the gas–solid interface.

The seven kinetic and mechanistic studies starting from supported-organometallic precursors demonstrate that well-defined, speciation-controlled precatalysts can be and have been synthesized. Additional benefits when starting from well-defined, speciation-controlled, supported organometallics include: (i) the presence of organic ligands, which offer additional handles such as IR spectroscopy for following the reactions and their kinetics, and (ii) systems which have precedented solution-based chemistry for comparison purposes (and which therefore can, in favorable cases, also yield otherwise unobtainable insights). Unfortunately, to date no rigorous kinetic and mechanistic studies, starting from well-defined supported organometallic complexes, have been reported for gas–solid supported nanoparticle formation systems. However, many of the supported organometallic systems, in particular Gates and co-workers $M(C_2H_4)_2$/zeolite (M = Ir, Rh) systems [60,61], are prime systems for the desired kinetic and mechanistic studies—ones where the hard first step of preparing and characterizing the system is now in hand.

In short, the above case studies of the $M(NH_3)_4^{2+}$ ($M = Pt^{2+}, Pd^{2+}$), H_2PtCl_6, $Ag(NO)_3$ and supported-organometallic systems provide a solid foundation of work upon which to build. However, much remains to be done. Recommended focal points include: (i) controlling the precatalyst speciation, ideally to one supported species; (ii) determining experimentally the complete, balanced supported-nanoparticle formation stoichiometry, including trace metal and other products where possible; (iii) ensuring if possible that diffusion is not masking the desired supported-nanoparticle formation kinetics; (iv) writing chemical-reaction-based mechanisms,[8] rather than the word- and picture-based schemes or cartoons that currently dominate the supported-nanoparticle formation literature, so that those mechanisms can be tested kinetically, and then (v) disproving multiple alternative mechanisms/hypotheses[11] rather than asserting a single mechanism emphasizing the author's preferences/beliefs. Mechanism, like science in general, proceeds only via conclusive disproof of multiple alternative hypotheses (Platt, *op. cit.*[11]).

There is also arguably a need to bridge the practical gas–solid mechanistic systems discussed herein with the cleaner, better-studied, UHV counterparts where available, assuming their associated temperature, pressure and materials gaps [76–79] can be bridged/overcome. The eventual goal is to have a uniform, cohesive mechanistic picture of heterogeneous catalyst formation, and their resultant catalysis, a picture that spans the knowledge available from UHV to that from practical supported-nanoparticle science to what is known in organic, organometallic and inorganic chemistry. Merging those existing areas of knowledge will then yield insights sufficient to drive the synthesis of the next generation of composition-, size- and shape-controlled supported-nanoparticle catalysts. This includes heterogeneous catalysts synthesized in contact with solution, as discussed next.

3. Studies of supported-nanoparticles in liquid–solid systems

Recent advances in solution-based nanoparticle syntheses [134,215–223] have resulted in significantly improved control over the resultant nanoparticle composition [224–230], size [156,231] and shape [232–235]. Kinetic and mechanistic insights into nanoparticle formation—that is, into nucleation, autocatalytic growth, bimolecular agglomeration and autocatalytic agglomeration—have also been obtained [114,190–194,236–240], insights possible in part due to the greater ease of full product, balanced stoichiometry, and kinetic and mechanistic studies for solution vs. solid-state reactions. Indeed, the systems and discussion which follow strongly suggest that the synthetic and mechanistic insights, available from a relative short period of solution nanoparticle syntheses and mechanistic studies, already come close to surpassing all those generated from all of the aforementioned studies at the gas–solid interface. Hence, an important goal in modern heterogeneous catalysis is to transfer the synthetic and mechanistic insights, from the modern revolution in nanoparticle synthesis and mechanistic study in solution, to the synthesis of solid-supported-nanoparticle heterogeneous catalysts.

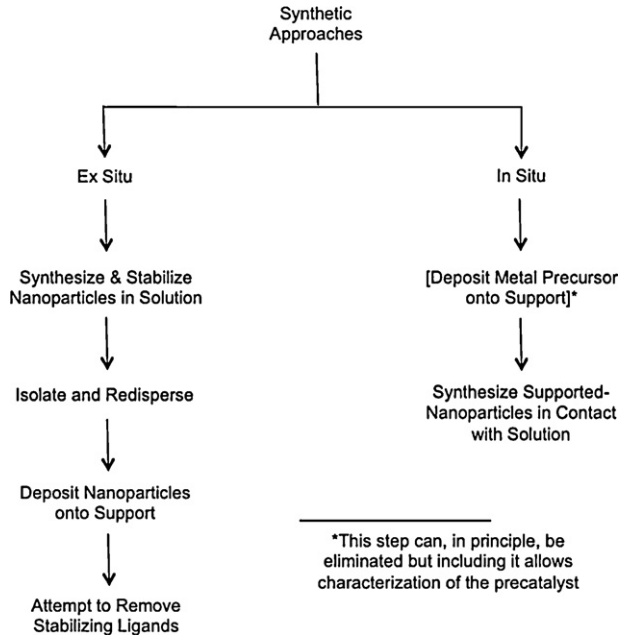

Scheme 12. Two emerging, limiting synthetic approaches for the preparation of supported-nanoparticle heterogeneous catalysts in contact with solution (i.e., in liquid–solid systems).

3.1. Fundamental background information regarding supported-nanoparticle heterogeneous catalyst formation in liquid–solid systems

Before reviewing the kinetic and mechanistic studies of supported-nanoparticle heterogeneous catalyst formation in contact with solution—that is, in liquid–solid systems—it will prove useful to describe first, but briefly, the synthetic methods for preparing supported-nanoparticles in liquid–solid and gas–liquid–solid systems. The physical methods for following the kinetics of those reactions will also be briefly summarized to start, all as an aid to the reader in understanding what follows.

3.1.1. Emerging synthetic strategies for the preparation of supported-nanoparticle catalysts in solution (i.e., liquid–solid systems)

Two limiting routes have emerged using solution-prepared transition metal nanoparticles to synthesize supported-nanoparticle heterogeneous catalysts (Scheme 12). The first method attempts to take advantage of the nanoparticle

community's ability to make stabilized transition-metal nanoparticles in solution (often with polymer or other ligands present to prevent nanoparticle aggregation [215–223]). Those stabilized nanoparticles are then typically isolated, redispersed and subsequently deposited onto a support [241–248]. Unfortunately however, the polymer or other bulky, often massive stabilizers are invariably and unavoidably co-deposited. This is as expected, given that typical metal–ligand dative bonds are 25–40 kcal/mole or more [25,26]. Complete removal of the stabilizing polymer or other ligands—as is required for the most coordinatively unsaturated and hence, facile catalysts [249]—has proven difficult to impossible [247,248,250–262]. Extensive treatments such as thermal activation in N_2, H_2 and O_2 environments [250–252], UV/ozone [253–256], O_2/plasma [256] and even neutron sputtering [257] have been largely unsuccessful in removing completely all the polymeric or other organic ligand "debris"—although claims of "complete" removal of all ligands or polymers continue to appear without controls demonstrating detectability limits, and thus the error bars, on the true level of "debris" removal. The resultant, partially poisoned, supported-nanoparticles are then, and in turn, also rendered compositionally ill-defined. The supported-nanoparticle's size and shape can also be altered by the harsh thermal, oxidative, reductive or other treatments attempting to fully remove the poisoning ligands or polymers [250–262].

A second, arguably more attractive synthetic approach—one now attracting increasing attention [263–277]—is to start from supported molecular precursors and then synthesize the supported-nanoparticles in situ, that is, in contact with solution. Ideally in this approach, only the desired catalytic reaction substrates or other desired ligands are present, thereby leading to what has been termed "weakly ligated/labile ligand nanoparticles" [104,223,278,279].[19] This in situ method can, at least in principle, provide superior control over the resultant supported-nanoparticle composition, size and shape since one can readily add desired solvents, ligands, and other additives or "promoters" as desired during the synthesis—all assuming that a careful, preferred selection of ligands and solvents can be selected en route to composition controlled, non-ligand-poisoned, "weakly ligated/labile ligand" [104,223,279] supported-nanoparticles.

3.1.2. Characterization methods for following the kinetics of supported-nanoparticle heterogeneous catalyst formation in liquid–solid systems

In principle, each of the physical methods capable of following the kinetics of supported-nanoparticle formation at the gas–solid interface (Table 1) could also be utilized in liquid–solid systems. Despite this, no direct, *in operando* (or in situ) methods have yet been utilized to follow the kinetics of supported-nanoparticle formation in liquid–solid systems; to date, only H_2 uptake and ex situ TEM and AFM have been utilized for following the kinetics of supported-nanoparticle formation.

3.1.3. Conclusions from the brief, fundamental background section on liquid–solid systems

The synthesis of supported-nanoparticles in liquid–solid systems is attractive since it has the potential to allow the synthetic and mechanistic insights, from the modern revolution in nanoparticle syntheses in solution (including control over the nanoparticle size, shape and composition), to be transferable to the synthesis of supported-nanoparticles, at least in principle. Moreover, many of the physical methods listed back in Table 1 should be applicable to studies of liquid–solid systems. However, to date the use of direct, *in operando* (or in situ) techniques to follow supported-nanoparticle formation kinetics in liquid–solid systems has not been reported, so that providing such studies *in operando* is an obvious, needed area of future research.

3.2. Kinetic and mechanistic studies of supported-nanoparticle formation in liquid–solid systems

3.2.1. Brief overview of the primary literature

Table 3 is a compilation of the eight available studies striving to understand the mechanisms of supported-nanoparticle heterogeneous catalyst formation in liquid–solid systems. Table 3 details: (i) the experimental preparation and nanoparticle formation conditions; (ii) whether the study contains kinetic data and, if so, by which method(s) those data were obtained; (iii) whether the stoichiometry of the supported-nanoparticle formation reaction was obtained, and if so how; and finally (iv) the proposed mechanism and rate equations as given by the original authors, if available.

A brief inspection of Table 3 is quite informative and reveals several global insights into the state of mechanistic knowledge for supported-nanoparticle heterogeneous catalyst formation in liquid–solid systems. First, there are only 8 studies in liquid–solid supported-nanoparticle formation systems to date—only 1/5th as frequent as the more common, 39 studies of gas–solid systems. In 7 of the 8 studies of liquid–solid systems, kinetic data have been collected, but, as already noted no study has used a direct method that is also at least in situ. However, in 3 of the 8 cases a supported-nanoparticle heterogeneous catalyst formation stoichiometry has been explicitly demonstrated, kinetic data have been collected and a chemical-reaction-based mechanism has been proposed, one that is both consistent with the kinetic data and where one or more alternative mechanistic pathways have been disproved.[11] Finally, the first liquid–solid study in Table 3 was reported in 2004, two of the studies in 2006, with the remaining 5 studies of the 8 total from the period 2009–2011. Clearly the study of supported-nanoparticle formation, in contact with solution is a much younger, still wide-open area of investigation.

3.2.2. Kinetic and mechanistic case studies

3.2.2.1. Wang et al.'s study of the formation of $Pt(0)_n$ on carbon nanotubes. In 2006 Wang et al. studied the formation of $Pt(0)_n$ on carbon nanotubes (CNTs) from a mixture of H_2PtCl_6 in ethylene glycol, sodium dodecyl sulfate (SDS) and CNTs [69] (Table 3, Entry 2). The authors were able to control the $Pt(0)_n$/CNT nanoparticle size over a range of 2.3–9.6 nm (with 12–44% dispersities) by varying the concentration of H_2PtCl_6, the temperature and the reducing agent. It is likely that the use of the organic solvent helps minimize the H_2PtCl_6 speciation and allows the formation of the near-monodisperse (i.e., $\leq \pm 15\%$ [215]) 2.3 ± 0.3 $Pt(0)_n$/CNT catalyst—although the precise speciation of the H_2PtCl_6 precatalyst is once again an issue. Wang et al. proposed a mechanism of supported-nanoparticle heterogeneous catalyst formation consisting of "...heterogeneous nucleation (which becomes favorable) once the critical nucleus size is attained, autocatalytic growth of the particle rapidly depletes the Pt-monomer concentration in solution, thereby effectively depressing homogeneous nucleation", as summarized pictorially in Scheme 13. Unfortunately, the needed kinetic studies were not performed to support or refute the authors' proposed mechanistic hypothesis. In the one case where solid-support-based (i.e., heterogeneous) nucleation vs. solution (i.e., homogeneous) nucleation has been kinetically tested [75], homogeneous nucleation was observed, Scheme 18 (vide infra), not the heterogeneous nucleation proposed in Scheme 13. Hence, at present and until the needed

[19] "Weakly ligated/labile ligand" nanoparticles are simply nanoparticles where only weakly coordinated ligands plus the desired reactants are present [104]. Related topics include "putative cation-only stabilized nanoparticles" [223] and "putative solvent-only stabilized nanoparticles" [279], neither of which actually appears to exist [104,223,279].

Table 3
The kinetic and mechanistic studies of supported-nanoparticle heterogeneous catalyst formation in liquid–solid systems.

Entry [Reference]	Authors	System of study	Kinetic data (physical method)	Stoichiometry (physical method)	Proposed mechanism(s) and rate equations as written by the original authors (if available)
1 [68]	Singh, A.; Luening, K.; Brennan, S.; Homma, T.; Kubo, N.; Pianetta, P.	Si wafers were dipped into a Cu–2% nitric acid matrix.	Yes atomic force microscopy (AFM)	No	*Proposed mechanism*. The authors assert that the Cu grows via an Ostwald-ripening mechanism.
2 [69]	Wang, Y.; Xu, X.; Tian, Z.; Zong, Y.; Cheng, H.; Lin, C.	50-wt% H_2PtCl_6, ethylene glycol (as the solvent and reducing agent), carbon nanotubes (CNTs), and sodium dodecyl sulfate (SDS) were mixed together and sonicated, and then heated and stirred.	No	No	*Proposed mechanism*. "Salt effects increase the barrier towards homogeneous nucleation, such that heterogeneous nucleation becomes more favorable. Once the critical nucleus size is attained, autocatalytic growth of the particle rapidly depletes the Pt-monomer concentration in solutions, thereby effectively depressing homogeneous nucleation", that is pathway 2B in Scheme 13.
3 [70]	Marre, S.; Cansell, F.; Aymonier, C.	$Cu(hfac)_2{\bullet}H_2O$ was mixed with SiO_2 spheres, in isopropyl alcohol, CO_2 and H_2 and brought to supercritical conditions.	Yes (ex situ TEM)	No	*Proposed mechanism*. The author's (word-based) mechanism consists of (i) homogenous decomposition to Cu nuclei, which are then (ii) deposited onto the SiO_2 surface, followed by (iii) direct growth of the nuclei on the SiO_2 surface.
4 [71]	Marre, S.; Erriguible, A.; Perdomo, A.; Cansell, F.; Marias, F.; Aymonier, C.	$Cu(hfac)_2{\cdot}H_2O$ reduced in situ with SiO_2 spheres.	Yes (ex situ TEM)	No	*Proposed mechanism*. The authors suggest a mechanism consisting of homogeneous nucleation followed by heterogeneous growth, as depicted in Scheme 14.
5 [72]	Mondloch, J.E.; Yan, X.; Finke, R.G.	1.96-wt% H_2PtCl_6 was slurried with either γ-Al_2O_3 or TiO_2 in a solution of ethyl acetate. The solution was taken to dryness under vacuum. The precatalyst was reduced in EtOH plus cyclohexene under 40 psig of H_2 at 22 °C.	Yes (H_2 uptake—cyclohexene reporter reaction[a])	Yes ($pH_{apparent}$ measurements)	*Proposed mechanism* $A \xrightarrow{k_1} B$ (Nucleation); $n\,Pt^{IV} \xrightarrow{H_2} Pt(0)_n$ $A + B \xrightarrow{k_2} 2B$ (Autocatalytic Surface Growth); $Pt^{IV} + Pt(0)_n \xrightarrow{H_2} Pt(0)_{n+1}$ where A is the supported precatalyst H_2PtCl_6/Al_2O_3 and B is the growing $Pt(0)_n$ nanoparticle surface *Integrated rate equation* $[A]_t = \frac{(k_1/k_2)+[A]_0}{1+(k_1/(k_2[A]_0))\exp(k_1+k_2[A]_0)_t}$
6 [73]	Rossi, L.M.; Nangoi, I.M; Costa, N.J.S.	Between 1.34 and 1.76-wt% $Pd(acetate)_2$ was slurried onto ligand-modified SiO_2 spheres (e.g., modified with (3-aminopropyl)triethoxy-silane) from toluene. The sample was washed with ethanol and acetone and dried under vacuum. The precatalyst was placed in toluene and reduced under H_2 (6 atm) at 75 °C.	Yes (H_2 uptake—cyclohexene reporter reaction[b])	No	No mechanism was proposed by the authors; however, they did note that "additional experiments and control arrangements are in progress in order to elucidate the mechanism of supported-nanoparticle formation".

Table 3 (*Continued*)

Entry [Reference]	Authors	System of study	Kinetic data (physical method)	Stoichiometry (physical method)	Proposed mechanism(s) and rate equations as written by the original authors (if available)
7 [74]	Mondloch, J.E.; Wang, Q.; Frenkel, A.I.; Finke, R.G.	$[Ir(1,5\text{-COD})Cl]_2$ was slurried with γ-Al_2O_3 in ethyl acetate and taken to dryness under vacuum. The $Ir(1,5\text{-COD})Cl/\gamma\text{-}Al_2O_3$ precatalyst was reduced under H_2 in acetone at 22 °C.	Yes (H_2 uptake—cyclohexene reporter reaction[a])	Yes (H_2 uptake, cyclooctane evolution)	*Proposed mechanism* $A \xrightarrow[\text{Nucleation}]{k_1} B$ $\quad 2n\ Ir^I \xrightarrow{H_2} 2/n\ Ir(0)_n$ $A + B \xrightarrow[\text{Autocatalytic Surface Growth}]{k_2} 2B$ $\quad Ir^I + Ir(0)_n \longrightarrow Ir(0)_{n+1}$ where A is the supported precatalyst $Ir(1,5\text{-COD})Cl/\gamma\text{-}Al_2O_3$ and B is the growing $Ir(0)_n$ nanoparticle surface. *Integrated rate equation* $[A]_t = \frac{(k_1/k_2)+[A]_0}{1+(k_1/(k_2[A]_0))\exp(k_1+k_2[A]_0)_t}$
8 [75]	Mondloch, J.E.; Finke, R.G.	$[Ir(1,5\text{-COD})Cl]_2$ was slurried with γ-Al_2O_3 in ethyl acetate and taken to dryness under vacuum. The $Ir(1,5\text{-COD})Cl/\gamma\text{-}Al_2O_3$ precatalyst was reduced under H_2 in acetone (and acetone plus cyclohexane) at 22 °C.	Yes (H_2 uptake—cyclohexene reporter reaction[a])	Yes (H_2 uptake, cyclooctane evolution)	*Proposed mechanism*[c] $Ir^I/Al_2O_3 + solvent \overset{K_{Diss}}{\rightleftharpoons} Ir^I{*}solvent + Al_2O_3$ $Ir^I{*}solvent \xrightarrow[2.5\ H_2]{k_1'} Ir(0)_{soln} + solvent$ $Ir^I/Al_2O_3 + solvent \overset{K_{Diss}}{\rightleftharpoons} Ir^I{*}solvent + Al_2O_3$ $Ir(0)_{soln} + Al_2O_3 \xrightarrow{Fast} Ir(0)/Al_2O_3$ $Ir^I{*}solvent + Ir(0)/Al_2O_3 \xrightarrow[2.5\ H_2]{k_2''} 2\,[Ir(0)/Al_2O_3] + solvent$ SUM: $[Ir^I/Al_2O_3]_{sus} \xrightarrow[2.5\ H_2]{k_{obs}''} [Ir(0)/Al_2O_3]_{sus}$ where Ir^I/Al_2O_3 is $Ir(1,5\text{-COD})Cl/\gamma\text{-}Al_2O_3$, solvent is acetone and $Ir^I{*}$solvent is Ir(1,5-COD)Cl(solvent) and the rate and equilibrium constants are defined in Scheme 17. *Integrated rate equation*[d] $[A]_t = \frac{(k_{1obs}/k_{2obs})+[A]_0}{1+(k_{1obs}/(k_{2obs}[A]_0))\exp(k_{1obs}+k_{2obs}[A]_0)_t}$ where k_{1obs} and k_{2obs} are given by $k_{1obs} = \frac{k_1' K_{Diss}[solvent]_t}{[Al_2O_3]_{sus,t} + K_{Diss}[solvent]_t}$ $k_{2obs} = \frac{k_2'' K_{Diss}[solvent]_t}{[Al_2O_3]_{sus,t} + K_{Diss}[solvent]_t}$

[a] The appropriate [cyclohexene]^0 control reaction was demonstrated to ensure that the reporter reaction was functioning properly.

[b] The appropriate [cyclohexene]^0 control reaction was not demonstrated to ensure that the reporter reaction was functioning properly.

[c] This mechanism applies only rigorously to the supported-nanoparticle formation reactions carried out in acetone. A slightly modified mechanism (with, however, the same general form) accounts for the mixed solvent case of acetone plus cyclohexane [75].

[d] These rate equations only apply rigorously to the supported-nanoparticle formation reactions carried out in acetone. Slightly modified rate equations (with, however, the same general form) were provided to account for the mixed solvent case of acetone plus cyclohexane [75].

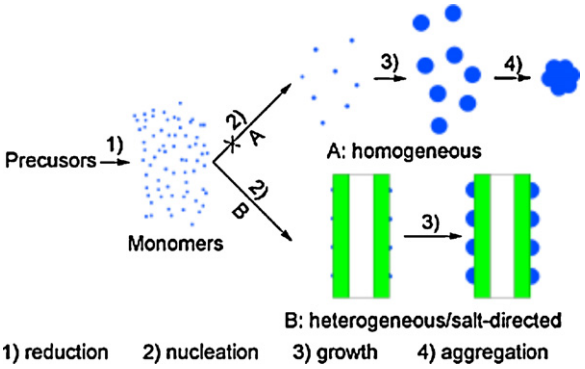

Scheme 13. Pictorial mechanisms proposed by Wang et al. [69] for the formation of $Pt(0)_n$/CNT in contact with solution. The authors favor the bottom pathway consisting of heterogeneous nucleation and growth, a pathway that is, however, not supported by the one available kinetic study to date (albeit of a different, Ir-based system [75]).

kinetic studies are done, Scheme 13 must be considered as a proposed, but kinetically unverified, picture-based mechanism.

3.2.2.2. Marre et al.'s studies of the formation of $Cu(0)_n$ on SiO_2 spheres. In 2006 and then in 2009, Marre et al. studied the formation of $Cu(0)_n/(SiO_2)_n$ (where $(SiO_2)_n$ are silica spheres) starting from $Cu(hfac)_2$ (where hfac = hexafluoroacetylacetonate) in supercritical CO_2/alcohol/H_2 mixtures [70,71] (Entries 3 and 4, Table 3). Ex situ TEM kinetic data were collected, monitoring the change in size of the $Cu(0)_n/(SiO_2)_n$ product with time. The authors proposed a model (Scheme 14) for the formation of $Cu(0)_n/(SiO_2)_n$ that accounts for the generation of nuclei due to precursor decomposition (i.e., "mode (1)" in Scheme 14), and then particle growth by coagulation and coalescence (i.e., "mode (2)" in Scheme 14), that is "homogeneous nucleation followed by heterogeneous growth", to quote the authors [71]. The authors claim that "The model allows the description of the particle size evolution by the variation of four variables: the nuclei volume concentration of mode 1 N_1, the particle volume concentration of mode 2 N_2, the

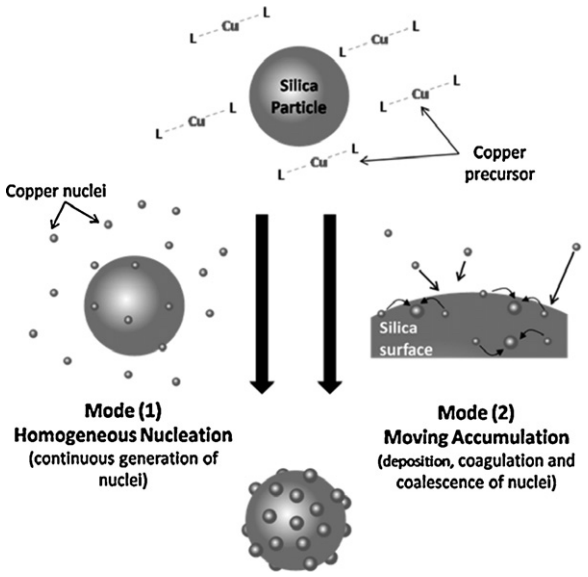

Scheme 14. A pictorial mechanism proposed by Marre et al. for the formation of $Cu(0)_n$ on SiO_2 spheres [71].

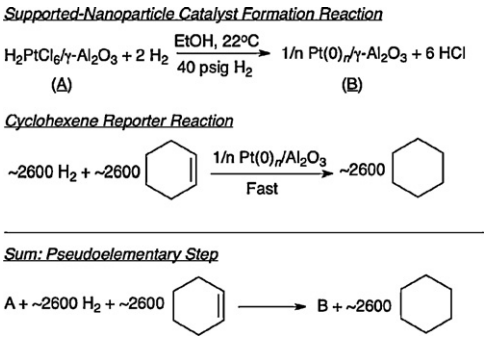

Scheme 15. The $H_2PtCl_6/\gamma\text{-}Al_2O_3$ to $Pt(0)_n/\gamma\text{-}Al_2O_3$ supported-nanoparticle formation reaction stoichiometry, cyclohexene reporter reaction and associated sum/pseudoelementary step [72].

volumetric concentration of the aggregates V_2, and the particle surface area concentration of mode 2 A_2". However and unfortunately, the proposed model was not fit to the observed experimental $Cu(0)_n$ diameter vs. residence time data (as it contains four parameters and only 3 data points were collected), see Fig. 11 in Ref. [71]. Nevertheless, in hand is valuable initial work identifying a good system worthy of additional, more detailed study. That said, several issues become apparent from a critical look at this system [70,71], vide infra, issues that those future studies will want to consider.

To start, the model employed by Marre et al. was originally developed by Choi and co-workers for the formation of aerosols [280] and assumes a monodisperse particle size distribution. However, the $-(SiO_2)_n$-supported $Cu(0)_n$ nanoparticles are not monodisperse; instead they show a size dispersion ranging from 29–55% based on the average and standard deviation of the diameters given in reference [71]. Second and perhaps most importantly (as examples elsewhere further detail [281,282][8]), an insidious disconnect exists here, as it does with all other picture- or word-only based mechanisms. Specifically, the words used (a) have no connection to balanced equations that rigorously and correctly define those words, and hence (b) no connection to the differential equation nor to the measured kinetic data. Those predicted differential (kinetic) equations are, of course, essential for testing and thereby supporting, or refuting, the proposed mechanistic equations and hence their associated words and pictures. The significance of this point is hard to over-emphasize. A look at the complex, confused literature of solid-state kinetics, where such disconnects between the words/concepts and the differential equations/kinetics is at present rampant and causing considerable confusion, frustration and unneeded complexity, will convince the skeptical reader that such disconnects are a very serious, insidious problem indeed [138–141,281]. Future work must strive to avoid the disconnect caused by picture- and word-only "mechanisms".

3.2.2.3. Studies of the formation of $Pt(0)_n$ on $\gamma\text{-}Al_2O_3$ and TiO_2. In 2009, studies were reported of the formation of $Pt(0)_n/\gamma\text{-}Al_2O_3$ starting from 1.96-wt% $H_2PtCl_6/\gamma\text{-}Al_2O_3$ in EtOH (and cyclohexene) under H_2 [72] (Table 3, Entry 5). The stoichiometry of the supported-nanoparticle formation (Scheme 15 (top reaction)), was confirmed via $pH_{apparent}$ measurements of the reaction solution post the supported-nanoparticle formation reaction (i.e., and in comparison to a sample containing 6 equivalents of authentic HCl plus the appropriate amount of $\gamma\text{-}Al_2O_3$). Those experiments yielded an identical pH within experimental error [72], thereby verifying the 6 HCl part of the stoichiometry in the top line of Scheme 15.

The kinetics of the $Pt(0)_n/\gamma\text{-}Al_2O_3$ supported-nanoparticle formation reaction (Fig. 8, diamonds), were well-fit to a 2-step mechanism (Fig. 8, line) consisting of slow continuous nucleation

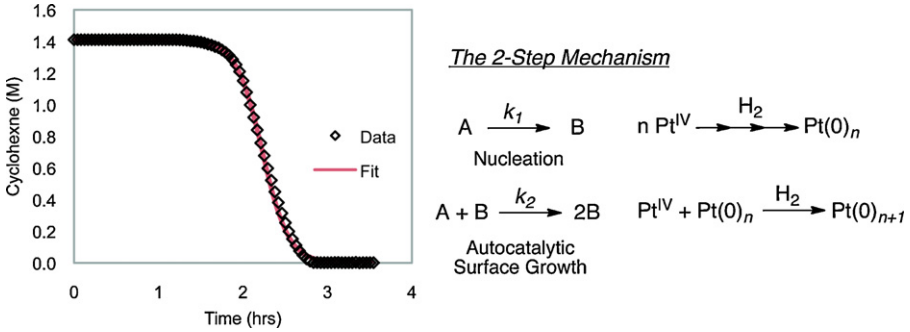

Fig. 8. $H_2PtCl_6/\gamma\text{-}Al_2O_3$ to $Pt(0)_n/\gamma\text{-}Al_2O_3$ supported-nanoparticle formation kinetics (black diamonds) in contact with EtOH, cyclohexene and H_2 (shown left) and fit to the 2-step mechanism (the line). Shown to the right is the 2-step mechanism used to fit the observed kinetic data [72]. (For the color version of this figure, the reader is referred to the web version of the article.)

Reprinted with permission from [72]. Copyright (2009) American Chemical Society.

($A \rightarrow B$, rate constant k_1), followed by fast autocatalytic surface growth ($A + B \rightarrow 2B$, rate constant k_2), a mechanism discovered for solution nanoparticle formation in 1997 [193] (Fig. 8 (right)). In these equations and in Fig. 8 A is $H_2PtCl_6/\gamma\text{-}Al_2O_3$ and B is $Pt(0)_n/\gamma\text{-}Al_2O_3$. The 2-step mechanism is a minimal, "Ockham's razor" [283], mechanism that has been widely used to extract average nucleation (k_1) and average autocatalytic surface growth (k_2) rate constants from the integrated analytical equation shown in Entry 5 of Table 3. Average rate constants for nucleation ($k_1 \approx 10^{-5.5(7)}\ h^{-1}$) and autocatalytic surface growth ($k_2 = 1.2(2) \times 10^4\ h^{-1}\ M^{-1}$) were obtained so long as a prestirring/pre-equilibration period of 2–7 h was employed when starting from the $H_2PtCl_6/\gamma\text{-}Al_2O_3$ precatalyst in contact with EtOH—very likely an equilibration period needed to control/minimize the "H_2PtCl_6"/$\gamma\text{-}Al_2O_3$ speciation. Without this preequilibration period the observed nucleation rate constant, k_1, varies by a range of $\sim 10^5$, as reflected in the varied supported-nanoparticle formation curves shown in Fig. 9.

Although the detailed reason(s) for the interesting $\sim 10^5$ range in k_1 remain(s) to be established, one very plausible hypothesis is that just noted: that a variable H_2PtCl_6 speciation, for the impregnation of H_2PtCl_6 onto metal oxides (recall Section 2.2.2.2), is responsible for the $\sim 10^5$ range in the rate constant for nucleation of the supported $Pt(0)_n$ nanoparticle synthesis when in contact with EtOH solvent. Noteworthy here is that $\sim 10^5$ range in k_1 directly causes a significant variation in the particle size (i.e., and in the size distribution) since k_1, k_2 and the starting $[H_2PtCl_6]_{initial}$ are three key factors in the equation governing nanoparticle size published for the 2-step mechanism [156].

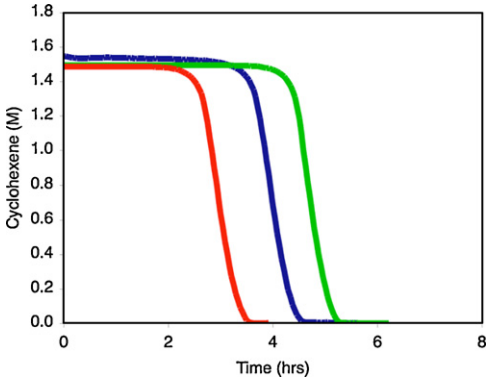

Fig. 9. Observed variation in the kinetics of the $Pt(0)_n/\gamma\text{-}Al_2O_3$ supported-nanoparticle heterogeneous catalyst formation system if a pre-equilibrium stirring period (in the EtOH reaction medium) is not employed. The resultant k_1 nucleation rate constant for these curves varies from $\sim 10^{-8}$ to $10^{-13}\ h^{-1}$, that is by a range of $\sim 10^5$ [72].

Reprinted with permission from [72]. Copyright (2009) American Chemical Society.

In order to fully appreciate how the $Pt(0)_n/\gamma\text{-}Al_2O_3$ supported-nanoparticle formation kinetic data were collected (e.g. Fig. 8), it is necessary to understand the indirect—but rapid, quantitative, and now well-precedented [190–193]—cyclohexene hydrogenation reporter reaction method that was employed. Experimentally, the supported-nanoparticle formation reaction was monitored by following the loss of H_2 pressure via a high pressure (±0.01 psig) computer-interfaced pressure transducer, which was then converted into cyclohexene loss via the experimentally verified (by ^1H NMR) [193] 1:1 H_2:cyclohexene stoichiometry. The cyclohexene reporter reaction (Scheme 15, middle reaction) takes advantage of the fact that the catalytic activity of the nanoparticle surface is proportional to the concentration of the active metal, B [193]. The sum/pseudo-elementary step [284–286][20] is given in Scheme 15 (bottom reaction), so that the overall reaction stoichiometry is then given by $-d[A]/dt/1 = -d[H_2]/dt/2600 = -d[\text{cyclohexene}]/dt/2600 = +d[B]/dt/1 = +d[\text{cyclohexane}]/dt/2600$. The power of the pseudoelementary step is that it allows one to measure the loss of H_2 or cyclohexene (or formation of cyclohexane) and relate that to the loss of A (or formation of B) by the above equation, for example $-d[H_2]/dt/2600 = -d[A]/dt/1$. An important point is that the use of the cyclohexene reporter reaction demands that the hydrogenation of cyclohexene be fast in comparison to the nanoparticle formation steps. This assumption is easily experimentally tested by changing the concentration of cyclohexene and plotting it vs. the H_2 uptake rate; the H_2 uptake rate should reach a regime where its a constant with increasing cyclohexene concentrations (i.e., should reach a limiting zero-order dependence on cyclohexene $[\text{cyclohexene}]^0$), as observed in Fig. 10, thereby verifying that cyclohexene reporter reaction is fast relative to the slower steps that one wants to measure kinetically (i.e., to $A \rightarrow B$ and $A + B \rightarrow 2B$ in the present example). In short, by following the loss of H_2 (or, equivalently the loss of cyclohexene), and as long as the cyclohexene reduction reaction is fast relative to the supported-nanoparticle formation reaction, one can measure the desired supported-nanoparticle nucleation, $A \rightarrow B$, and autocatalytic growth, $A + B \rightarrow 2B$, steps, all while employing the pseudoelementary-step stoichiometric relationships.

[20] A pseudoelementary step is the summation of one or more, slow elementary kinetic steps, to which one can add one or more fast steps, the overall (summed) pseudoelementary step by definition being establishable by determining the overall reaction stoichiometry. Noyes formally introduced the concept of the pseudoelementary step in the 1970s when studying complex oscillating reactions [284–286], although kineticists have used it and been aware of it probably long before Noyes' important labeling of the pseudoelementary step concept.

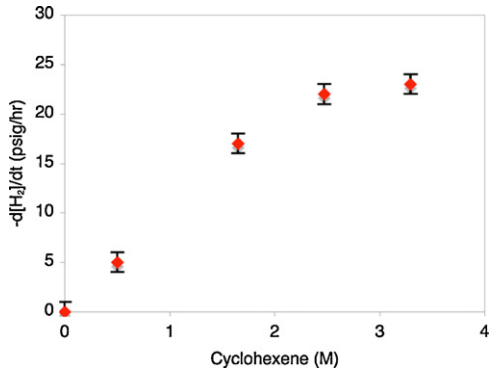

Fig. 10. A plot of the H_2 uptake rate ($-d[H_2]/dt$ extracted from the linear portion of the supported-nanoparticle formation reaction, Fig. 8) vs. the cyclohexene concentration. The kinetics reach a zero-order plateau in cyclohexene above 1.65 M [72].

Reprinted with permission from [72]. Copyright (2009) American Chemical Society.

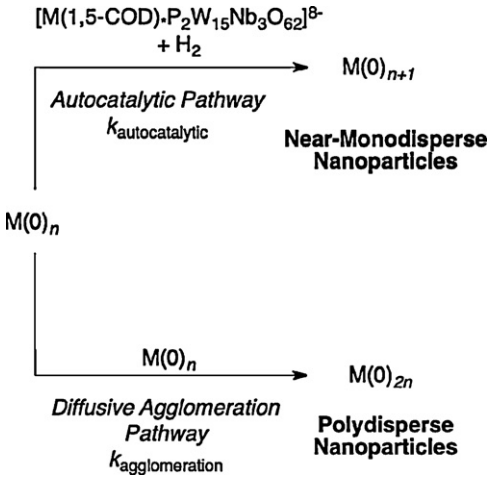

Scheme 16. The two, parallel nanoparticle growth pathways originally demonstrated during the formation, in solution, of polyoxoanion-stabilized $M(0)_n$ nanoparticles from a $[M(1,5\text{-COD})\bullet P_2W_{15}Nb_3O_{62}]^{8-}$ (M = Rh, Ir) precursor (i.e., $P_2W_{15}Nb_3O_{62}{}^{8-}$ is the polyoxoanion that was employed) [287]. As demonstrated elsewhere [287], insufficient H_2 (i.e., H_2 gas-to-solution MTL) yields polydisperse nanoparticles since diffusive agglomeration (bottom) kinetically outcompetes surface autocatalytic growth (top) when insufficient H_2 is present in solution.

In that 2009 study, also investigated was the conversion of a more heavily metal loaded, 5-wt% H_2PtCl_6/TiO_2 precatalyst to $Pt(0)_n/TiO_2$ in EtOH (and cyclohexene) under H_2 [72]. The observed kinetics are now linear (Fig. 11, red diamonds left), in dramatic contrast to the sigmoidal kinetics observed when starting from the lower loading, 2.0-wt% $H_2PtCl_6/\gamma\text{-}Al_2O_3$ precatalyst (Fig. 8). Interestingly and importantly, those linear kinetics are the same as Chupas et al. observed for their formation of 5-wt% H_2PtCl_6/TiO_2 to $Pt(0)_n/TiO_2$, but in their studies at the gas–solid interface [56]. Stirring rate, and H_2PtCl_6 weight percent control experiments in the 2009 study [72] revealed that the linear kinetic curves (for this gas–liquid–solid system) are due to H_2 gas-to-solution mass transfer limitations (MTL). Fig. 11 (left) demonstrates that when the stirring rate is increased from 600 to 1000 rpm, the cyclohexene uptake rate (or H_2 uptake) increases from 42.2 psig H_2/h to 66.8 psig H_2/h, that is a 66% increase leads to a 58% increase in the reaction rate, prima facie evidence for H_2 gas-to-solution MTL [287].

Further evidence consistent with the presence of H_2 gas-to-solution MTL is given by varying the weight percent of H_2PtCl_6 on TiO_2 and then plotting that vs. the measured H_2 uptake rate (Fig. 11 (right)). In short, the kinetics for the higher, 5-wt% H_2PtCl_6/TiO_2, are diffusion limited, and not chemical-reaction limited, kinetic evidence that is invaluable to knowing if the $Pt(0)_n$ nanoparticles are being synthesized under optimum conditions. Here they are not due to the established effects of H_2 gas-to-solution MTL that broaden the nanoparticle dispersion (vide infra) [287].

The negative affects of MTL conditions on nanoparticle formation (and syntheses) in solution have been demonstrated in the literature [287], Scheme 16—an example of one of the ≥8 mechanistic insights now available from kinetic and mechanistic studies of nanoparticle formation in solution [281]. Specifically, aggregation to polydisperse nanoparticles occurs under such MTL conditions (Scheme 16, bottom half) since that aggregation kinetically out competes the H_2-requiring surface autocatalytic growth that would otherwise yield near-monodisperse nanoparticles (i.e., ±≤15% [193]) at sufficient H_2 pressures (Scheme 16, top half).

However and importantly, by using the cyclohexene reporter reaction method it was possible to screen rapidly and find conditions that avoid the undesired linear (MTL) kinetic regime for the H_2PtCl_6/TiO_2 system [72]. Specifically, when a lower loading 0.99-wt% H_2PtCl_6/TiO_2 precatalyst was employed, the kinetics changed from linear to sigmoidal. While those 0.99-wt% H_2PtCl_6/TiO_2

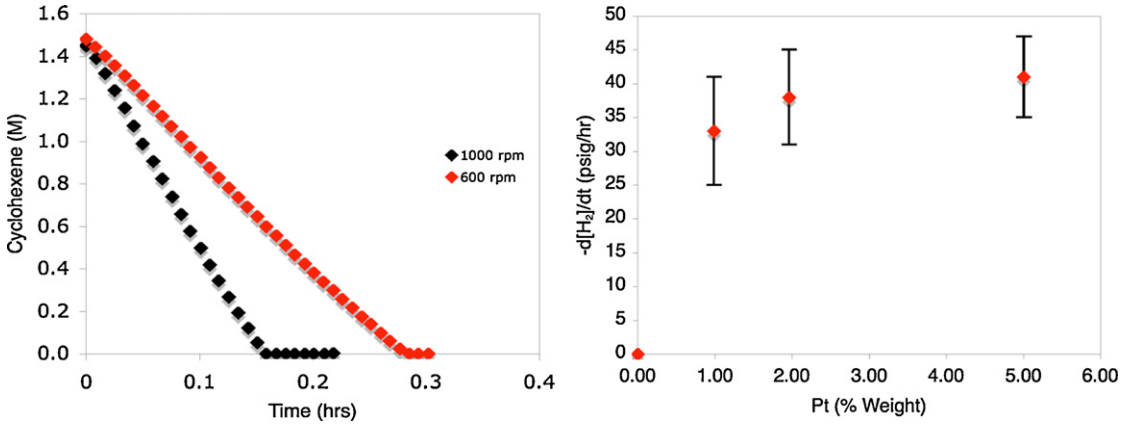

Fig. 11. Linear kinetics observed for the 5-wt% H_2PtCl_6/TiO_2 system in contact with EtOH, cyclohexene and H_2 at 600 and 1000 rpm [72] (shown left). The rate of H_2 loss as a function of the Pt-wt% demonstrates that the reaction approaches zero-order kinetics (i.e., approaches the H_2 gas-to-solution MTL regime) even by 2-wt% (right) [72].

Reprinted with permission from [72]. Copyright (2009) American Chemical Society.

kinetics were shown to still contain some MTL,[21] the lower catalyst loading is having the desired effect of moving away from the MTL-regime and into the desired chemical-reaction-limited regime.

In summary, kinetic and mechanistic studies of $H_2PtCl_6/\gamma\text{-}Al_2O_3$ in contact with EtOH solvent and using the cyclohexene/H_2 to cyclohexane reporter reaction method have demonstrated: (i) a balanced reaction stoichiometry; and (ii) sigmoidal kinetic curves which can be fit by a 2-step, slow, continuous nucleation and then fast autocatalytic surface growth mechanism. Hence, the words/concepts of "slow, continuous nucleation" and then "fast autocatalytic surface growth" [193] can be used rigorously and with confidence for this system.[8] This is a non-trivial point in comparison to literature word- or picture-based mechanisms. Also demonstrated for the H_2PtCl_6/TiO_2 system were: (iii) H_2 gas-to-solution MTL kinetics, from which polydisperse nanoparticles to form as a result of those MTL effects, and (iv) conditions that largely avoid such undesirable MTL effects. Perhaps especially important, also reported were (v) that there is a $\sim 10^5$ range in k_1 for the $H_2PtCl_6/\gamma\text{-}Al_2O_3$ system unless one pre-equilibrates the system with the EtOH solvent, and (vi) the suggestion that the H_2PtCl_6 speciation is the underlying cause of the $\sim 10^5$ range in k_1, an important hypothesis that remains to be further tested and thereby supported or refuted.

3.2.2.4. Studies of the formation for the conversion of Ir(1,5-COD)Cl/γ-Al2O3 to Ir(0)~900/γ-Al2O3: development of a prototype system in contact with solution. The speciation issues in the classic H_2PtCl_6/support system [72] lead to the definition, then development, of a so-called "prototype" system for the study of the synthesis and kinetics and mechanism of the formation of supported-nanoparticles in contact with solution. Specifically, 8 criteria were defined [74] in which a prototype system: (i) should start from a compositionally and structurally well-defined supported precatalyst; (ii) should be in contact with solution and formed under low temperature conditions; and (iii) should contain an establishable, balanced stoichiometry for a supported-nanoparticle formation reaction, a reaction that should also lead to a well-characterized supported-nanoparticle catalyst. In addition, a prototype system; (iv) should yield an active and long-lived catalyst, so that (v) the desired/necessary kinetic and mechanistic studies are worth the effort. The prototype system (vi) should also yield reproducible and quantitative kinetic data, so that quantitative conclusions and mechanistic insights can be drawn. Moreover and ideally, comparison should be possible to a kinetically and mechanistically well-studied solution nanoparticle formation system [193,288], with the goal of obtaining new insights that such a little-precedented comparison might reveal. Once that prototype system is in hand, one would also like to (viii) systematically vary key synthetic variables (such as the support, the solvent, the metal precursor and other desired additives or "promoters") to reveal their affects on the supported-nanoparticle formation reaction in contact with solution. Other attributes of a prototype system are surely possible if not desirable, but the above 8 attributes were the initial goal [74].

Hence, in 2010 and 2011 papers, studies were reported regarding the formation of a (as defined) prototype Ir(1,5-COD)Cl/γ-Al_2O_3

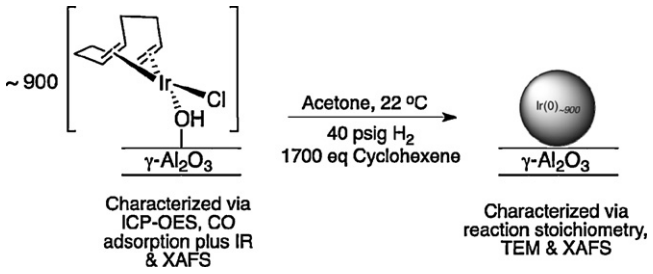

Scheme 17. The recently developed [74] Ir(1,5-COD)Cl/γ-Al_2O_3 to Ir(0)~900/γ-Al_2O_3 supported-nanoparticle formation system in contact with solution.

to Ir(0)~900/γ-Al_2O_3 supported-nanoparticle catalyst formation system shown in Scheme 17 [74,75] (Table 3, Entries 7 and 8). The Ir(1,5-COD)Cl/γ-Al_2O_3 to Ir(0)~900/γ-Al_2O_3 supported-nanoparticle formation system in contact with solution satisfies the first 7 of 8 prototype criteria as defined above. The speciation-controlled Ir(1,5-COD)Cl/γ-Al_2O_3 precatalyst was thoroughly characterized via inductively coupled plasma optical emission spectroscopy, CO trapping plus IR, and XAFS spectroscopies. The Ir(0)~900/γ-Al_2O_3 product was formed in contact with acetone, cyclohexene and H_2, and then fully characterized via reaction stoichiometry (confirmed via cyclooctane evolution and H_2 uptake measurements), TEM and XAFS spectroscopy revealing a near-monodispere [215], non-aggregated 2.9 ± 0.4 nm Ir(0)~900/γ-Al_2O_3 catalyst (Fig. 12). The resultant Ir(0)~900/γ-Al_2O_3 is a highly active (turnover frequency of 8200 turnover/h) and long-lived (≥220,000 total turnovers) cyclohexene hydrogenation catalyst [74] ensuring that the subsequent, time-consuming kinetic and mechanistic studies were worth the effort.

The observed Ir(0)~900/γ-Al_2O_3 supported-nanoparticle formation kinetics (Fig. 13, left), again monitored via the cyclohexene reporter reaction (analogous to the one shown in Scheme 15), are sigmoidal (Fig. 13). Those kinetics are well-fit to the 2-step mechanism of slow continuous nucleation ($A \rightarrow B$, rate constant k_1), followed by fast autocatalytic surface growth ($A + B \rightarrow 2B$, rate constant k_2), where in this case A is the Ir(1,5-COD)Cl/γ-Al_2O_3 precatalyst and B is the growing $Ir(0)_n$ nanoparticle surface [74]. The resultant, well-defined rate constants are $k_1 = 1.5(1.1) \times 10^{-3}\ h^{-1}$ and $k_2 = 1.6(2) \times 10^4\ h^{-1}\ M^{-1}$ for nucleation and autocatalytic surface growth, respectively—note that control over the Ir(1,5-COD)Cl/γ-Al_2O_3 speciation has allowed reproducible k_1 and k_2 rate constants along with formation of a near monodisperse (i.e., ±≤15%) 2.9 ± 0.4 nm Ir(0)~900/γ-Al_2O_3 supported-nanoparticle catalyst.

The choice of the Ir(1,5-COD)Cl/γ-Al_2O_3 precatalyst allows for an additional, valuable kinetic monitoring method performed as a control. By using gas–liquid-chromatography (GLC), the authors directly monitored the cyclooctane evolution kinetics (i.e., the loss of A, Ir(1,5-COD)Cl, by the formation of cyclooctane, the hydrogenated product of the starting 1,5-cyclooctadiene ligand) (Fig. 13 (right)). Importantly, the nucleation ($k_{1GLC} = 1.2(2) \times 10^{-3}\ h^{-1}$) and autocatalytic surface growth ($k_{2GLC} = 1.2(2) \times 10^4\ h^{-1}\ M^{-1}$) rate constants obtained by the more direct, but slow and imprecise, GLC monitoring method provides independent verification of the kinetics obtained by the fast and precise, but indirect, cyclohexene reporter reaction method ($k_1 = 1.5(1.1) \times 10^{-3}\ h^{-1}$ and $k_2 = 1.6(2) \times 10^4\ h^{-1}\ M^{-1}$). The comparison of the GLC vs. H_2-pressure transducer obtained kinetics also experimentally and independently verifies the $-d[A]/dt/1 = -d[H_2]/dt/1700$ relationship inherent to the reporter reaction with its excess, 1700 equivalents of cyclohexene vs. the 1 equivalent of A (where A = the Ir(1,5-COD)Cl/γ-Al_2O_3 precatalyst) [74]. The results make apparent the ease, precision, power and validity of the of the cyclohexene reporter reaction method for following the kinetics of

[21] The observation that the lower 0.99-wt% H_2PtCl_6 loading *on* TiO_2 still has MTL effects, despite being at 2-fold lower loading than the γ-Al_2O_3 case, shows (a) the significant effect of the support on the catalyst formation kinetics, and (b) argues for different speciation on, or in the presence of, these two supports (with a more active species toward Pt(0) formation being present on TiO_2). Such support effects have also been observed in the gas-solid supported-nanoparticle formation literature [32,37,42], but their detailed origin remains obscure.

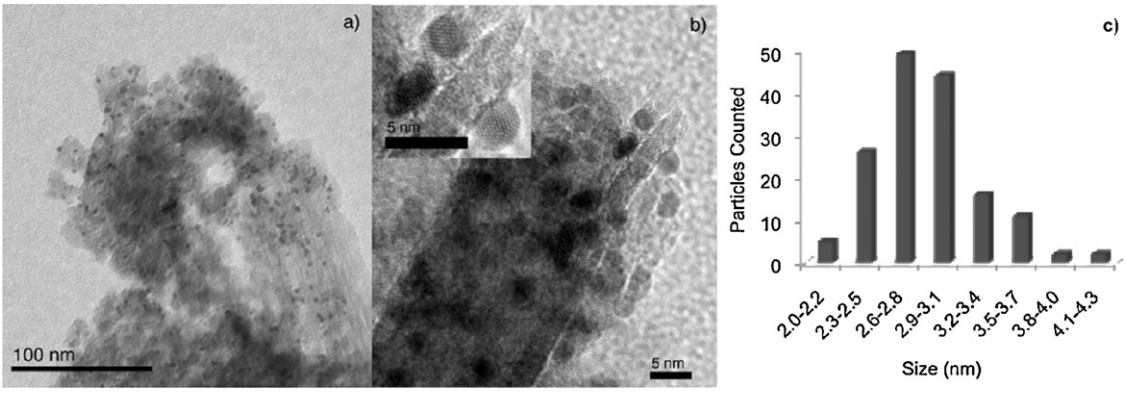

Fig. 12. TEM imaging and particle size histogram of the prototype $Ir(0)_{\sim 900}/\gamma\text{-}Al_2O_3$ supported-nanoparticle catalyst showing 2.9 ± 0.4 nm, and, hence a near-monodisperse size distribution [74]. (a) A large-area view (scale bar 100 nm) reveals that the nanoparticles are well-dispersed on the support. (b) A close-up view (scale bar 5 nm) reveals that the supported-nanoparticles are crystalline. (c) The associated particle size histogram.
Reprinted with permission from [74]. Copyright (2010) American Chemical Society.

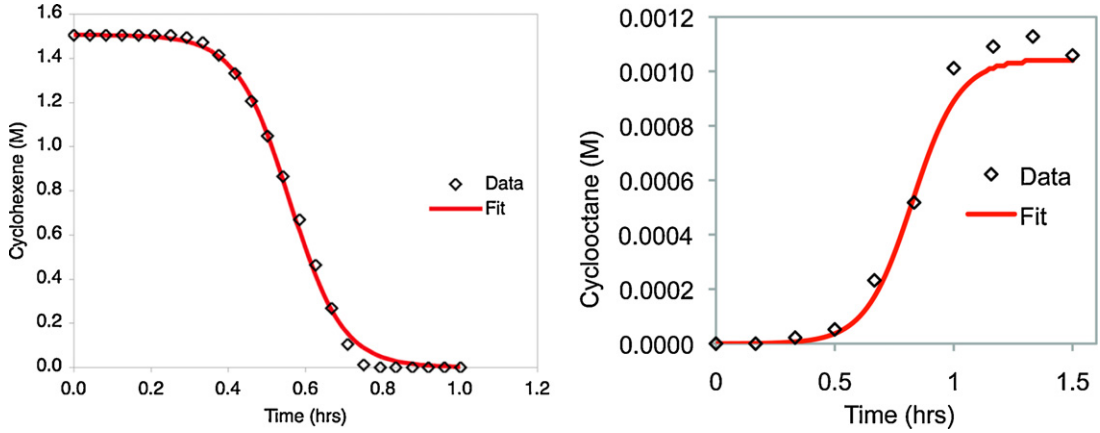

Fig. 13. The sigmoidal kinetics obtained via the cyclohexene reporter reaction method and fit to the 2-step mechanism (left), plus the control of directly monitoring the evolution of cyclooctane via GLC (right) all for the $Ir(1,5\text{-}COD)Cl/\gamma\text{-}Al_2O_3$ to $Ir(0)_{\sim 900}/\gamma\text{-}Al_2O_3$ supported-nanoparticle formation reaction in contact with solution. The k_1 and k_2 rate constants obtained independently from the two kinetic monitoring methods agree within experimental error [74] (i.e., and after correction for the pseudoelementary step derived $-d[A]/dt/1 = -d[H_2]/dt/1700$ stoichiometry), nicely confirming each method and the underlying kinetic derivations and pseudoelementary step method.
Reprinted with permission from [74]. Copyright (2010) American Chemical Society.

supported-nanoparticle formation in contact with solution, at least in such favorable cases and when the proper $[cyclohexene]^0$ controls are performed [74,193].

In a follow up study [75], the authors addressed the important question of whether the nucleation and growth steps occur primarily in solution, on the support, or possibly in both phases for one or more of the $Ir(0)_{\sim 900}/\gamma\text{-}Al_2O_3$ catalyst formation steps. That is, what is the intimate kinetic mechanism for this prototype system formed in contact with solution? The possible purely solid-oxide-based, purely solution-based or mixed solution-plus-solid nucleation and growth alternative mechanistic pathways are shown in Scheme 18. The bolded pathway shows the mixed solution-plus-solid mechanism that was uncovered by the kinetic and other mechanistic studies [75], vide infra.

In the kinetic treatment, and the expressions provided next (and as originally derived elsewhere [75]), the $Ir(1,5\text{-}COD)Cl/\gamma\text{-}Al_2O_3$ precatalyst (abbreviated $[Ir^I/Al_2O_3]_{sus}$) and $\gamma\text{-}Al_2O_3$ (abbreviated $[Al_2O_3]_{sus}$) were necessarily approximated as being "homogeneously suspended in solution",[22] as depicted by the "sus"

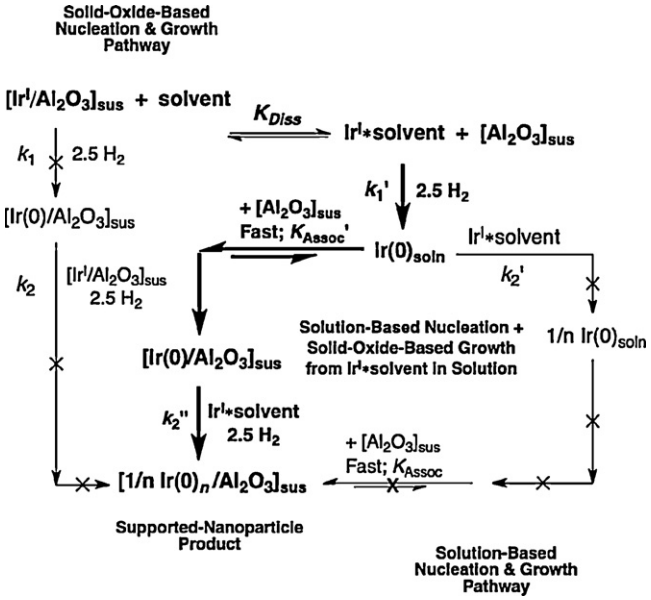

Scheme 18. The a priori, plausible solid-oxide only (left), solution-only (right), and mixed (bolded; the kinetically observed) pathways for conversion of $Ir(1,5\text{-}COD)Cl/\gamma\text{-}Al_2O_3$ to $Ir(0)_{\sim 900}/\gamma\text{-}Al_2O_3$ in contact with solution [75].

[22] More specifically, the hypothetical "concentrations" of active "Ir(1,5-COD)Cl" binding sites of the suspended $\gamma\text{-}Al_2O_3$ were treated as if they increase linearly when in contact with solution (or, really, with the amount of solvent-exposed $\gamma\text{-}Al_2O_3$ surface area) [75].

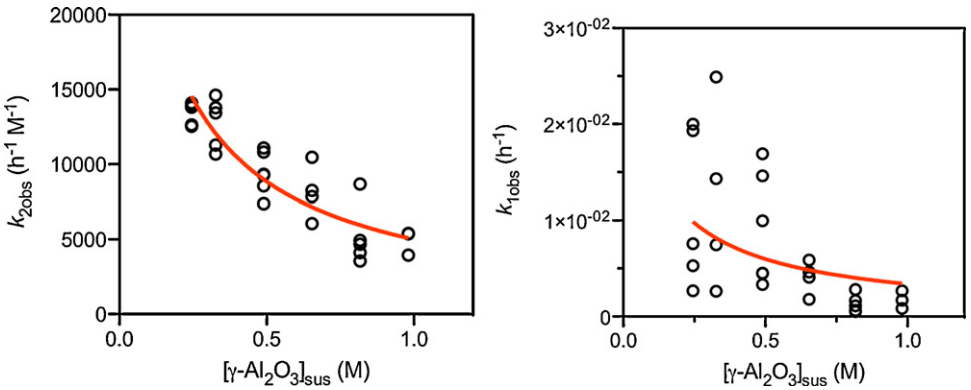

Fig. 14. Dependence of the k_{2obs} (left black circles) and k_{1obs} (right, circles) rate constants on the [γ-Al_2O_3]$_{sus}$ "concentration". Also shown are the fits (the lines) to Eqs. (11) and (10), respectively [75]. (For the color version of this figure, the reader is referred to the web version of the article.)
Reprinted with permission from [75]. Copyright (2011) American Chemical Society.

subscripts, and approximation that proved to work well in those studies. The bold mechanism in Scheme 18 consists of Ir(1,5-COD)Cl(solvent) dissociation from the γ-Al_2O_3 support (i.e., from Ir(1,5-COD)Cl/γ-Al_2O_3), then solution-based nucleation from that dissociated Ir(1,5-COD)Cl(solvent) species, subsequent fast Ir(0)$_n$ nanoparticle capture by γ-Al_2O_3 and then solid-oxide-based nanoparticle growth by Ir(0)$_n$/γ-Al_2O_3 with Ir(1,5-COD)Cl(solvent). For that bold pathway, the relevant kinetic equations can be derived by starting from the 2-step mechanism (Eq. (6)):

$$\frac{d[Ir^I/Al_2O_3]_{sus}}{dt} = k'_1\,[Ir^I * solvent]_t + k''_2[Ir^I * solvent]_t[Ir(0)_n/Al_2O_3]_{sus,t} \quad (6)$$

In Eq. (6) and the equations that follow, Ir^I*solvent is the dissociated complex, Ir(1,5-COD)Cl(solvent), Ir^I/Al_2O_3 is Ir(1,5-COD)Cl/γ-Al_2O_3 precatalyst, the subscript "*i*" represents initial concentrations, while the subscript "*t*" denotes each species as a function of time. Solving the dissociative equilibrium equation (K_{Diss}) (Eq. (7)) for [Ir^I*solvent]$_t$ followed by subsequent substitution in the mass balance equation (Eq. (8)) are key steps in the derivation.

$$K_{Diss} = \frac{[Ir^I * solvent]_t[Al_2O_3]_{sus,t}}{[Ir^I/Al_2O_3]_{sus,t}[solvent]_t} \quad (7)$$

$$[Ir^I/Al_2O_3]_{sus,i} = [Ir^I/Al_2O_3]_{sus,t} + [Ir^I * solvent]_t \quad (8)$$

Substitution of the resultant [Ir^I/Al_2O_3]$_{sus}$ equation back into Eq. (6) yields Eq. (9), where the resultant rate constants are given by Eqs. (10) and (11), respectively.

$$-\frac{d[Ir^I/Al_2O_3]_{sus}}{dt} = k_{1obs}[Ir^I/Al_2O_3]_{sus,i} + k_{2obs}[Ir^I/Al_2O_3]_{sus,i}[Ir(0)_n/Al_2O_3]_{sus,t} \quad (9)$$

$$k_{1obs} = \frac{k'_1K_{Diss}[solvent]_t}{[Al_2O_3]_{sus,t} + K_{Diss}[solvent]_t} \quad (10)$$

$$k_{2obs} = \frac{k''_2K_{Diss}[solvent]_t}{[Al_2O_3]_{sus,t} + K_{Diss}[solvent]_t} \quad (11)$$

The mechanism in Scheme 18 (bold), along with Eqs. (10) and (11), predict that both the γ-Al_2O_3 and solvent "concentrations" should affect the nucleation and growth rate constants.

To start, the effects of the suspended γ-Al_2O_3 on the Ir(0)$_{\sim 900}$/γ-Al_2O_3 nucleation and growth kinetics [75] were investigated (Fig. 14). Consistent with the mechanism in Scheme 18 (bold) both k_{2obs} and k_{1obs} qualitatively decrease with increasing γ-Al_2O_3 (black circles). That trend is explained by the increased γ-Al_2O_3 shifting the K_{Diss} equilibrium in Scheme 18 to the left, resulting in less Ir(1,5-COD)Cl(solvent) in solution, and a corresponding decrease in both k_{2obs} and k_{1obs}. Importantly, Eq. (11) could be used to quantitatively fit the k_{2obs} vs. γ-Al_2O_3 data shown in Fig. 14 (the line, left), yielding values of $k_2'' = 4(1) \times 10^{-4}$ h^{-1} M^{-1} and $K_{Diss} = 1.3(6) \times 10^{-2}$. The K_{Diss} equilibrium was independently verified by hydrogenating the dissociated/equilibrated Ir(1,5-COD)Cl(solvent) in solution and quantifying the amount of cyclooctane in solution via GLC. In addition, constraining $K_{Diss} = 1.3(6) \times 10^{-2}$, Eq. (10) could "roughly" account for the shape of the k_{1obs} vs. γ-Al_2O_3 data also shown in Fig. 14 (the line, right). Note that the scatter of $\sim 10^1$ in the k_{1obs} data is as expected; nucleation rate constants are known to have a scatter of $\sim 10^{1.2}$ in the best studied nanoparticle formation systems to date (e.g., the solution synthesis of Ir(0)$_{\sim 300}$ nanoparticles from a single species Ir(1,5-COD)·$P_2W_{15}Nb_3O_{62}^{8-}$ polyoxoanion precursor [289]) for reasons that are partially understood [193,288]. The steeper rise of the data vs. the computed (fit) curve in the right-hand, k_1 vs. [γ-Al_2O_3]$_{sus}$ plot in Fig. 14 is suggestive of bimolecular nucleation, A + A → 2B, a point under investigation [290].

In order to investigate the affects of the acetone/solvent "concentration" on the Ir(1,5-COD)Cl/γ-Al_2O_3 to Ir(0)$_n$/γ-Al_2O_3 kinetics, a mixed solvent system of cyclohexane plus acetone was used [75]. One key difference is that [Ir(1,5-COD)Cl]$_2$ was now the dominant species observable in solution via UV–vis spectroscopy. While a slightly modified mechanism, and forms of Eqs. (10) and (11), were derived in that original publication [75], the qualitative results are easily explainable in terms of Scheme 18 and Eqs. (10) and (11). The k_{2obs} and k_{1obs} vs. [acetone] data are shown in Fig. 15; qualitatively both k_{2obs} and k_{1obs} increase with increasing acetone concentration as the mechanism back in Scheme 18 predicts. Shifting the dissociative equilibrium in Scheme 18 to the right results in more Ir(1,5-COD)Cl(solvent) (really [Ir(1,5-COD)Cl]$_2$ in this mixed solvent case) in solution and a concomitant increase in both k_{2obs} and k_{1obs}. Again, the general form of Eq. (11) could be used to quantitatively fit the k_{2obs} vs. [acetone] data. Once the K_{Diss} equilibrium for the mixed solvent system was determined, the k_{1obs} vs. [acetone] data could also be accounted for at least semiquantitatively (i.e., and in light of the inherent experimental error in the data in Fig. 15, right). The higher data points above the curve-fit line in the right hand k_{1obs} vs. [acetone]^1 plot are, again, suggestive of bimolecular nucleation [290].

The Ir(1,5-COD)Cl/γ-Al_2O_3 to Ir(0)$_{\sim 900}$/γ-Al_2O_3 supported-nanoparticle formation nucleation and growth rate constants also

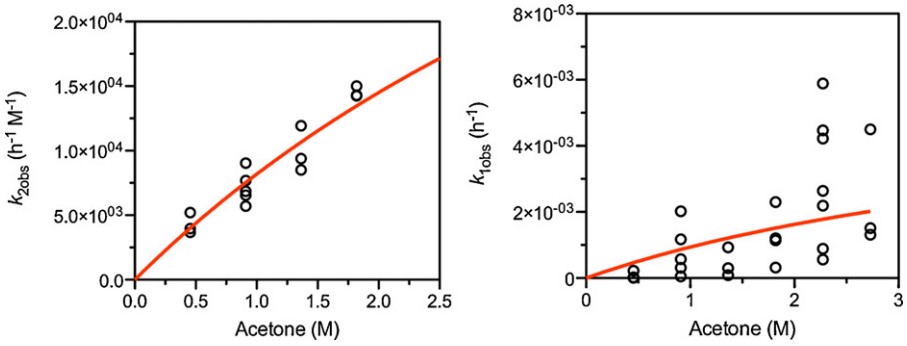

Fig. 15. Dependence of the k_{2obs} (left, circles) and k_{1obs} (right, circles) rate constants on the [acetone] "concentration". Also shown are the fits (the lines) to equations that have the same general form as Eqs. (11) and (10), respectively [75]. (For the color version of this figure, the reader is referred to the web version of the article.) Reprinted with permission from [75]. Copyright (2011) American Chemical Society.

have a general solvent dependence in acetone, propylene carbonate, CH_2Cl_2 and cyclohexane: k_{1obs} varies by ~3000-fold and k_{2obs} varies by ~70-fold. Finally, that solvent variation-, γ-Al_2O_3- and acetone-dependent kinetic data, along with UV–vis spectroscopic and GLC data could also be used to rule out the all-heterogeneous (solid-oxide-based) and all-homogeneous (solution-based) nucleation and growth mechanisms also shown in Scheme 18 (and as detailed in the original paper [75]).

Importantly, these studies suggest that the ≥8 available synthetic insights from the soluble, ligand-stabilized, nanoparticle formation literature should be transferable to the syntheses of supported-nanoparticle heterogeneous catalysts. Those insights include [281]: (i) that autocatalysis separates nucleation and growth in time, which in turn is why near-monodisperse (≤±15%) size distributions of typically "magic-number" sized [157] supported-nanoparticles are formed; (ii) that rational size control is possible via a recently developed nanoparticle size vs. time equation that relates k_1, k_2 and the precursor ($[A]_0$) concentration to the final nanoparticle average size [156]; (iii) that additional size control is possible via olefin or other ligand additives [288]; (iv) that rational seeded-growth methods are precedented by the surface autocatalytic growth step, including the rational syntheses of all possible geometric isomers of multimetallic "nano-onions" [157]; (v) that rational catalyst shape control is predicted, via preselected ligands attaching to the growing nanoparticle faces, thereby preventing autocatalytic surface growth at those facets [232–235]; (vi) that the negative effects of H_2 gas-to-solution mass-transfer limitations (MTL) in nanoparticle syntheses are expected (vide supra), along with insights into how to avoid such MTL effects [287]; (vii) that specific, nanoparticle lattice-matching ligands can provide additional nanoparticle stability if desired [223,291]; and finally (viii) that nanoparticle size-dependent surface metal-to-ligand bond energies exist in which the larger nanoparticles have weaker M_n–L bonds—plus all that very important, arguably very general, preliminary finding implies for catalysis [191,192].

3.2.3. Conclusions

The above survey (i.e., Table 3) of the kinetic and mechanistic studies of supported-nanoparticle formation in liquid–solid systems makes clear that such studies have occurred only 1/5th as frequent as studies of gas–solid systems. While word- and picture-based mechanisms dominated the earlier literature [69–71], there is a clear trend towards more rigorous, chemical reaction-based, supported-nanoparticle formation mechanisms in the liquid–solid based nanoparticle formation systems [72,74,75]. A 2-step mechanism consisting of slow, continuous nucleation A → B (rate constant k_1) followed by fast autocatalytic surface growth, A + B → 2B (rate constant k_2), has been shown to quantitatively account for both $Pt(0)_n$/γ-Al_2O_3 and $Ir(0)_n$/γ-Al_2O_3 supported-nanoparticle formation in contact with solution [72,74,75]. Also demonstrated is that nucleation occurs in solution from Ir(1,5-COD)Cl(solvent) for the Ir(1,5-COD)Cl/γ-Al_2O_3 to $Ir(0)_{\sim 900}$/γ-Al_2O_3 system in acetone solvent, the one case examined to date [75]. One expects the finding of solution-based nucleation to be more general for other coordinatively saturated (e.g., d^8 square planar), or high-valent (e.g., Ir(III), Rh(III), Au(III)), supported organometallic species that do not have facile reduction mechanisms to $M(0)_n$ under H_2 (i.e., and while on the support) [292]. Additionally, diffusion-based mechanisms (more specifically H_2 gas-to-solution MTL) were also revealed for $Pt(0)_n/TiO_2$ supported-nanoparticle formation from 5-wt% H_2PtCl_6/TiO_2 [72]; hence, care must be taken to minimize such effects even when employing such liquid–solid systems. Finally, a very important insight for future studies—one that makes physical sense in hindsight—is that diffusion limitations present in gas–solid catalyst formation systems can be overcome in favorable cases by going to a liquid–solid system. This potential advantage, argues, by itself, for much greater investigation of liquid–solid systems.

The future appears bright for synthetic, as well as kinetic and mechanistic studies of supported-nanoparticle formation in solution—catalysts ideally synthesized from speciation-controlled, supported organometallics and other single-species precatalysts. In those studies it will continue to be important to establish regimes where chemical-reaction-based kinetics are occurring, rather than diffusion-limited conditions. Establishing fully the supported-nanoparticle formation stoichiometry and resultant products will continue to be important stepping stones, as those stoichiometries must be the sum of the proposed mechanistic steps. Overall, the results suggest that synthetic and mechanistic insights, from the modern revolution in nanoparticle syntheses and study in solution, can now begin to be transferred to the syntheses of improved, size, shape and surface-composition controlled supported-nanoparticles and their catalysis.

4. Summary

Key points from the introduction section include:

- Key catalytic properties—such as selectivity, activity and lifetime—of supported-nanoparticle catalysts depend of course on the size, structure and composition of the supported nanoparticles.
- Unfortunately, rational, mechanistically guided syntheses of the desired size, structure and compositionally controlled supported-nanoparticle catalysts are generally still lacking.

- One major reason for this gap, despite the technological and commercial importance of supported-nanoparticle catalysts, is the present poor understanding of the mechanisms that govern supported-nanoparticle formation.

Key points from the fundamental background information at the gas–solid interface include:

- Methods such as XAFS and total high-energy X-ray scattering plus PDF analysis are direct, powerful physical methods capable of following supported-nanoparticle formation in real time.
- However, and despite the emergence and use of such powerful spectroscopic methods, additional, more routine complimentary kinetic monitoring methods are needed to screen systems and to ensure that only the most important and well-defined systems are subject to the more expensive and time-consuming synchrotron X-ray methods mentioned above. Restated, there is a need in the future to couple cheap, quick and easy (albeit sometimes indirect) methods with the more expensive, slower (but more direct and thereby powerful) reaction product and kinetic monitoring methods.
- The complex nature of the mechanisms of formation of supported-nanoparticles will demand the use of multiple, complimentary physical methods (e.g., XAFS plus total high-energy X-ray scattering with PDF analysis).

Key points from the kinetic and mechanistic studies at the gas–solid interface include:

- The $M(NH_3)_4^{2+}$ ($M = Pt^{2+}$, Pd^{2+}) H_2PtCl_6, $Ag(NO_3)$, and supported-organometallic systems provide a solid foundation of work upon which to build. However, much remains to be done including studies that, at a minimum, rigorously demonstrate the following: (i) the supported-precatalyst composition and structure—that is, the precise precatalyst speciation present, (ii) the supported-nanoparticle products, and (iii) the overall balanced stoichiometry of the nanoparticle formation reaction.
- Control over the supported-precatalyst speciation is particularly crucial as the supported-nanoparticle formation kinetics are governed by the rates of evolution of those species (e.g., their nucleation (k_1) and growth (k_2) rate constants). Supported-organometallic precatalysts offer one good, precedented, and arguably more broadly applicable way to overcome and control the precatalyst speciation problem.
- Once speciation-controlled precatalysts are in hand, diffusional and other unwanted processes need to be looked for, and then eliminated, when present so that chemical-reaction-based kinetic regimes can studied en route to the synthesis of the desired, more active, more selective, longer-lived and precisely weakly-ligated supported-nanoparticle catalysts.
- The finding of diffusion-limited processes in supported-nanoparticle formation of gas–solid systems is arguably a major limitation at present in those systems—an important finding from this review. It is crucial, therefore, to find conditions which at least limit, if not eliminate, such diffusion-controlled limitations in gas–solid supported-nanoparticle formation systems.
- Chemical-reaction-based mechanisms (rather than the currently dominant word- and picture-based), plus disproof of multiple alternative mechanisms (hypotheses) en route to a thereby better supported mechanism, are needed if the synthetic and mechanistic knowledge of supported-nanoparticle formation reactions is to advance smoothly, more quickly and reliably.
- There is a need to bridge the synthetic and mechanistic knowledge of supported-nanoparticle formation from the systems and studies reviewed herein, with knowledge from the UHV community, as well as with the knowledge now available from soluble ligand-stabilized nanoparticle formation in solution. There is also a need to bridge the above three areas with the wealth of precise knowledge of reactions and their mechanisms available from the organometallic community [25,26].

Key points from the fundamental background information in liquid–solid systems include:

- Synthesizing supported-nanoparticles via liquid–solid systems is an attractive, emerging area, one where the synthetic and mechanistic insights, from the modern revolution in nanoparticle synthetic and mechanistic studies in solution, can probably be transferred to the synthesis of supported-nanoparticle catalysts. Bridging the "pressure", "temperature", "materials" and "no solvent vs. solvent" gaps between those areas, as well as bridging and melding the "concept and associated nomenclature" gaps, between these areas promises to be a formidable – but key, important – challenge.
- Direct, *in operando* techniques for following the kinetics of supported-nanoparticle formation need to be emphasized in the future.

Key points from the kinetic and mechanistic studies in liquid–solid systems include:

- In terms of volume, kinetic and mechanistic studies for liquid–solid systems are presently 1/5th as common as the more often studied gas–solid systems—indicating that a wide-open opportunity for additional studies is present for liquid–solid systems.
- Despite the lower volume of work to date, good initial headway has been made into understanding supported-nanoparticle formation reactions and their underlying mechanism(s) in liquid–solid systems. In particular, the overall kinetics in several systems can be fit by a chemical-reaction-based mechanism consisting of slow, continuous, nucleation ($A \rightarrow B$, rate constant k_1) followed by fast autocatalytic surface growth ($A + B \rightarrow 2B$, rate constant k_2). A nanoparticle size vs. time equation is also available for that 2-step mechanism and in terms of k_1, k_2 and $[A]_0$ [156].
- In one case, an as-defined prototype system, Ir(1,5-COD)Cl/γ-Al_2O_3, has been prepared and shown to evolve to a well-defined, weakly-ligated, highly catalytically active, $Ir(0)_{\sim 900}$/γ-Al_2O_3 supported-nanoparticle catalyst via a demonstrated, balanced reaction stoichiometry.
- In the Ir(1,5-COD)Cl/γ-Al_2O_3 to $Ir(0)_{\sim 900}$/γ-Al_2O_3 system in contact with acetone solution, kinetic and mechanistic studies demonstrate that nucleation occurs in solution from Ir(1,5-COD)Cl(solvent) dissociated from the γ-Al_2O_3 support, followed by a fast $Ir(0)_n$ nanoparticle capture step by the γ-Al_2O_3 support, and then subsequent support-based nanoparticle growth between $Ir(0)_n$/γ-Al_2O_3 plus Ir(1,5-COD)Cl(solvent) from solution.

Overall, it is clear that kinetic and mechanistic insights into supported-nanoparticle heterogeneous catalyst formation greatly lags behind both the importance, as well as the prior preparative chemistry, of these practical, industrially relevant catalysts. However, a convergence appears to be emerging between the knowledge of solution nanoparticle syntheses, mechanistic studies of nanoparticle formation in solution, improved speciation-controlled synthesis of supported precatalysts, plus the use of powerful physical methods (such as XAFS and the total high-energy X-ray scattering and PDF analysis). Complimentary, quicker and easier, but less direct methods for following nanoparticle formation reactions are also finding use. A synergism of these subareas is beginning to occur and is strongly encouraged. A combination and melding of the knowledge of the heterogeneous catalysts, UHV, solution nanoparticle and organometallic communities is needed and, therefore, is an important, challenging goal.

Despite the above advances, much remains to be done to achieve the lofty goal of synthesizing the next generation of size, size

dispersion, shape and surface-composition-controlled supported-nanoparticle heterogeneous catalysts. It is hoped the present review of the current state of knowledge, and additional research needs, will help fuel the needed, synergistic efforts.

Note added in proof

Two relevant papers have been published since submission of this review. The first study is a third publication from Chupas, Chapman and co-workers [293] in which those authors used total high-energy X-ray scattering, plus PDF analysis, to monitor the formation of $Ag(0)_n$ species supported on the zeolite Mordenite (MOR) from a Ag^+/MOR precatalyst under H_2 (at 300, 350, 400 and 500 K) and at the gas–solid interface.

In the second study, Gates and co-workers use aberration-corrected scanning transmission electron microscopy (STEM) to study the "first steps of metal nanocluster formation" from another well characterized $Ir(C_2H_4)_2$ complex supported on zeolite Al-SSZ-53 and under the influence of the STEM electron beam [294]. The interested reader is referred to these papers for the synthetic and mechanistic details and insights therein.

Acknowledgements

We gratefully acknowledge support from the Chemical Sciences, Geosciences and Biosciences Division, Office of Basic Energy Sciences, Office of Science, U.S. Department of Energy, Grant DE-FG02-03ER15453.

Appendix A. Supplementary data

Supplementary data associated with this article can be found, in the online version, at doi:10.1016/j.molcata.2011.11.011.

References

[1] H. Heinemann, Handbook of Heterogeneous Catalysis, vol. 1, VCH, Weinheim, 1997.
[2] J.M. Thomas, Angew. Chem. Int. Ed. 27 (1988) 1673–1691.
[3] C.H. Bartholomew, R.J. Farrauto, Fundamentals of Industrial Catalytic Processes, second ed., John Wiley & Sons, Hoboken, 2006.
[4] B.C. Gates, G.W. Huber, C.L. Marshall, P.N. Ross, J. Siirola, Y. Wang, MRS Bull. 33 (2008) 429–435.
[5] B.C. Gates, Catalytic Chemistry, John Wiley & Sons, New York, 1992.
[6] A.T. Bell, Science 299 (2003) 1688–1691.
[7] R. Schlögl, S.B. Abd Hamid, Angew. Chem. Int. Ed. 43 (2004) 1628–1637.
[8] M. Che, C.O. Bennett, Adv. Catal. 36 (1989) 55–172.
[9] R.A. van Santen, Acc. Chem. Res. 42 (2009) 57–66.
[10] G. Leendert Bezemer, J.H. Bitter, H.P.C.E. Kuipers, H. Oosterbeek, J.E. Holewijn, X. Xu, F. Kapteijn, A. Jos van Dillen, K.P. de Jong, J. Am. Chem. Soc. 128 (2006) 3956–3964.
[11] G.A. Somorjai, Catal. Lett. 7 (1990) 169–182.
[12] K.M. Bratlie, H. Lee, K. Komvopoulos, P. Yang, G.A. Somorjai, Nano Lett. 7 (2007) 3097–3101.
[13] I. Lee, F. Delbecq, R. Morales, M.A. Albiter, F. Zaera, Nat. Mater. 8 (2009) 132–138.
[14] D.J. Sajkowski, M. Boudart, Catal. Rev. Sci. Eng. 29 (1987) 325–360.
[15] G.C. Bond, Acc. Chem. Res. 26 (1993) 490–495.
[16] H.-S. Oh, J.H. Yang, C.K. Costello, Y.M. Wang, S.R. Bare, H.H. Kung, M.C. Kung, J. Catal. 210 (2002) 375–386.
[17] L.V. Tiep, M. Bureau-Tardy, G. Bulgi, G. Djega-Maridassou, M. Che, G.C. Bond, J. Catal. 99 (1986) 449–460.
[18] G.A. Somorjai, K. McCrea, Appl. Catal. A: Gen. 222 (2001) 3–18.
[19] G.A. Somorjai, J.Y. Park, Angew. Chem. Int. Ed. 47 (2008) 9212–9228.
[20] Z. Ma, F. Zaera, in: B.R. King (Ed.), Heterogeneous Catalysis by Metals, John Wiley & Sons Ltd., West Sussex, 2005, pp. 1768–1784.
[21] S.H. Joo, J.Y. Park, C.-H. Tsung, Y. Yamada, P. Yang, Nat. Mater. 8 (2009) 126–131.
[22] J.M. Thomas, J. Chem. Phys. 128 (2008) 182502.
[23] G.J. Hutchings, J. Mater. Chem. 19 (2009) 1222–1235.
[24] E.V. Anslyn, D.A. Dougherty, Modern Physical Organic Chemistry, University Science Books, Sausalito, CA, 2006.
[25] J.P. Collman, L.S. Hegedus, J.R. Norton, R.G. Finke, Principles and Applications of Organotransition Metal Chemistry, second ed., University Science Books, Sausalito, CA, 1987.
[26] J. Hartwig, Organotransition Metal Chemistry: From Bonding to Catalysis, University Science Books, Sausalito, CA, 2010.
[27] J.H. Espenson, Chemical Kinetics and Reaction Mechanisms, second ed., McGraw-Hill, New York, 2002.
[28] R.G. Wilkins, Kinetics and Mechanism of Reactions of Transition Metal Complexes, second ed., VCH Publishers Inc., New York, 1991.
[29] R.A. Dalla Betta, M. Boudart, in: J.-W. Hightower (Ed.), Proceeding of the 5th International Congress on Catalysis, Elsevier, Amsterdam, 1973, pp. 1329–1341.
[30] A.C. Herd, C.G. Pope, J. Chem. Soc. Faraday Trans. 69 (1973) 833–838.
[31] M. Kermarec, M. Briend-Faure, D. Delafosse, J. Chem. Soc. Chem. Commun. 8 (1975) 272–273.
[32] H. Beyer, P.A. Jacobs, J.B. Uytterhoeven, J. Chem. Soc. Faraday Trans. 72 (1976) 674–685.
[33] P.A. Jacobs, M. Tielen, J.-P. Linart, J.B. Uytterhoeven, H. Beyer, J. Chem. Soc. Faraday Trans. 72 (1976) 2793–2804.
[34] M. Briend-Faure, D. Delafosse, J. Chem. Soc. Faraday Trans. 73 (1977) 905–912.
[35] M. Briend-Faure, J. Jeanjean, M. Keramerec, D. Delafosse, J. Chem. Soc. Faraday Trans. 74 (1978) 1538–1544.
[36] D. Hermerschmidt, R. Haul, Ber. Bunsen-Ges. Phys. Chem. 84 (1980) 902–907.
[37] H.K. Beyer, P.A. Jacobs, Stud. Surf. Sci. Catal. 12 (1982) 95–102.
[38] H. Dexpert, J. Phys. 47 (1986) 219–226.
[39] M.S. Tzou, W.M.H. Sachtler, Stud. Surf. Sci. Catal. 38 (1988) 233–241.
[40] F. Le Normand, D. Bazin, H. Dexpert, P. Lagarde, J.P. Bournonville, in: M.J. Philips, M. Ternan (Eds.), Proceeding of the 9th International Congress on Catalysis, Elsevier, Amsterdam, 1988, pp. 1401–1409.
[41] S.T. Homeyer, W.M.H. Sachtler, J. Catal. 118 (1989) 266–274.
[42] R.A. Schoonheydt, H. Leeman, J. Phys. Chem. 93 (1989) 2048–2053.
[43] D. Bazin, H. Dexpert, J.P. Bournonville, J. Lynch, J. Catal. 123 (1990) 86–97.
[44] M. Che, Z.X. Cheng, C. Louis, J. Am. Chem. Soc. 117 (1995) 2008–2018.
[45] M.S. Nashner, A.I. Frenkel, D. Somerville, C.W. Hills, J.R. Shapley, R.G. Nuzzo, J. Am. Chem. Soc. 120 (1998) 8093–8101.
[46] A. Yamaguchi, T. Shido, Y. Inada, T. Kogure, K. Asakura, M. Nomura, Y. Iwasawa, Catal. Lett. 68 (2000) 139–145.
[47] M.K. Oudenhuijzen, P.J. Kooyman, B. Tappel, J.A. van Bokhoven, D.C. Koningsberger, J. Catal. 205 (2002) 135–146.
[48] S.G. Fiddy, M.A. Newton, T. Campbell, A.J. Dent, I. Harvey, G. Salvini, S. Turin, J. Evans, Phys. Chem. Chem. Phys. 4 (2002) 827–834.
[49] M.K. Neylon, C.L. Marshall, A.J. Kropf, J. Am. Chem. Soc. 124 (2002) 5457–5465.
[50] K. Okumura, R. Yoshimoto, T. Uruga, H. Tanida, K. Kato, S. Yokota, M. Niwa, J. Phys. Chem. B 108 (2004) 6250–6255.
[51] F. Li, B.C. Gates, J. Phys. Chem. B 108 (2004) 11259–11264.
[52] J.H. Yang, J.D. Henao, M.C. Raphulu, Y. Wang, T. Caputo, A.J. Groszek, M.C. Kung, M.S. Scurrell, J.T. Miller, H.H. Kung, J. Phys. Chem. B 109 (2005) 10319–10326.
[53] P. Li, J. Liu, N. Nag, P.A. Crozier, Surf. Sci. 600 (2006) 693–702.
[54] B.J. Hwang, C.-H. Chen, L.S. Sarma, J.-M. Chen, G.-R. Wang, M.-T. Tang, D.-G. Liu, J.-F. Lee, J. Phys. Chem. B 110 (2006) 6475–6482.
[55] H. Tanaka, M. Uenishi, M. Taniguchi, I. Tan, K. Narita, M. Kimura, K. Kaneko, Y. Nishihata, J. Mizuki, Catal. Today 117 (2006) 321–328.
[56] P.J. Chupas, K.W. Chapman, G. Jennings, P.L. Lee, C.P. Grey, J. Am. Chem. Soc. 129 (2007) 13822–13824.
[57] K.-I. Shimizu, K. Sugino, K. Kato, S. Yokota, K. Okumura, A. Satsuma, J. Phys. Chem. C 111 (2007) 1683–1688.
[58] K. Okumura, K. Kato, T. Sanada, M. Niwa, J. Phys. Chem. C 111 (2007) 14426–14432.
[59] E. Bus, R. Prins, J.A. van Bokhoven, Phys. Chem. Chem. Phys. 9 (2007) 3312–3320.
[60] A. Uzun, B.C. Gates, Angew. Chem. Int. Ed. 47 (2008) 9245–9248.
[61] A.J. Liang, B.C. Gates, J. Phys. Chem. C 112 (2008) 18039–18049.
[62] K. Okumura, T. Honma, S. Hirayama, T. Sanada, M. Niwa, J. Phys. Chem. C 112 (2008) 16740–16747.
[63] K. Okumura, H. Matsui, T. Sanada, M. Arao, T. Honma, S. Hirayama, M. Niwa, J. Catal. 265 (2009) 89–98.
[64] A. Kulkarni, B.C. Gates, Angew. Chem. Int. Ed. 48 (2009) 9697–9700.
[65] T. Shishido, H. Asakura, F. Amano, T. Sone, S. Yamazoe, K. Kato, K. Teramura, T. Tanaka, Catal. Lett. 131 (2009) 413–418.
[66] P.J. Chupas, K.W. Chapman, H. Chen, C.P. Grey, Catal. Today 145 (2009) 213–219.
[67] S. Nassreddine, G. Bergeret, B. Jouguet, C. Geantet, L. Piccolo, Phys. Chem. Chem. Phys. 12 (2010) 7812–7820.
[68] A. Singh, K. Luening, S. Brennan, T. Homma, N. Kubo, P. Pianetta, AIP Conf. Proc. 705 (2004) 1086–1089.
[69] Y. Wang, X. Xu, Z. Tian, Y. Zong, H. Cheng, C. Lin, Chem. Eur. J. 12 (2006) 2542–2549.
[70] S. Marre, F. Cansell, C. Aymonier, Nanotechnology 17 (2006) 4594–4599.
[71] S. Marre, A. Erriguible, A. Perdomo, F. Cansell, F. Marias, C. Aymonier, J. Phys. Chem. C 113 (2009) 5096–5104.
[72] J.E. Mondloch, X. Yan, R.G. Finke, J. Am. Chem. Soc. 131 (2009) 6389–6396.
[73] L.M. Rossi, I.M. Nangoi, N.J.S. Costa, Inorg. Chem. 48 (2009) 4640–4642.
[74] J.E. Mondloch, Q. Wang, A.I. Frenkel, R.G. Finke, J. Am. Chem. Soc. 132 (2010) 9701–9714.
[75] J.E. Mondloch, R.G. Finke, J. Am. Chem. Soc. 133 (2011) 7744–7756.
[76] C.T. Campbell, Surf. Sci. Rep. 27 (1997) 1–111.

[77] C.R. Henry, Surf. Sci. Rep. 31 (1998) 231–325.
[78] H. Poppa, Catal. Rev. Sci. Eng. 35 (1993) 359–398.
[79] J.A. Venables, in: W.K. Liu, M.B. Santos (Eds.), Thin Films: Heteroepitaxial Systems, Series on Directions in Condensed Matter Physics, vol. 15, World Scientific Publishing, Singapore, 1999, pp. 1–53.
[80] D.W. Goodman, J. Phys. Chem. 100 (1996) 13090–13102.
[81] P.L.J. Gunter, J.W. Niemantsverdriet, F.H. Riberio, G.A. Somorjai, Catal. Rev. Sci. Eng. 39 (1997) 77–168.
[82] G. Ertl, H.-J. Freund, Phys. Today 52 (1999) 32–38.
[83] R. Imbihl, R.J. Behm, R. Schlögl, Phys. Chem. Chem. Phys. 9 (2007) 3459.
[84] G.A. Somorjai, R.L. York, D. Butcher, J.Y. Park, Phys. Chem. Chem. Phys. 9 (2007) 3500–3513.
[85] M.A. Newton, Chem. Soc. Rev. 37 (2008) 2644–2657.
[86] M.M. Günter, B. Bems, R. Schlögl, T. Ressler, J. Synchrotron Radiat. 8 (2001) 619–621.
[87] M.A. Newton, S.G. Fiddy, G. Guilera, B. Jyoti, J. Evans, Chem. Commun. (2005) 118–120.
[88] R. Imbihl, G. Ertl, Chem. Rev. 95 (1995) 697–733.
[89] For an example see: J.A. Rodriguez, J.Y. Kim, J.C. Hanson, M. Perez, A.I. Frenkel, Catal. Lett. 85 (2003) 247–254.
[90] Examples of kinetic studies of photodeposited supported-nanoparticles include:
(a) H. Yoneyama, N. Nishimura, H. Tamura, J. Phys. Chem. 85 (1981) 268–272;
(b) J.-M. Herrmann, J. Disdier, P. Pichat, J. Phys. Chem. 90 (1986) 6028–6034;
(c) E. Borgarello, N. Serpone, G. Emo, R. Harris, E. Pelizzetti, C. Minero, Inorg. Chem. 25 (1986) 4499–4503;
(d) A. Fernández, A. Caballero, A.R. González-Elipe, J.-M. Hermann, H. Dexpert, F. Villain, J. Phys. Chem. 99 (1995) 3303–3309;
(e) K. Teramura, S.-I. Okuoka, S. Yamazoe, K. Kato, T. Shishido, T. Tanaka, J. Phys. Chem. C 112 (2008) 8495–8498;
(f) J. Ohyama, K. Teramura, S.-I. Okuoka, S. Yamazoe, K. Kato, T. Shishido, T. Tanaka, Langmuir 26 (2010) 13907–13912.
[91] I. Yordanov, R. Knoerr, V. De Waele, M. Mostafavi, P. Bazin, S. Thomas, M. Rivallan, L. Lakiss, T.H. Metzger, S. Mintova, J. Phys. Chem. C 114 (2010) 20974–20982.
[92] M. Che, O. Clause, C. Marcilly, in: G. Ertl, H. Knözinger, J. Weitkamp (Eds.), Preparation of Solid Catalysts, Wiley-VCH, Weinheim, 1999, pp. 315–526.
[93] See several chapters in the recent book: J.R. Regalbuto (Ed.), Catalyst Preparation Science and Engineering, CRC Press, Boca Raton, 2007.
[94] Many interesting individual reports can also be found in a series of proceedings dedicated to the subject titled "International Symposium on Scientific Bases for the Preparation of Heterogeneous Catalysts" which was originally edited by B. Delmon.
[95] C. Perego, P. Villa, Catal. Today 34 (1997) 281–305.
[96] M. Komiyama, Catal. Rev. Sci. Eng. 27 (1985) 341–372.
[97] J.W. Geus, A.J. van Dillen, in: G. Ertl, H. Knözinger, J. Weitkamp (Eds.), Preparation of Solid Catalysts, Wiley-VCH, Weinheim, 1999, pp. 460–487.
[98] W.M.H. Sachtler, in: G. Ertl, H. Knözinger, J. Weitkamp (Eds.), Handbook of Heterogeneous Catalysis, VCH, Weinheim, 1997, pp. 365–374.
[99] B.C. Gates, Chem. Rev. 95 (1995) 511–522.
[100] J.M. Thomas, B.F.G. Johnson, R. Raja, G. Sankar, P.A. Midgley, Acc. Chem. Res. 36 (2003) 20–30.
[101] M.S. Nashner, A.I. Frenkel, D.L. Adler, J.R. Shapley, R.G. Nuzzo, J. Am. Chem. Soc. 119 (1997) 7760–7771.
[102] G. Schmid (Ed.), Clusters and Colloids: From Theory to Applications, VCH Publishers, Inc., New York, NY, 1994.
[103] R.G. Finke, in: D.L. Feldheim, C.A. Foss Jr. (Eds.), Metal Nanoparticles: Synthesis, Characterization and Applications, Marcel Dekker, Inc., New York, 2002.
[104] E. Bayram, M. Zahmakıran, S. Özkar, R.G. Finke, Langmuir 26 (2010) 12455–12464.
[105] G. Schmid, D. Fenske, Philos. Trans. R. Soc. A 368 (2010) 1207–1536.
[106] J.A. Schwarz, C. Contescu, A. Contescu, Chem. Rev. 95 (1995) 477–510.
[107] B.M. Weckhuysen, Phys. Chem. Chem. Phys. 5 (2003) 4351–4360.
[108] M.A. Bañares, Catal. Today 100 (2005) 71–77.
[109] S.J. Tinnemans, J.B. Mesu, K. Kervinen, T. Visser, T.A. Nijhuis, A.M. Beale, D.E. Keller, A.M.J. van der Eerden, B.M. Weckhuysen, Catal. Today 113 (2006) 3–15.
[110] F. Meunier, M. Daturi, Catal. Today 113 (2006) 1–2.
[111] M.A. Bañares, Top. Catal. 52 (2009) 1301–1302.
[112] J.M. Thomas, J.-C. Hernandez-Garrido, Angew. Chem. Int. Ed. 48 (2009) 3904–3907.
[113] J.F. Creemer, S. Helveg, G.H. Hoveling, S. Ullmann, A.M. Molenbroek, P.M. Sarro, H.W. Zandbergen, Ultramicroscopy 108 (2008) 993–998.
[114] H. Zheng, R.K. Smith, Y.-W. Jun, C. Kisielowski, U. Dahmen, A.P. Alivisatos, Science 324 (2009) 1309–1312.
[115] S.-Y. Chung, Y.-M. Kim, J.-G. Kim, Y.-J. Kim, Nat. Phys. 5 (2009) 68–73.
[116] M. Bauer, H. Bertagnolli, ChemPhysChem 10 (2009) 2197–2200.
[117] D.C. Koningsberger, R. Prins (Eds.), X-ray Absorption: Principles, Applications, Techniques of EXAFS, SEXAFS and XANES, John Wiley & Sons, New York, 1988.
[118] D.C. Koningsberger, B.L. Mojet, G.E. van Dorssen, D.E. Ramaker, Top. Catal. 10 (2000) 143–145.
[119] D. Bazin, J.J. Rehr, J. Phys. Chem. B 107 (2003) 12398–12402.
[120] K. Chao, A.C. Wei, J. Electron. Spectrosc. 119 (2001) 175, and references therein.
[121] J.J. Rehr, A.L. Ankudinov, Coord. Chem. Rev. 249 (2005) 131–140.
[122] M. Vaarkamp, D.C. Koninsberger, in: G. Ertl, H. Knözinger, J. Weitkamp (Eds.), Handbook of Heterogeneous Catalysis, vol. 2, VCH, Weinheim, 1997, pp. 475–493.
[123] A.I. Frenkel, C.W. Hills, R.G. Nuzzo, J. Phys. Chem. B 105 (2001) 12689–12703.
[124] A. Kulkarni, R.J. Lobo-Lapidus, B.C. Gates, Chem. Commun. 46 (2010) 5997–6015.
[125] L. Nagy, T. Yamaguchi, K. Yoshida, Struct. Chem. 14 (2003) 77–84.
[126] T. Egami, S.J.L. Billinge, Underneath the Bragg Peaks: Structural Analysis of Complex Materials, Elsevier, Oxford, 2003.
[127] S.J.L. Billinge, in: R.E. Dinnebier, S.J.L. Billinge (Eds.), Powder Diffraction: Theory and Practice, RSC, London, 2008.
[128] S.J.L. Billinge, J. Solid State Chem. 181 (2008) 1695–1700.
[129] S.J.L. Billinge, M.G. Kanatzidis, Chem. Commun. (2004) 749–760.
[130] S.J.L. Billinge, I. Leven, Science 316 (2007) 561–565.
[131] R.S. Drago, Physical Methods in Chemistry, W.B. Saunders Company, Philadelphia, 1977.
[132] D.C. Harris, M.D. Bertolucci, Symmetry and Spectroscopy: An Introduction to Vibrational and Electronic Spectroscopy, Oxford University Press Inc., New York, 1978.
[133] J.C. Fierro-Gonzalez, S. Kuba, Y. Hao, B.C. Gates, J. Phys. Chem. B 110 (2006) 13326–13351.
[134] J.D. Aiken, R.G. Finke, J. Mol. Catal. A: Chem. 145 (1999) 1–44.
[135] D.B. Williams, C.B. Carter, Transmission Electron Microscopy, Plenum Press, New York, 1996 (Chapter 4).
[136] M. Jacoby, C&E News 86 (2008) 31–34.
[137] H. Knözinger, in: G. Ertl, H. Knözinger, J. Weitkamp (Eds.), Handbook of Heterogeneous Catalysis, vol. 2, VCH, Weinheim, 1997, pp. 676–689.
[138] A.K. Galwey, M.E. Brown, Thermochim. Acta 269 (1995) 1–25.
[139] M.E. Brown, J. Therm. Anal. 49 (1997) 17–32.
[140] A.K. Galwey, Thermochim. Acta 413 (2004) 139–183.
[141] A.K. Galwey, J. Therm. Anal. Calorim. 92 (2008) 967–983.
[142] R.M. Dessau, J. Catal. 77 (1982) 304–306.
[143] F. Ribeiro, C. Marcilly, M. Guisnet, J. Catal. 78 (1982) 275–280.
[144] A.I. Mashchenko, O.D. Bronnikov, R.V. Dmitriev, V.I. Garanin, V.B. Kazanskii, K.M. Minachev, Kinet. Catal. 15 (1974) 1418–1419.
[145] W.J. Reagan, A.W. Chester, G.T. Kerr, J. Catal. 69 (1981) 89–100.
[146] D. Exner, N. Jaeger, K. Moller, G. Schulz-Ekloff, J. Chem. Soc. Faraday Trans. 78 (1982) 3537–3544.
[147] W.M.H. Sachtler, M.S. Tzou, F.J. Jiang, Solid State Ionics 26 (1988) 71–76.
[148] M.S. Tzou, B.K. Teo, W.M.H. Sachtler, J. Catal. 113 (1988) 220–235.
[149] S.T. Homeyer, W.M.H. Sachtler, J. Catal. 117 (1989) 91–101.
[150] A. Paez-Munoz, D.C. Koningsberger, J. Phys. Chem. 99 (1995) 4193–4204.
[151] A.C.M. van den Broek, J. van Grondelle, R.A. van Santen, J. Catal. 167 (1997) 417–424.
[152] J.B. Uytterhoeven, Acta Phys. Chem. 24 (1978) 53–69.
[153] P.A. Jacobs, Stud. Surf. Sci. Catal. 12 (1982) 71–85.
[154] D. Delafosse, J. Chim. Phys. 83 (1986) 791–799.
[155] P.A. Jacobs, Carboniogenic Activity of Zeolites, Elsevier Scientific Publishing Company, New York, 1977, pp. 184–227.
[156] M.A. Watzky, E.E. Finney, R.G. Finke, J. Am. Chem. Soc. 130 (2008) 11959–11969.
[157] M.A. Watzky, R.G. Finke, Chem. Mater. 9 (1997) 3083–3095.
[158] H.L. Coonradt, F.G. Ciapetta, W.E. Garwood, W.K. Leaman, J.N. Miale, Ind. Eng. Chem. 53 (1961) 727–732.
[159] M.J. Sterba, V. Haensel, Ind. Eng. Chem. Prod. Res. Dev. 15 (1976) 2–17.
[160] C.N. Satterfield, Heterogeneous Catalysis in Practice, McGraw-Hill Inc., New York, 1980.
[161] L.R. Gellens, W.J. Mortier, J.B. Uytterhoeven, Zeolites 1 (1981) 85–90.
[162] W.A. Spieker, J. Liu, J.T. Miller, A.J. Kropf, J.R. Regalbuto, Appl. Catal. A: Gen. 232 (2002) 219–235.
[163] W.A. Speiker, J. Liu, J.T. Miller, A.J. Kropf, J.R. Regalbuto, Appl. Catal. A: Gen. 243 (2003) 52–66.
[164] B.N. Shelimov, J.-F. Lambert, M. Che, B. Didillon, J. Mol. Catal. A: Chem. 158 (2000) 91–99.
[165] T. Mang, B. Breitshceidel, P. Polanek, H. Knözinger, Appl. Catal. A: Gen. 106 (1993) 239–258.
[166] J.P. Brunelle, Pure Appl. Chem. 50 (1978) 1211–1229.
[167] M. Haruta, Cattech 6 (2002) 102–115.
[168] S. Wang, K. Qian, X. Bi, W. Huang, J. Phys. Chem. C 113 (2009) 6505–6510.
[169] T.M. Anderson, W.A. Neiwert, M.L. Kirk, P.M.B. Piccoli, A.J. Schultz, T.F. Koetzle, D.G. Musaev, K. Morokuma, R. Cao, C.L. Hill, Science 306 (2004) 2074–2077.
[170] R. Cao, T.M. Anderson, D.A. Hillesheim, P. Kögerler, K.I. Hardcastle, C.L. Hill, Angew. Chem. Int. Ed. 47 (2008) 9380–9382.
[171] A.M. Morris, O.P. Anderson, R.G. Finke, Inorg. Chem. 48 (2009) 4411–4420.
[172] U. Lee, H.-C. Joo, K.-M. Park, S.S. Mal, U. Kortz, B. Keita, L. Nadjo, Angew. Chem. Int. Ed. 47 (2008) 793–796.
[173] U. Kortz, U. Lee, H.-C. Joo, K.-M. Park, S.S. Mal, M.H. Dickman, G.B. Jameson, Angew. Chem. Int. Ed. 47 (2008) 9383–9384.
[174] M.D. Baker, G.A. Ozin, J. Godber, J. Phys. Chem. 88 (1984) 4902–4904.
[175] P.A. Jacobs, J.B. Uytterhoeven, H.K. Beyer, J. Chem. Soc. Faraday Trans. 75 (1979) 56–64.
[176] Y. Kim, K. Seff, J. Am. Chem. Soc. 99 (1977) 7055–7057.
[177] Y. Kim, K. Seff, J. Am. Chem. Soc. 100 (1978) 175–180.
[178] R. Kellerman, J. Texter, J. Chem. Phys. 70 (1979) 1562–1563.

[179] L.R. Gellens, W.J. Mortier, R.A. Schoonheydt, J.B. Uytterhoeven, J. Phys. Chem. 85 (1981) 2783–2788.
[180] L.R. Gellens, W.J. Mortier, J.B. Uytterhoeven, Zeolites 1 (1981) 11–18.
[181] G.A. Ozin, F. Hugues, J. Phys. Chem. 87 (1983) 94–97.
[182] J. Michalik, L. Kevan, J. Am. Chem. Soc. 108 (1986) 4247–4253.
[183] J. Texter, R. Kellerman, T. Gonsiorowski, J. Phys. Chem. 90 (1986) 2118–2124.
[184] N.D. Cvjeticanin, N.A. Petranovic, Zeolites 14 (1994) 35–41.
[185] T. Sun, K. Seff, Chem. Rev. 94 (1994) 857–870.
[186] R. Schollner, H.K. Beyer, Zeolites 4 (1984) 61–66.
[187] M.D. Baker, G.A. Ozin, J. Godber, J. Phys. Chem. 89 (1985) 305–311.
[188] M.D. Baker, J. Godber, G.A. Ozin, J. Phys. Chem. 89 (1985) 2299–2304.
[189] W.C. Conner Jr., J.L. Falconer, Chem. Rev. 95 (1995) 759–788.
[190] B.J. Hornstein, R.G. Finke, Chem. Mater. 16 (2004) 139–150 (see also: Chem. Mater. 16 (2004) 3972).
[191] C. Besson, E.E. Finney, R.G. Finke, J. Am. Chem. Soc. 127 (2005) 8179–8184.
[192] C. Besson, E.E. Finney, R.G. Finke, Chem. Mater. 17 (2005) 4925–4938.
[193] M.A. Watzky, R.G. Finke, J. Am. Chem. Soc. 119 (1997) 10382–10400.
[194] A recent review of the kinetic and mechanistic studies of transition-metal nanoparticle nucleation and growth, with an emphasis on the nucleation process, has appeared: E.E. Finney, R.G. Finke, J. Colloid Interface Sci. 317 (2008) 351–374.
[195] A. Henglein, M. Giersig, J. Phys. Chem. B 103 (1999) 9533–9539.
[196] J. Wang, H.F.M. Boelens, M.B. Thatagar, G. Rothenberg, ChemPhysChem 5 (2004) 93–98.
[197] R. Patakfalvi, S. Papp, I. Dékány, J. Nanopartic. Res. 9 (2007) 353–364.
[198] M. Harada, E. Katagiri, Langmuir 26 (2010) 17896–17905.
[199] T. Koenig, R.G. Finke, J. Am. Chem. Soc. 110 (1988) 2657–2658.
[200] T.W. Koenig, B.P. Hay, R.G. Finke, Polyhedron 7 (1988) 1499–1516.
[201] D.H. Leung, R.G. Bergman, K.N. Raymond, J. Am. Chem. Soc. 130 (2008) 2798–2805.
[202] J. Evans, in: J.-M. Basset, B.C. Gates, J.-P. Candy (Eds.), Surface Organometallic Chemistry: Molecular Approaches to Surface Catalysis, Kluwer, Dordrecht, 1988, pp. 47–73.
[203] H.H. Lamb, B.C. Gates, H. Knozinger, Angew. Chem. Int. Ed. 27 (1988) 1127–1144.
[204] J.-M. Basset, F. Lefebvre, C. Santini, Coord. Chem. Rev. 178–180 (1998) 1703–1723.
[205] T.J. Marks, Acc. Chem. Res. 25 (1992) 57–65.
[206] J.F. Walzer Jr., U.S. Patent 5,643,847 (1997).
[207] A. Uzun, D.A. Dixon, B.C. Gates, Chem. Cat. Chem. 3 (2011) 95–107.
[208] K.J.J. Mayrhofer, V. Juhart, K. Hartl, M. Hanzlik, M. Arenz, Angew. Chem. Int. Ed. 48 (2009) 3529–3531.
[209] R. Dellapergola, L. Garlaschelli, S. Martinengo, Inorg. Synth. 28 (1990) 245–247.
[210] A. Uzun, V.A. Bhirud, P.W. Kletnieks, J.F. Haw, B.C. Gates, J. Phys. Chem. C 111 (2007) 15064–15073.
[211] V. Ortalan, A. Uzun, B.G. Gates, N.D. Browning, Nat. Nanotechnol. 5 (2010) 506–510.
[212] P. Serna, B.C. Gates, J. Am. Chem. Soc. 133 (2011) 4714–4717.
[213] A. Uzun, B.C. Gates, J. Am. Chem. Soc. 131 (2009) 15887–15894.
[214] E. Bayram, J. Lu, C. Aydin, A. Uzun, N.D. Browning, B.C. Gates, R.G. Finke, Investigation of the catalytically active species, when starting with the well-characterized, site-isolated $[Ir(C_2H_4)_2]$/zeolite-Y complex in contact with solution, via cyclohexene hydrogenation reporter reaction kinetics and post-kinetic EXAFS and HAADF-STEM structural analyses (tentative title).
[215] J.D. Aiken, Y. Lin, R.G. Finke, J. Mol. Catal. A: Chem. 114 (1996) 29–51.
[216] A.C. Templeton, W.P. Wuelfing, R.W. Murray, Acc. Chem. Res. 33 (2000) 27–36.
[217] R.M. Crooks, M. Zhao, L. Sun, V. Chechik, L.K. Yeung, Acc. Chem. Res. 34 (2001) 181–190.
[218] H. Bönnemann, R.M. Richards, Eur. J. Inorg. Chem. (2001) 2455–2480.
[219] A. Roucoux, J. Schulz, H. Patin, Chem. Rev. 102 (2002) 3757–3778.
[220] B.L. Cushing, V.L. Kolesnichenko, C.J. O'Connor, Chem. Rev. 104 (2004) 3893–3946.
[221] D. Astruc, F. Lu, J.R. Aranzaes, Angew. Chem. Int. Ed. 44 (2005) 7852–7872.
[222] J.P. Wilcoxon, B.L. Abrams, Chem. Soc. Rev. 35 (2006) 1162–1194.
[223] L.S. Ott, R.G. Finke, Coord. Chem. Rev. 251 (2007) 1075–1100.
[224] E.G. Mednikov, M.C. Jewell, L.F. Dahl, J. Am. Chem. Soc. 129 (2007) 11619–11630, also see the extensive references therein for similar nanosized clusters, "nanoclusters".
[225] P.D. Jadzinsky, G. Calero, C.J. Ackerson, D.A. Bushnell, R.D. Kornberg, Science 318 (2007) 430–433.
[226] M.W. Heaven, A. Dass, P.S. White, K.M. Holt, R.W. Murray, J. Am. Chem. Soc. 130 (2008) 3754–3755.
[227] H. Qian, R. Jin, Nano Lett. 9 (2009) 4083–4087.
[228] H. Qian, W.T. Eckenhoff, Y. Zhu, T. Pintauer, R. Jin, J. Am. Chem. Soc. 132 (2010) 8280–8281.
[229] J.F. Parker, C.A. Fields-Zinna, R.W. Murray, Acc. Chem. Res. 43 (2010) 1289–1296.
[230] Y. Levi-Kalisman, P.D. Jadzinsky, N. Kalisman, H. Tsunoyama, T. Tsukuda, D.A. Bushnell, R.D. Kornberg, J. Am. Chem. Soc. 133 (2011) 2976–2982.
[231] B. Corain, G. Schmid, N. Toshima (Eds.), Metal Nanoclusters in Catalysis and Materials Science: The Issue of Size Control, Elsevier, Amsterdam, 2008.
[232] T.S. Ahmadi, Z.L. Wang, T.C. Green, A. Henglein, M.A. El-Sayed, Science 272 (1996) 1924–1926.
[233] C. Burda, X. Chen, R. Narayanan, M.A. El-Sayed, Chem. Rev. 105 (2005) 1025–1102.
[234] A.R. Tao, S. Habas, P. Yang, Small 4 (2008) 310–325.
[235] Y. Xia, Y. Xiong, B. Lim, S.E. Skrabalak, Angew. Chem. Int. Ed. 48 (2009) 60–103.
[236] C.B. Murray, Science 324 (2009) 1276–1277.
[237] M. Harada, Y. Inada, Langmuir 25 (2009) 6049–6061.
[238] J. Polte, T.T. Ahner, F. Delissen, S. Sokolov, F. Emmerling, A.F. Thunemann, R. Kraehnert, J. Am. Chem. Soc. 132 (2010) 1296–1301.
[239] J. Polte, R. Erler, A.F. Thunemann, S. Sokolov, T.T. Ahner, K. Rademann, F. Emmerling, R. Kraehnert, ACS Nano 4 (2010) 1076–1082.
[240] T. Yao, Z. Sun, Y. Li, Z. Pan, H. Wei, Y. Xie, M. Nomura, Y. Niwa, W. Yan, Z. Wu, Y. Jiang, Q. Liu, S. Wei, J. Am. Chem. Soc. 132 (2010) 7696–7701.
[241] Z. Kónya, V.F. Puntes, I. Kiricsi, J. Zhu, J.W. Ager III, M.K. Ko, H. Frei, P. Alivisatos, G.A. Somorjai, Chem. Mater. 15 (2003) 1242–1248.
[242] N. Zheng, G.D. Stucky, J. Am. Chem. Soc. 128 (2006) 14278–14280.
[243] I. Lee, R. Morales, M.A. Albiter, F. Zaera, Proc. Natl. Acad. Sci. U.S.A. 105 (2005) 15241–15246.
[244] X. Huang, C. Guo, J. Zuo, N. Zheng, G.D. Stucky, Small 5 (2009) 361–365.
[245] M. Boualleg, J.-M. Basset, J.-P. Candy, P. Delichere, K. Pelzer, L. Veyre, C. Thieuleux, Chem. Mater. 21 (2009) 775–777.
[246] Y. Zhu, H. Qian, B.A. Drake, R. Jin, Angew. Chem. Int. Ed. 49 (2010) 1295–1298.
[247] R.M. Rioux, H. Song, J.D. Hoefelmeyer, P. Yang, G.A. Somorjai, J. Phys. Chem. B 109 (2005) 2192–2202.
[248] H. Song, R.M. Rioux, J.D. Hoefelmeyer, R. Komor, K. Niesz, M. Grass, P. Yang, G.A. Somorjai, J. Am. Chem. Soc. 128 (2006) 3027–3037.
[249] L.S. Ott, B.J. Hornstein, R.G. Finke, Langmuir 22 (2006) 9357–9367.
[250] H. Eniaga, M. Harada, Langmuir 21 (2005) 2578–2584.
[251] R.M. Rioux, B.B. Hsu, M.E. Grass, H. Song, G.A. Somorjai, Catal. Lett. 126 (2008) 10–19.
[252] Y.L. Borodko, L. Jones, H. Lee, H. Frei, G.A. Somorjai, Langmuir 25 (2009) 6665–6671.
[253] S. Pang, Y. Kurosawa, T. Kondo, T. Kawai, Chem. Lett. 34 (2005) 544–545.
[254] W. Chen, J. Kim, S. Sun, S. Chen, Phys. Chem. Chem. Phys. 8 (2006) 2779–2786.
[255] C. Aliaga, J.Y. Park, J. Russell-Renzas, H. Lee, G.A. Somorjai, Catal. Lett. 129 (2009) 1–6.
[256] C. Aliaga, J.Y. Park, Y. Yamada, H. Sook Lee, C.-H. Tsung, P. Yang, G.A. Somorjai, J. Phys. Chem. C 113 (2009) 6150–6155.
[257] A.S. Eppler, J. Zhu, E.A. Anderson, G.A. Somorjai, Top. Catal. 13 (2000) 33–41.
[258] H. Lang, R.A. May, B.L. Iversen, B.D. Chandler, J. Am. Chem. Soc. 125 (2003) 14832–14836.
[259] D. Liu, J. Gao, C.J. Murphy, C.T. Williams, J. Phys. Chem. B 108 (2004) 12911–12916.
[260] A. Singh, B.D. Chandler, Langmuir 21 (2005) 10776–10782.
[261] D.S. Deutsch, A. Siani, P.T. Fanson, H. Hirata, S. Matsumoto, C.T. Williams, M.D. Amiridis, J. Phys. Chem. C 111 (2007) 4246–4255.
[262] M.A. Albiter, F. Zaera, Langmuir 26 (2010) 16204–16210.
[263] K.P. De Jong, J.W. Geus, Appl. Catal. A: Gen. 4 (1982) 41–51.
[264] G.C. Bond, A.F. Rawle, J. Mol. Catal. A: Chem. 109 (1996) 261–271.
[265] E.A. Sales, B. Benhamida, V. Caizergues, J.-P. Lagier, F. Fievet, F. Bozon-Verduraz, Appl. Catal. A: Gen. 172 (1998) 273–283.
[266] Y. Guari, C. Thieuleux, A. Mehdi, C. Reyé, R.J.P. Corriu, S. Gomez-Gallardo, K. Philippot, B. Chaudret, R. Dutartre, Chem. Commun. (2001) 1374–1375.
[267] G. Marconi, P. Pertici, C. Evangelisti, A.M. Caporusso, G. Vitulli, G. Capannelli, M. Hoang, T.W. Turney, J. Organomet. Chem. 689 (2004) 639–646.
[268] V. Hulea, D. Brunel, A. Galarneau, K. Philippot, B. Chaudret, P.J. Kooyman, F. Fajula, Micropor. Mesopor. Mater. 79 (2005) 185–194.
[269] Y. Jiang, Q. Gao, J. Am. Chem. Soc. 128 (2006) 716–717.
[270] M. Zawadzki, J. Okal, Mater. Res. Bull. 43 (2008) 3111–3121.
[271] M. Boutros, A. Denicourt-Nowicki, A. Roucoux, L. Gengembre, P. Beaunier, A. Gedeon, F. Launay, Chem. Commun. (2008) 2920–2922.
[272] R. Xing, Y. Liu, H. Wu, X. Li, M. He, P. Wu, Chem. Commun. (2008) 6297–6299.
[273] M.A. Elmoula, E. Panaitescu, M. Phan, D. Yin, C. Richter, L.H. Lewis, L. Menon, J. Mater. Chem. 19 (2009) 4483–4487.
[274] Y. Xie, K. Ding, Z. Liu, R. Tao, Z. Sun, H. Zhang, G. An, J. Am. Chem. Soc. 131 (2009) 6648–6649.
[275] E. Besson, A. Mehdi, C. Reye, R.J.P. Corriu, J. Mater. Chem. 19 (2009) 4746–4752.
[276] M. Zahmakiran, S. Özkar, Langmuir 25 (2009) 2667–2678.
[277] M. Zahmakiran, Y. Tonbul, S. Özkar, J. Am. Chem. Soc. 132 (2010) 6541–6549.
[278] S. Özkar, R.G. Finke, J. Am. Chem. Soc. 127 (2005) 4800–4808.
[279] L. Starkey Ott, R.G. Finke, Inorg. Chem. 45 (2006) 8382–8393.
[280] J.I. Jeong, M. Choi, Aerosol Sci. 34 (2003) 965–976.
[281] E.E. Finney, R.G. Finke, Chem. Mater. 21 (2009) 4692–4705.
[282] A.M. Morris, M.A. Watzky, R.G. Finke, Biochim. Biophys. Acta 1794 (2009) 375–397.
[283] William of Ockham, 1285–1349, as cited by E.A. Moody, The Encyclopedia of Philosophy, vol. 7, McMillan, 1967.
[284] R.J. Field, E. Koros, R.M. Noyes, J. Am. Chem. Soc. 94 (1972) 8649–8664.
[285] R.J. Field, R.M. Noyes, J. Chem. Phys. 60 (1974) 1877–1884.
[286] R.J. Field, R.M. Noyes, Acc. Chem. Res. 10 (1977) 214–221.
[287] J.D. Aiken III, R.G. Finke, J. Am. Chem. Soc. 120 (1998) 9545–9554.
[288] Y. Lin, R.G. Finke, Inorg. Chem. 33 (1994) 4891–4910.
[289] J.A. Widegren, M.A. Bennett, R.G. Finke, J. Am. Chem. Soc. 125 (2003) 10301–10310.
[290] J.E. Mondloch, R.G. Finke, Kinetic evidence for bimolecular nucleation in supported-transition-metal nanoparticle catalyst formation in contact with

solution: the prototype Ir(1,5-COD)Cl/γ-Al_2O_3 to $Ir(0)_{\sim 900}$/γ-Al_2O_3 system, submitted for publication.
[291] R.G. Finke, S. Özkar, Coord. Chem. Rev. 248 (2004) 135–146.
[292] J.A. Widegren, J.D. Aiken III, S. Özkar, R.G. Finke, Chem. Mater. 13 (2001) 312–324.
[293] H. Zhao, T.M. Nenoff, G. Jennings, P.J. Chupas, K.W. Chapman, J. Phys. Chem. Lett 2 (2011) 2742–2746.
[294] C. Aydin, J. Lu, A.J. Liang, C.-Y. Chen, N.D. Browning, B.C. Gates Nano Lett. (2011) http://dx.doi.org/10.1021/nl2034305.